Anonymous Referee #1

General Comments

1. The manuscript entitled 'High-resolution (0.05°×0.05°) NO_x emissions in the Yangtze River Delta inferred from OMI' focuses on developing a method to inverting NO_x emissions at a high resolution in major urban areas by using the long-term satellite measurements of nitrogen dioxide. The results show that the inverted NO_x emission dataset can reveal the features which are not well represented or not included widely used Multi-scale Emissions Inventory of China. Overall, though the topic is important and the methods are technically, the manuscript need be restructured and rephrased. I recommend to reconsider its publication pending the following concerns satisfactorily addressed.

The manuscript has been overhauled considering the comments from both referees.

A brief review has been made about the inventories at similar resolutions, including Zhao et al. (2015) and CAMS-reg (Granier et al., 2019) on page 3 line 8 (see the revised manuscript) based on bottom-up methods. Top-down estimates can be further combined with bottom-up inventories and spatial proxies to increase the spatial resolution, by downscaling and/or source sector apportionment (e.g., MarcoPolo on page 4 line 1-4). MarcoPolo emissions can reach higher resolutions than 0.05°×0.05°, i.e., 0.01°×0.01°, given the detailed information of the location of the emission sources which ask for lots of efforts to collect and are absent or inaccurate at times. Top-down emissions including our work offer an important supplement and reference at high resolutions.

The PHLET model has been upgraded and re-built on the FEniCS platform, the necessary citations of which have also been included. Based the FEniCS platform, we improve the calculation efficiency of the PHLET and A-PHLET largely. Now, the inversion calculation takes less than one hour as stated on page 6 line 14.

We have also fixed a bug to correctly account for the effect of S_0 in Eq. 3. The corresponding results and discussions have been revised including NO_x emissions, lifetimes and the uncertainties. After processing the error covariance properly, the derived the lifetime of NO_2 due to deposition becomes longer (30.4 h), which is more consistent with our knowledge about NO_x chemistry.

We have shortened the study time period from summer 2012-2016 to summer 2012-2015. According to the National Bureau of Statistics of China (http://data.stats.gov.cn/), NO_x emissions have dropped substantially from 2015 to 2016. Thus, including summer 2016 may not be the best practice to derive emissions.

To substantiate the emission distribution, more discussion has added in Sect. 4.2 based

on the distributions of proxies such as nighttime light, population density, marine shipping routes, coal power plant locations and land use indicated by a satellite photo from Google Earth. Sect. 4.3 compares our emissions with other inventories besides MEIC.

In the conclusion section, we give a summary of the limitations and shortcomings of our method.

Most of the figures have been re-arranged. Some figures have been added, considering comments from both referees.

We have substantially improved the structure of the manuscript to accommodate both reviewers' suggestions. A flowchart has been added to Sect. 2.1 in order to illustrate the procedures of our inversion method. Section 2.3 has been divided into 5 subsections for clarification. Section 2.3.1-2.3.3 describe the model setting and assumptions. Sect. 2.3.4 shows how the SCM matrix is applied to PHLET simulated VCDs, with the detailed procedures shown in Appendix B. Section 2.3.5 summarizes the uncertainty estimates. The part (former Appendix D) about solving the observation error covariance matrix and the adjoint model has been moved to Sect. 2.4, supplemented with an extended discussion on assuming the covariance to be diagonal. The OSSE-like test (former Appendix E) based on GEOS-Chem simulated NO_2 data has been moved to a new Sect. 5.

Specific comments

1. Why the shortest lifetime of NO_2 has the advantage to better relate NO_x emissions to NO_2 VCDs at the 0.05°×0.05° resolution?

Due to the short lifetime of NO_2, the effect of transport and diffusion is rather local. Therefore, the distribution of NO_2 VCDs can better reflect that of NO_x emission at high-resolution; and the effect of transport errors on emission estimate is smaller.

2. Page 6, Line 1-7: What's the relation between the NO_2 retrieval with the AOD? The description is needed.

The NO_2 retrieval becomes unreliable when the loading of aerosol gets too high. We have added necessary citation to this description.

3. Section 2 is generally messy and lack of logics. What's the relation between the PHLET model and PHLET-A model? I suggest the authors rephrase the part 'data and method' more logically.

In order to clarify our method, we have added a flowchart and additional descriptions to illustrate the procedures in Sect. 2. See our response to general comment 1 for the

detailed structural changes.

4. The main of this manuscript includes two parts: part one is to show the distributions of NO_2 basing on the retrieved emission data, part two is to evaluate above emission data. Thus, showing more explicit analyses are needed.

To substantiate the emission distribution, more discussion has added in Sect. 4.2 based on the distributions of proxies such as nighttime light, population density, marine shipping routes, coal power plant locations and land use indicated by a satellite photo from Google Earth. Sect. 4.3 compares our emissions with other inventories besides MEIC.

5. In Figure 1, why the NO_x emission and local net source are somewhat related to the lifetime of NO_2? The good relationship between the NO_2 VCDs and lifetimes of NO_2 can be understood well, however, the relations with NO_x emission and local net source are not taken for granted.

We have clarified the methodology; see our response to general comment 1.

As shown in Eq. (2), the local net source is the difference between emission and loss.

Sect. 2.5 and Appendix C presents how to calculate emission and lifetime from the local net source.

6. Figure 1 and Figure 2 should be rearranged. Fig. 2a-d can be combined into Fig.1a-d; Fig. 2e-f and Fig. 1f can be combined into one graph. The current arrangement is messy to describe.

More figures are included in the revised manuscript. The figures are also re-arranged taking the comments from both of the referees into consideration.

7. Page 17, Line 6, what does ‘Figure 3ows’ mean?

Typing error. Changed.

8. How do the authors define ‘anthropogenic’ emission? Including what?

As now clarified in Sect. 2.3.2 (page 10 line 13-21):

“Lightning emissions, biomass burning emissions, aircraft emissions, transport from neighboring regions, and convection can lead to NO_2 at higher altitudes over the YRD area. However, the amount of NO_2 aloft is much smaller than near-ground NO2 due to large ground sources (Lin, 2012). Thus, we regard NO_2 aloft as the regional background, and do not include it in Eq. 1. Also, for near-ground NO_2 over the YRD area, the

contribution of downward vertical transport is negligible compared to the contribution of ground sources. Aircraft emissions contribute little to the total ground source, because 78% of aircraft emissions occur at the high altitudes (9–12 km) (Ma and Xiuji, 2000). Therefore, PHLET only accounts for near-ground NO_2 from ground soil, biomass burning and anthropogenic sources (energy, industry, transportation, and residential)."

And in Sect. 4.3 (page 21 line 11-13):

"Our emission data and the DECSO inventory are top-down estimates and include the contributions of soil and biomass-burning sources. Thus, we estimate soil and biomass burning emissions from independent sources, and then subtract these emissions from our and DECSO emission datasets" (to obtain anthropogenic emissions.)

9. What's the reason of inconsistent difference of total anthropogenic NOx emission in each city for summer inverted by this study versus from the MEIC inventory? Otherwise, the difference should be same for each city, that is to say, systematically higher or lower.

Both our and MEIC inventories are gridded, and their differences are grid cell independent and vary from one city to another.

10. The tile of Section 4.3 should be 'Comparing our inverted emission dataset with the MEIC inventory', or more exactly, it should be 'Comparison between our inverted emission dataset with the MEIC inventory'.

Changed

Anonymous Referee #2

General Comments

1. This inventory is presented as the only high-resolution inventory for the YRD region, but in the MarcoPolo-Panda project, a high-resolution emission inventory of 0.01-degree resolution has been developed for this region (see http://www.marcopolo-panda.eu/products/toolbox/emission-data/) Since the affiliations of the authors were also participating in the MarcoPolo-Panda project it is surprising that this inventory is not mentioned or used in their comparisons. Also, Zhao et al. (2015) present a city-scale emission inventory with the resolution of 3kmx3km in Nanjing, in the Yangtze River Delta.: "*Zhao, Y., Qiu, L. P., Xu, R. Y., Xie, F. J., Zhang, Q., Yu, Y. Y., Nielsen, C.*

P., Qin, H. X., Wang, H. K., Wu, X. C., Li, W. Q., and Zhang, J.: Advantages of a city-scale emission inventory for urban air quality research and policy: the case of Nanjing, a typical industrial city in the Yangtze River Delta, China, Atmos. Chem. Phys., 15, 12623-12644, 10.5194/acp-15-12623-2015, 2015." The authors claim that very high resolution emissions are lacking, but it is not mentioned how "very high" is defined. Several regions have a high-resolution emission inventory with similar resolution as PHLET: CAMS in Europe, GlobEmissions in the Qatar and South Africa, MarcoPolo-Panda in various regions in China.

We have included discussion of these inventories in the revised introduction:

On page 3 line 1-3: "Gridded bottom-up emission inventories typically use spatial proxies (like population and GDP) to allocate provincial-level emission values, which are derived from activity statistics and emission factor data, to individual locations (Zhao et al., 2011; Janssens-Maenhout et al., 2015; Zhao et al., 2015).".

On page 3 line 7-10: "For a small area, emission factors and activity data of the major sources can be collected by on-site surveys to allow construction of a high-resolution inventory (Zhao et al., 2015; Granier et al., 2019), such as Zhao et al. (2015) for Nanjing. However, on-site surveys are extremely time consuming and resource demanding, difficult to be applied to a large domain in a timely manner."

On page 4 line 1-10: "Top-down estimates can be further combined with bottom-up inventories and spatial proxies to increase the spatial resolution, such as from 0.25°×0.25° in the DECSO derived emissions to 0.01°×0.01° for 2014 during the MarcoPolo Project (Hooyberghs et al., 2016; Timmermans et al., 2016) and similar inventories over Qatar and South Africa (Maiheu and Veldeman, 2013)."

In this work, high resolution refers to emissions at a resolution equal or higher than 0.05°×0.05°. We have made this clear on page 2 line 23 and page 4 line 9.

2. The authors mention that their method is not computationally expensive and can be applied world-wide, but a rough calculation shows that their algorithm will take at least 10 year to calculate the emissions for the whole world, which is not faster than many other methods they refer to on page 3.

First, our method is designed for urban and surrounding areas, rather than everywhere of the globe. Second, in this case study, the calculation is completed on only one CPU core, while the CTMs adopted in top-down method generally ask for parallel computing with many cores. For a multi-domain study, our method can easily adopt parallel computation with more cores. Third, we have upgraded the codes on the FEniCS platform, the necessary citations of which are included. Right now, the emission calculation for the YRD takes less than one hour, faster than our previous calculation by a factor of 30-40. Thus, with one computational core, applying our method to the

globe on a 0.05°×0.05° grid for 4 years would take about a few months.

3. The authors say that the methods are limited in time period, spatial domain and horizontal resolution. This is very different for all the referred methods. The methods of Miyazaki et al and of Stavrakou et al. have already been applied on a global scale, while other methods are also not theoretically limited to a certain domain. In general, the methods mentioned can be applied to any time period as long as satellite observations are available.

We have clarified this point in the revised introduction (page 3 line 25 – page 4 line 1):

"These more sophisticated methods have often been applied to relatively short time periods (e.g., Gu et al., 2016 for one month), small spatial domains (e.g., Tang et al., 2013 in Texas), and/or at coarse horizontal resolutions (e.g., Miyazaki et al., 2012 at 2.8° and Stavrakou et al., 2008 at 5°×5°)."

4. The authors suggest that only (Lin et al., 2012) and Stavrakou et al. (2013) provide uncertainties of the CTM, while they are also presented by Miyazaki et al. (2012) and Ding et al. (2017).

The statement and the citations are modified on page 4 line 6-8: "CTM-based studies typically provide an estimate of the overall model error, although Lin et al. (2012) and Stavrakou et al. (2013) present errors in the individual model processes (e.g., key chemical reactions and meteorological parameters)."

5. What are pros and cons of the introduced method? The pros are mentioned, but what is the downside of averaging a time period of 2012-2016. Specifically, in this period strong trends are appearing in NO_2 over China.

We have shortened the study time period from summer 2012-2016 to summer 2012-2015. According to the National Bureau of Statistics of China (http://data.stats.gov.cn/), NO_x emissions have dropped substantially from 2015 to 2016. Thus, including summer 2016 may not be the best practice to derive emissions.

We have also evaluated the emission for each year from 2012 to 2015. The average emissions of those years over 2012-2015 and the emissions evaluated from all VCD data together (as in the main text) are similar. Slope and interception of their linear regression are 0.95 and 0.08, and their correlation coefficient is 0.98 (see the figure below).

We discussion the limitation of our method in Section 2.

On page 9 line 9-11: "Also, combining data from multiple years to derive an averaged NO_2 distribution for simulation (rather than conducting the simulations for individual

years and months) leads to an additional uncertainty."

We have also added the revised conclusion section a paragraph summarizing the limitations of our method:

On page 25 line 11-20: "Our inversion method also has a few shortcomings. The derived emissions do not separate the individual contributions of anthropogenic sectors (i.e., power plants, industry, transportation, and residential). The spatial resolution of the estimated emissions is limited by that of satellite VCD data, although a special oversampling technique has been used to help achieve the highest spatial resolution possible for emissions. The PHLET model is assumed to be 2-dimensional by simplifying the vertical distribution of NO_2 and not accounting for the spatial variability in the vertical shape, similar to previous studies. The adjoint model assumes the observational error covariance matrix to be diagonal, without fully considering the effect of correlations between individual grid cells. Also, we assume a spatially uniform relationship between NO_2 VCDs and NO_2 lifetimes, which may lead to an underestimate in the lifetimes at low-NO_2 locations over the eastern sea."

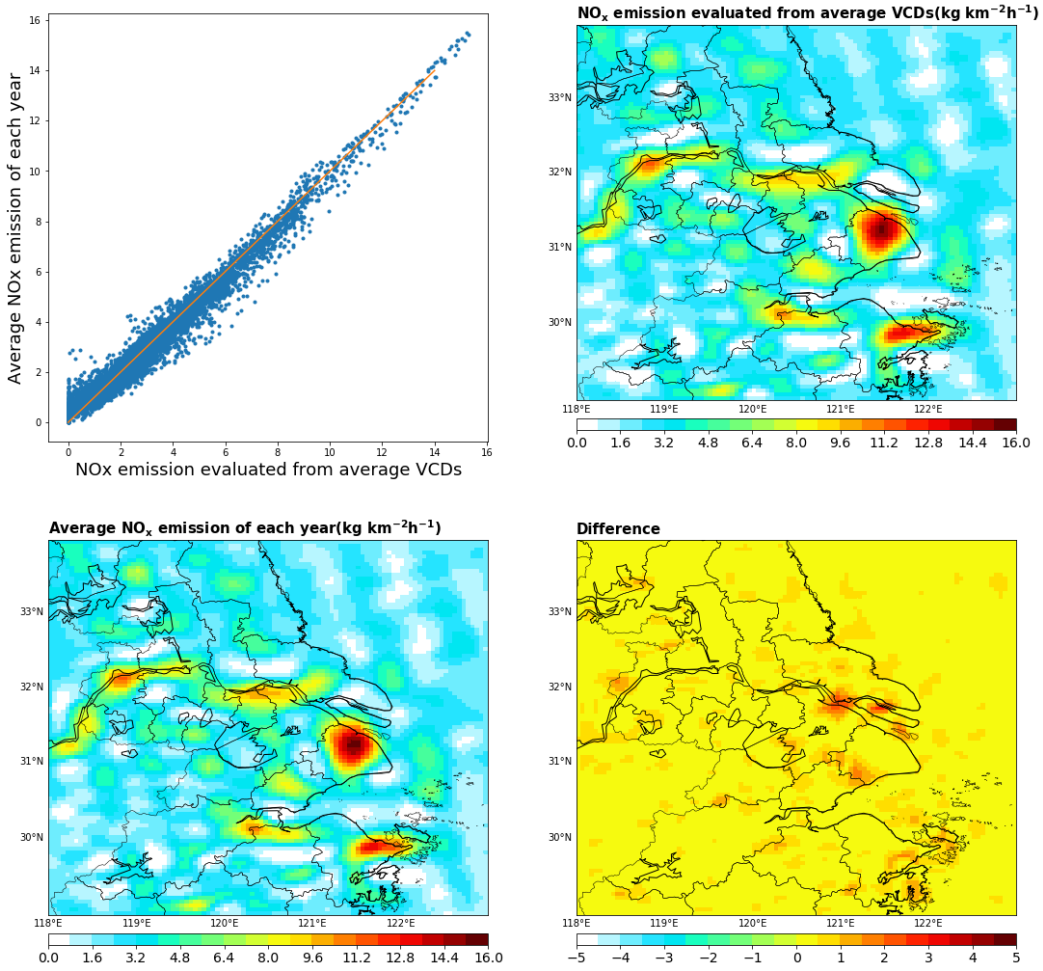

6. The period is focusing on the summer time. What are the expected results for the

winter-period. Will this change the spatial resolution? Will the magnitude of the emissions change a lot?

To achieve highest spatial resolution possible, we have intended to focus on the summer months, when the lifetimes of NO_x are the shortest.

The lifetimes of NO_2 would be longer in winter, and therefore, the effects of transport and diffusion are more significant. The spatial relation of NO_2 VCDs and NO_x emissions would be lower in winter. Thus, it would be much more difficult to derive the emissions at a high resolution, and the influences of transport errors would be much larger.

7. It should at least be mentioned that there is no sector information in the derived emissions, which is an advantage of bottom-up inventories

We have added on page 25 line 11-12: "Our inversion method also has a few shortcomings. The derived emissions do not separate the individual contributions of anthropogenic sectors (i.e., power plants, industry, transportation, and residential)."

Also note that as stated on page 3 line 14-17: "Top-down inversion typically provides the total emission data, although emissions from individual sources can be further derived by integrating a priori data (often from bottom-up inventories) about source-specific information such as diurnal and seasonal variabilities (e.g., Lin et al., 2010; Lin, 2012) and spatial variabilities (Timmermans et al., 2016)."

8. Although the gridding is on a 0.05° resolution the actual spatial resolution of the resulting emissions seems much lower. An indication of the intrinsic resolution can be obtained from the largest gradients in the emissions. I cannot detect clear structures with a 0.05° resolution. One would at least expect some power plants to show up as clear spots in this region. Maybe the method is still limited by the OMI resolution?

The highest emission is at one grid cell in north Shanghai, and its difference from eight surrounding grid cells are 0.39 kg km^{-2} h^{-1} (2.6%). The mean gradient of the emissions is 0.079 kg km^{-3} h^{-1}.

We admit the intrinsic resolution of our derived emissions is limited by the pixel sizes of OMI. We have added in the revised conclusion section that

On page 25 line 12-14: "The spatial resolution of the estimated emissions is limited by that of satellite VCD data, although a special oversampling technique has been used to help achieve the highest spatial resolution possible for emissions."

Also, in Sect. 4.2 on page 22 line 5-7: "This is because our top-down estimate is limited by the intrinsic resolution of NO_2 VCDs, i.e., our oversampling approach does not fully

compensate for the large sizes of OMI pixels. Therefore, the large spatial gradient of NO_x emissions is smoothed to some extent in our dataset."

We have also discussed emissions related to power plants. As detailed in the revised Sect. 4.2 on page 20 line 10-18:

"The filled circles in Fig. 6g show the locations of coal-fired power plants in 2016 from Carbon Brief (www.carbonbrief.org; last access: 2019/6/27). The radius of a circle denotes the power generation capacity. Figure 6h further shows the GPED v1.0 bottom-up NO_x emissions for power plants on a 0.1°×0.1° grid in 2016. Coal-fired power plants in the YRD are normally near the urban centers, traffic lines or other sources. Our top-down NO_x emission map shows large emission values near the power plants (Fig. 6b), although it cannot isolate the sole contribution of power plants. At the GPED power plant locations, the correlation between our and GPED emissions reaches 0.26, due to the influence by non-power plant sources; note that the correlation between GPED emissions and POMINO NO2 VCDs are only about 0.21."

9. The structure of the paper is somewhat confusing and therefore I suggest moving appendix C and E to the main text. Section 2.1 is too short to understand the method of determining emissions.

We have substantially improved the structure of the manuscript to accommodate both reviewers' suggestions. A flowchart has been added to Sect. 2.1 in order to illustrate the procedures of our inversion method. Section 2.3 has been divided into 5 subsections for clarification. Section 2.3.1-2.3.3 describe the model setting and assumptions. Sect. 2.3.4 shows how the SCM matrix is applied to PHLET simulated VCDs, with the detailed procedures shown in Appendix B. Section 2.3.5 summarizes the uncertainty estimates. The part (former Appendix D) about solving the observation error covariance matrix and the adjoint model has been moved to Sect. 2.4, supplemented with an extended discussion on assuming the covariance to be diagonal. The OSSE-like test (former Appendix E) based on GEOS-Chem simulated NO_2 data has been moved to a new Sect. 5.

10. In section 2.3: The contributions of lightning, biomass burning and aircraft emissions are neglected. The authors explained that the contributions of these emissions are small. In the inversion method, both soil and anthropogenic emissions are derived. In section 4, it is calculated that the soil emissions contribute 0.9% of the inverted emissions. This looks like a very small amount. However, biomass burning is considered as a significant source in the YRD, especially in summer. On a scale of 0.05°×0.05° lots of biomass burning activity will exist. Give some more detailed information and explain why lightning, biomass burning and aircraft emissions are neglected.

As now clarified in Sect. 2.3.2 on page 10 line 13-21:

“Lightning emissions, biomass burning emissions, aircraft emissions, transport from neighboring regions, and convection can lead to NO_2 at higher altitudes over the YRD area. However, the amount of NO_2 aloft is much smaller than near-ground NO_2 due to large ground sources (Lin, 2012). Thus, we regard NO_2 aloft as the regional background, and do not include it in Eq. 1. Also, for near-ground NO_2 over the YRD area, the contribution of downward vertical transport is negligible compared to the contribution of ground sources. Aircraft emissions contribute little to the total ground source, because 78% of aircraft emissions occur at the high altitudes (9–12 km) (Ma and Xiuji, 2000). Therefore, PHLET only accounts for near-ground NO_2 from ground soil, biomass burning and anthropogenic sources (energy, industry, transportation, and residential).”

11. The model error is set to be the sum of the quadrature of errors contributed by several aspects. However, there is no explanation on how the authors set some errors, for example the treatment of background NO_2 concentrations. The authors use wind fields from ECMWF on a coarse resolution and regridded to a high resolution. The error of regridded wind field on high resolution can be quite large. The authors consider error of wind speed, but how about the wind direction? The error set for the wind looks optimistic.

Error estimates for individual parameters and processes are based on the literature, our sensitivity tests, and/or expert judgement. For most parameters, the reasoning of choosing specific values is given when the error terms are introduced.

For background NO_2, our choice (0.54×10^{15} molecules cm^{-2}) is based on the consideration that background NO_2 would be very small (e.g., smaller than 1×10^{15} molecules cm^{-2}; Cui et al., 2016). Doubling the background only has marginal effects on our emission estimate especially at modest- and high-NO_2 locations. Spatially averaged, the error due to the choice of our background value is estimated as 5%.

For errors introduced by winds, we have clarified in Sect. 2.3.3 on page 11 line 17-19 that

“We assess the model errors introduced by the uncertainties in the wind field and effective diffusion coefficients by Monte Carlo simulations in which the wind speeds are changed according to their uncertainties. The resulting relative uncertainty in the modeled NO_2 VCDs is about 20%. ”

12. References: All the references should be carefully checked if they are in the correct format, especially the names of authors. Many articles are missing or articles should be removed throughout the whole text. It is advisable to let a native speaker make the necessary corrections.

The references have been checked and some necessary citations have been added.

Specific comments

1. Page 1, Line 14: lacking => missing

Changed.

2. Page 1, Line 17: The inversion => The model used in the inversion

We have change it into ‘the top-down inversion method’ which refers to the whole process.

3. Page 1, Line 18: We construct a model called PHLET (..)

Changed.

4. Page 1, Line 19 Metrix => Matrix

Changed.

5. Page 2, Line 5 tied => related

Changed.

6. Page 2, Line 7 features => structures

Changed.

7. Page 2, Line 8-9: This last sentence is kind of obvious. It should be moved from the abstract to the conclusions/outlook, but I suggest to just remove it.

Removed.

8. Page 2, Line 21: split the sentence into 2 separate sentences to make it more understandable.

Changed. Now on page 2 line 18.

9. Page 2, line 24: on => of

Changed.

10. Page 2, line 24: how is a “very high resolution” defined?

We have made it clear to be 0.05°×0.05° on page 2 line 23 and page 4 line 9.

11. Page 3, Line 1: Bottom-up emissions do not only use spatial proxies but are also based on gathered statistical information of industrial output, car emissions, etc.

The statement has been modified.

12. Page 3, Line 4: Please define “high”

We have made it clear to be 0.05°×0.05° on page 2 line 23 and page 4 line 9.

13. Page 3, Line 20-21: What do the authors mean by “low-cost” and “high-resolution”

Low cost refers to the low requirement on computation resources described on page 6 line 13-16:

“With one computational core (Intel ® Xeon ® Gold 6130 CPU @ 2.10GHz), derivation of NOx emissions over the YRD here takes less than one hour after necessary input data are prepared. Applying the framework to multiple areas would take a similar amount of time by using one computational core for each area.”

As for high resolution, we have made it clear to be 0.05°×0.05° on page 2 line 23 and page 4 line 9.

14. Page 3, Line 22: Here it is mentioned that these inventories are important for trends and variability. I agree, but the method presented in this paper do not give the possibility to study trends and variability, which should be mentioned somewhere in the conclusion.

As now clarified in Sect. 6 on page 24 line 22-24:

“Although this study derives the averaged emissions over summer 2012–2015, calculations of emissions at higher temporal resolutions (e.g., every 2 years) is possible to better capture the interannual variability and trends.”

15. Page 3, Line 22-23: Why is it important to understand air pollution with the advent of TROPOMI? I would say it is the other way around: TROPOMI is important for understanding air pollution.

The sentence has been removed. Discussion about TROPOMI is on page 25 line 25-page 2 line 2 now.

16. Page 3, line 24: Constructing => construct

Changed.

17. Page 4, line 1 other 13 => 13 other

Changed. In addition, we have added two more cities which were missed in the original manuscript.

18. Page 4, line 1: explain the acronym POMINO

Changed. On page 6 line 22.

19. Page 4, line 3: change to “a model called PHLET”

Changed.

20. Page 4, line 5: delete “concentration dependent”

Changed.

21. Page 4, line 17: Why is this the finest spatial information possible?

As described in Sect. 2.2 on page 7 line 25 – page 8 line 4, The oversampling approach takes advantage of the fact that the exact location of footprint of the OMI instrument slightly changes from one day to another, so does the exact location of footprint of a satellite pixel at a given VZA. Thus, sampling from multiple days increases the horizontal resolution of data. Besides, the SCM matrix is constructed base on the pixels, and thus the finest spatial information is preserved.

22. Page 4, line 19: What Is SCM? This is explained much later in the text.

We have re-structured the manuscript and have clarified the use of SCM in Sect. 2.3.4, supplemented by Appendix B.

23. Page 4, line 21-22: Without further explanation this does not explain the method.

A flowchart has been added in order to illustrate the procedures of our inversion method on page 5 line 8 -page 6 line 4.

24. Page 4, line 22: Which fixed formula is used?

It refers to Eq. C5 in Appendix C. The statement has been modified.

25. Page 5, line 1: Which nonlinear relationship do the authors mean here? There are 3 quantities mentioned: (1) emissions, (2) lifetimes and (3) VCDs.

Between lifetimes and NO_2 VCDs. Changed now on page 6 line 8.

26. Page 5, line 4: A long time period is mentioned. What do the authors mean, a long time period to average or multiple 5 years periods? And why are these long time periods not presented in this paper?

We meant summer 2012-2016.

We have shortened the study time period from summer 2012-2016 to summer 2012-2015. According to the National Bureau of Statistics of China (http://data.stats.gov.cn/), NO_x emissions have dropped substantially from 2015 to 2016. Thus, including summer 2016 may not be the best practice to derive emissions.

27. Page 5, line 5: It is mentioned that the calculation takes about 36 hours after necessary input data? What are the necessary input data? How long does it take to prepare the input data?

The necessary input data are the OMI product (i.e. POMINO) and wind field. The time it takes to prepare those data depends on the Internet conditions, as in other studies. Running our codes to process these input data takes 30-40 minutes for the YRD domain here.

28. Page 5, line 5: If the inversion takes 36 hours for a 5x5 degree domain, a global calculation will take about 10000 hours, which is about 10 year.

See 'general comments 2'. And as stated on page 6 line 14-16, applying the framework to multiple areas would take a similar amount of time by using one computational core for each area.

29. Page 5, line 8: a reference for OMI is missing.

Added.

30. Page 6, line 2-7: Removing the 30 outer pixel and the row anomaly will strongly reduce the number of pixels used in this research. How may pixels be still used?

22007 pixels. Added.

31. Page 6, line 8: space => grid

Changed. Corresponding texts are now in Sect. 2.3.4

32. Page 6, line 11: The footprint does not change, the location of the footprint changes from one day to another.

Changed.

33. Page 6, line 14: the year of the reference to Fioletov is missing.

The sentence has been changed.

34. Page 6, line 17: For purpose => For the purpose

Changed, now on page 8 line 5.

35. Page 7, Line 7: The assumptions of the PHLET model are not mentioned in Beirle et al. This reference should be removed.

A similar assumption on the vertical shape of NO_2 is taken in Beirle et al. (2011), as their model does not include information about the (horizontal and temporal) changes in the vertical shape of NO_2. In their online supporting information, "At the OMI observation time under cloud free conditions, the megacity emissions undergo rapid vertically mixing (within some km distance from the source)".

36. Page 7, Line 10: The transport from neighbouring regions is missing in this list while this is an important contribution.

We consider the transport from outside the study domain as part of the regional background. We write in the revised Sect. 2.3.2 (page 10 line 13-16) that

"Lightning emissions, biomass burning emissions, aircraft emissions, transport from neighboring regions, and convection can lead to NO_2 at higher altitudes over the YRD area. However, the amount of NO_2 aloft is much smaller than near-ground NO_2 due to large ground sources (Lin, 2012). Thus, we regard NO_2 aloft as the regional background, and do not include it in Eq. 1."

37. Page 7, Line15-16: Can the authors give a reference for this statement.

The reference about aircraft emission is given. The statement has been adjusted since the biomass burning NO_x should be taken into consideration.

38. Page 7, Line 17-20: This is quite some assumption about the background value. What is the basis of this assumption? Why is the uncertainty set to 5%?

For background NO_2, our choice (0.54×10^{15} molecules cm^{-2}) is based on the consideration that background NO_2 would be very small (e.g., smaller than 1×10^{15} molecules cm^{-2}; Cui et al., 2016). Doubling the background only has marginal effects on our emission estimate especially at modest- and high-NO_2 locations. Spatially averaged, the error due to the choice of our background value is estimated as 5%.

39. Page 8, line 14: What is the source of the wind data?

Described in Sect. 2.3.3. The data are from ERA5.

40. Page 9, Line 20: space => grid

Changed.

41. Page 11, Line 7-8: I would suggest mentioning the average number of iterations (about 60?) needed to reach convergence and remove Fig C1. Is the value of 390 chosen based on this Figure and the fact that it is stable or are there other motivations?

There are 50 times of iterations before the convergence is reached according to the rate of decline of J. J is reduced from an initial value of 6585.2 to a stabilized value of 73.6.

We think the figure is important for the demonstration of how fast J is reduced. Thus, we have elected to keep the figure (Fig. 2).

42. Page 12, Line 6: It becomes clearer if the short appendix C is just put into the text here.

Adjusted.

43. Page 12, Line 11: “inverted emission” is not the correct term. The concentrations are inverted to get the emissions. This “emission inversion” and “inverted emissions” is appearing in many places in the text.

Changed throughout the text.

44. Page 12, Line 11-12: What is the value of error on the lifetime? I suggest mentioning also the values of the calculated errors in the text.

As described on page 15 line 11-14,

“The error in the lifetime is derived from the errors in NO_x loss (estimated in Appendix C) and NO_2 VCDs, according to the common manner of error synthesis.”

45. Page 14, line 1: inverted => derived

Changed.

46. Page 14, line 14: Since there is a lot of agriculture in the YRD region a soil contribution of 0.9% seems very small and needs some explanation. A discussion on biomass burning emissions (which occur in the agricultural regions) can be helpful here as well.

The soil emissions in GEOS-Chem already account for the effects of both fertilizer and natural soil. We cannot conclude whether the relative contribution of soil emissions (to the total) has been underestimated, because of the dominant emissions from power plants, transportation, industry and residential activities.

We have clarified that biomass burning is part of the sources of our derived emissions. In Sect. 4.2 where we compare our derived "anthropogenic" emissions with other anthropogenic inventories, the GFED v4 biomass burning inventory is adopted to be subtracted from our derived emissions.

47. Page 15, Line 1: Figure 2e is mentioned without discussing 2a-d.

Figure a-d have been discussed before.

Now we have re-arranged the figures. Additional figures have been added, considering comments from both referees.

48. Page 15, Line 13: Please mention the basis of the coloring of Fig 2f.

As stated on page 18 line 20-22, The data points are colored to indicate the different ranges of VCDs at individual grid cells.

49. Page 15, Line 19: Why are the emissions not directly compared to bottom-up inventories instead of these proxies that are used in the bottom-up inventories. For example, a comparison with the MarcoPolo-Panda or the Zhao et al. inventory can give more insights.

In Sect. 4.3 we compare our emissions with other inventories besides MEIC.

50. Page 17, Line 5-6: To separate the anthropogenic emissions, GEOS-Chem is used to calculate soil emissions. What are the uncertainties of the soil emissions calculated by GEOS-Chem?

We have discussed the errors in soil emissions and biomass burning emissions in Sect. 4.2 on page 21 line 13-19:

"Soil emissions are calculated by the nested GEOS-Chem (Fig. 7c), with the uncertainties assumed to be within 50% (Wang et al., 1998; J. Yienger and Ii Levy, 1995). Biomass burning emissions (Fig. 7b) are taken from the Global Fire Emissions Database (GFED4; www.globalfiredata.org/data.html; last access: 2019/7/10) (Giglio et al., 2013), with the uncertainties estimated to be within 10% over the YRD (Giglio et al., 2009; Giglio et al., 2013). Summed over the study domain, the soil sources contribute about 0.5% of our emissions while biomass burning contribute about 5.1%."

51. Page 17, Line 6: Figure 3ows?

Typo. Corrected.

52. Page 17, Line 8: Comparing Figure 3e and 3f is only useful if they are at the same resolution. Thus, Figure 3e should be regrided to the coarser resolution of Figure 3f.

All data are presented on 0.05°×0.05° grid.

53. Page 18, Lines 6-15: There is some repetition of the text of the previous sections

Rephrased.

54. Page 18, Line 19-20: I would remove the last sentence about the programming language, which is not very relevant in a scientific paper

We have elected to keep the sentence, because we consider that programing with Python, a popular and easily used language, is an important feature that the potential users of our codes may appreciate.

55. Page 22: Line 17: Since one observation of the satellite is used in several grid cells, I doubt if the assumption that covariance matrices are diagonal matrices is correct. A discussion is needed here.

Since we use several pixels to get the mean VCD for each grid cell, and grid cells nearby each other may shares the same pixels partly although weight differently. Therefore, we admit that making the covariance matrix to be diagonal may be an imperfect assumption, although a similar assumption has been used in many previous studies (Keiya and Itsushi, 2006; Cao et al., 2018).

To partly account for the uncertainty lead by such approximation, we assume relatively high errors in the VCDs, as shown in Sect. 2.2:

On page 8 line 5-13: "For the purpose of emission estimate, we assume that the error of VCD at a satellite pixel (σ_p) contains an absolute error of half of the mean VCD over the domain (i.e.,1.9×10^{15} molecules cm^{-2}) and a relative error of 30% (Lin et al., 2010;Boersma et al., 2011;Lin et al., 2015a;Beirle et al., 2011). We further add in quadrature an additional error (σ_g) when a satellite pixel is projected to the grid cells at a finer resolution; this error is important in the urban-rural fringe zone. For a given grid cell, σ_g is set to be 50% of the standard deviation of VCDs at its eight surrounding grid cells. Sampling over multiple days reduces the random error by a factor of $s = \left(\sqrt{(1-c)/n + c}\right)$, where c represents the fraction of systematic error (assumed to be 50%) and n the number of days with valid data (Eskes et al., 2003; Miyazaki et al.,

2012). Thus, the total error for the temporally averaged VCD at a given grid cell is $\sigma_s = \sqrt{\left(\sigma_p^2 + \sigma_g^2\right)} \cdot s$."

We have also summarized the limitation in the conclusion section:

On page 25 line 16-18: "The adjoint model assumes the observational error covariance matrix to be diagonal, without fully considering the effect of correlations between individual grid cells."

56. References: Most references contain many spelling errors and omissions.

Checked.

57. Figure 2d: The lifetime is very short over the ocean, contradicting to what is usually seen in the literature.

We agree that the lifetime over the ocean might be underestimated and the emission there is therefore overestimated. Some discussions are added on page 17 line 6-11 and on page 25 line 12-13.

58. Figure 2e: Although the gridding is on 0.05 degree resolution the actual spatial resolution of this image seems much lower. An indication if the intrinsic resolution can be obtained from the largest gradients in the emissions. I cannot detect clear structures with a 0.05 degree resolution. One would at least expect some power plants to show up as clear spots in this region.

Maybe the method is still limited to the OMI resolution. I would like to see some discussion about this.

Please see our response to general comment 8.

59. Figure 2f: The plot is more logical when the x-axis and y-axis are reversed. I also suggest drawing a line for the 100% relative error in this plot as a helpline to guide the eye.

Changed.

60. Figure 2 caption: What are the magnitudes of POMINO that are mentioned. In Figure 2f it is too small to see.

Changed.

61. Figure 3e: This has to be regrided to the resolution of 2f for comparison.

Adjusted.

62. Figure 3: I miss information on power plants, which are a major source of NO_x.

See our response to general comment 8.

63. Figure 4: The crosses in the plot, indicating the amount of grid cells, are too small.

The crosses have been deleted for simplicity.

64. Figure D1: I do not understand why we need two colors for the dots.

The blue points stand for the grid cells where the VCDs is lower than 5×10^{15} molecules cm^{-2}, and the evaluated local net sources at these grid cells are used to derive the relation between the NO_x loss and NO_2 VCDs by fitting the fixed formula. An explanation is added on page 30 line 7.

65. Figure D2: The lifetime depends a lot on chemistry, temperature and precipitation. Therefore, the plot seems very simplified.

We agree, but this is the best we can do without involving a computationally much costlier 3-D chemical transport model. We note that previous studies with simplified models have often assumed a single value for lifetime for each city or other emission sources (Beirle et al., 2011; Liu et al., 2016).

We have added a discussion of the limitations of our method, including about the lifetime, in the revised conclusion section on page 25 line 18-20:

"Also, we assume a spatially uniform relationship between NO_2 VCDs and NO_2 lifetimes, which may lead to an underestimate in the lifetimes at low-NO_2 locations over the eastern sea."

High-resolution (0.05°×0.05°) NO_x emissions in the Yangtze River Delta inferred from OMI

Hao Kong[1], Jintai Lin[1], Ruixiong Zhang[1*], Mengyao Liu[1], Hongjian Weng[1], Ruijing Ni[1], Lulu Chen[1], Jingxu Wang[1], Yingying Yan[1], Qiang Zhang[2]

[1]Laboratory for Climate and Ocean-Atmosphere Studies, Department of Atmospheric and Oceanic Sciences, School of Physics, Peking University, Beijing 100871, China

[2]Ministry of Education Key Laboratory for Earth System Modeling, Department of Earth System Science, Tsinghua University, Beijing 100084, China

Correspondence to: Jintai Lin (linjt@pku.edu.cn)

[*] Now at: School of Earth and Atmospheric Sciences, Georgia Institute of Technology, Atlanta, GA, USA

Abstract

Emission datasets of nitrogen oxides (NO_x) at high horizontal resolutions (e.g., ~~0.05° × 0.05°~~0.05°×0.05°) are crucial for understanding human influences at fine scales, air quality studies, and pollution control. Yet high-resolution emission data are often ~~lacking~~missing or contain large uncertainties especially for the developing regions. Taking advantage of long-term satellite measurements of nitrogen dioxide (NO_2), here we develop a computationally efficient method to ~~invertingestimating~~ NO_x emissions in major urban areas at the ~~0.05° × 0.05°~~0.05°×0.05° resolution. The top-down inversion method accounts for the nonlinear effects of horizontal transport, chemical loss, and deposition. We construct a model called PHLET (2-dimensional Peking University High-resolution Lifetime-Emission-Transport ~~(PHLET)~~ model~~,~~), its adjoint model (PHLET-A), and a Satellite Conversion ~~Metrix~~Matrix approach to relate emissions, lifetimes, simulated NO_2, and satellite NO_2 data. The inversion method is applied to summer

months of 2012–2015 in the Yangtze River Delta area (YRD, 118°E-123°E, 29°N-34°N), a major polluted region of China, using the POMINO NO_2 vertical column density product retrieved from the Ozone Monitoring Instrument. A systematic analysis of inversion errors is performed, including using an Observing System Simulation Experiment-like test. Across the YRD area, the ~~inverted~~ summer average ~~emission ranges~~emissions obtained in this work range from 0 to ~~12.0~~15.3 kg km^{-2} h^{-1}, and the ~~lifetime~~lifetimes (due to chemical loss and deposition) from ~~1.4~~0.6 to 3.~~6~~3 h. Our ~~inverted~~ emission dataset reveals fine-scale spatial information ~~tied~~related to nighttime light, population density, road network, ~~and~~ maritime shipping~~.~~, and land use (from a Google Earth photo). We further compare our emissions with multiple inventories. Many of the ~~inverted~~ fine-scale emission ~~features~~structures are not well represented or not included in the widely used Multi-scale Emissions Inventory of China~~. Our inversion method can be applied to other regions and other satellite sensors such as the TROPOspheric Monitoring Instrument.~~ (MEIC).

1. Introduction

Nitrogen oxides (NO_x = NO + NO_2) are a main precursor of particulate matter, ozone, and other atmospheric pollutants. NO_x strongly influence the atmospheric oxidative capacity, affect the climate, and are toxic to many organisms. NO_x are emitted from natural ~~(soil, biomass burning, and lightning)~~ and anthropogenic ~~(transportation, energy, industry, and residential)~~ sources ~~(Lin, 2012).~~(Lin, 2012). Over the past decade, China has experienced rapid growth in the Gross Domestic Product (GDP, by 8.3% a^{-1} on average from 2008 to 2017), fossil fuel consumption (by 5.5% a^{-1} from 2007 to 2015), and urbanization (National Bureau of Statistics of China, http://data.stats.gov.cn/)~~.~~. These socioeconomic changes have been accompanied by a rapid change in NO_x emissions in the urban and surrounding areas. With the large and continuously increasing urban population and motor vehicles, NO_x pollution is particularly severe in large cities such as Beijing and Shanghai ~~(Barnes and Rudziński, 2013;Lin et al., 2016).~~(Barnes and Rudziński, 2013;Lin et al., 2016). Many coastal cities like Shanghai have also experienced enormous growth in the shipping business ~~and resulting~~. Therefore, pollution along the coastal line has become a

serious problem associated with the ~~growing volume~~growth of global economic trade~~. Emissions~~; and emissions from seaborne transport play an increasingly important role in the global air pollution ~~(Fu et al., 2017).~~(Fu et al., 2017). Understanding the urban pollution and its environmental impacts requires accurate quantitative knowledge ~~on~~of NO_x emissions at a very high horizontal resolution~~,~~ (e.g., 0.05°×0.05°), which is ~~still~~typically lacking especially for the developing countries.

Gridded bottom-up emission inventories typically use spatial proxies (like population and GDP) to allocate provincial-level emission values ~~to individual locations (Zhao et al., 2011;Janssens-Maenhout et al., 2015), which~~, which are derived from activity statistics and emission factor data, to individual locations (Zhao et al., 2011; Janssens-Maenhout et al., 2015; Zhao et al., 2015). Such a gridding method may lead to large uncertainties at high resolutions (Zhao et al., 2011; Zheng et al., 2017; Geng et al., 2017)~~.~~, because the mismatch between proxies and emissions becomes more significant and emitting facilities are harder to allocate accurately as the resolution increases (Zheng et al., 2017). For a small area, emission factors and activity data of the major sources can be collected by on-site surveys to allow construction of a high-resolution inventory (Zhao et al., 2015; Granier et al., 2019), such as Zhao et al. (2015) for Nanjing. However, on-site surveys are extremely time consuming and resource demanding, difficult to be applied to a large domain in a timely manner.

Top-down inversion using satellite retrieval products of tropospheric vertical column densities (VCDs) of nitrogen dioxide (NO_2) is a widely used independent estimate of NO_x emissions (Martin et al., 2003; Stavrakou et al., 2008; Lin et al., 2010; Mijling and R., 2012; Gu et al., 2014; Beirle et al., 2015; Miyazaki et al., 2016; Ding et al., 2017a)~~.~~. Top-down inversion typically provides the total emission data, although emissions from individual sources can be further derived by integrating a priori data (often from bottom-up inventories) about source-specific information such as diurnal and seasonal variabilities (e.g., Lin et al., 2010; Lin, 2012) and spatial variabilities (Timmermans et al., 2016).

The traditional top-down methods based on local mass balance (LMB) or its variants assume a weak effect of horizontal transport (Martin et al., 2003; Lamsal et al., 2011; Lin, 2012; Gu et al., 2014; Boersma

et al., 2015). These algorithms work relatively well at low resolutions (> 50 km) given the relatively short lifetime of NO_x (hours to 1 day), but may introduce large uncertainties when applied to higher resolutions – for example, emissions in the rural-urban fringe zone cannot be identified accurately. The Adjoint Model and Kaman Filter methods better account for horizontal transport, although their applicability is limited by expensive computational costs ~~(Stavrakou et al., 2008;Mijling and R., 2012;Miyazaki et al., 2016;Qu et al., 2017;Ding et al., 2017a). These more sophisticated methods are typically applied to limited time periods, limited spatial domains, and/or low horizontal resolutions (Gu et al., 2014;Ding et al., 2017b;Miyazaki et al., 2012;Stavrakou et al., 2008;Qu et al., 2017;Huang et al., 2014).~~. These more sophisticated methods have often been applied to relatively short time periods (e.g., Gu et al., 2016 for one month), small spatial domains (e.g., Tang et al., 2013 in Texas), and/or at coarse horizontal resolutions (e.g., Miyazaki et al., 2012 at T41 grid, i.e.; ~2.8°, and Stavrakou et al., 2008 at 5°×5°). Top-down estimates can be further combined with bottom-up inventories and spatial proxies to increase the spatial resolution, such as from 0.25°×0.25° in the DECSO derived emissions to 0.01°×0.01° for 2014 during the MarcoPolo Project (Hooyberghs et al., 2016; Timmermans et al., 2016) and similar inventories over Qatar and South Africa (Maiheu and Veldeman, 2013). The LMB, Adjoint Model and Kaman Filter approaches normally use 3-dimentional chemical transport models (CTMs) to relate emissions to VCDs. ~~With a few exceptions (Lin et al., 2012;Stavrakou et al., 2013),~~ CTM-based studies typically provide an estimate of the ~~uncertainties~~overall model error, although Lin et al. (2012) and Stavrakou et al. (2013) present errors in ~~CTMs are not often assessed comprehensively due to expensive computational costs.~~the individual model processes (e.g., key chemical reactions and meteorological parameters). A computationally low-cost method for space-based high-resolution (0.05°×0.05°) NO_x emission ~~inversion~~estimate will be helpful for understanding the urban pollution and its trends and variability. ~~This is particularly true with the advent of fine spatial resolution satellite sensors such as the TROPOspheric Monitoring Instrument (TROPOMI).~~

This study presents a computationally low-cost space-based top-down approach to ~~constructing~~construct high-resolution NO_x emission ~~inventory~~inventories for ~~the~~ urban and surrounding areas. The approach is

applied to the Yangtze River Delta (YRD) area (118°E-123°E, 29°N-34°N, which includes Shanghai, Nanjing, Hangzhou and 15 other ~~13~~ cities) on a 0.05°×0.05° grid, using the POMINO NO_2 VCD data retrieved from the Ozone Monitoring Instrument (OMI). We derive the average NO_x emissions for the summer months (June, July, and August) of 2012–~~2016~~2015. We construct a model called PHLET (2-dimensional ~~(2-D)~~ Peking University High-resolution Lifetime-Emission-Transport ~~(PHLET) model~~) and its adjoint model (PHLET-A) to facilitate the emission ~~inversion~~estimate. The ~~concentration-dependent lifetime~~lifetimes of NO_x ~~is~~are estimated as well, in order to account for the nonlinear NO_x chemistry.

Section 2 presents the data and method for top-down inversion of high-resolution NO_x ~~emission inversion.~~emissions. Inversion uncertainties are analyzed explicitly. ~~We also test the~~Section 3 presents spatial distributions of NO_2 VCDs, the derived local net sources (which are used subsequently to derive NO_x emissions and lifetimes), NO_x lifetimes, and their uncertainties. Section 4 analyzes the top-down emission data estimated here, including comparisons with spatial proxies (population density, night light brightness, power plant locations, road network, marine shipping routes, and a Google Earth photo for land use indication), the Multi-scale Emissions Inventory of China (MEIC) (Zheng et al., 2014; Liu et al., 2015), the DECSO top-down emissions (Mijling et al., 2013; Ding et al., 2017b), and the MarcoPolo emissions (Hooyberghs et al., 2016; Timmermans et al., 2016). Section 5 tests our inversion method by applying it to the NO_2 VCDs simulated by the GEOS-Chem CTM, in a manner similar to the Observing System Simulation Experiment (OSSE). ~~Section 3 presents the top-down estimate of NO_x emissions, lifetimes, and their uncertainties. Comparison with the Multi-scale Emissions Inventory of China (MEIC) is also provided. Section 4~~Section 6 concludes the study.

2. Data and Method

2.1. A general framework to retrieve NO_x emissions at a high resolution

The high-resolution NO_x emission retrieval framework consists of multiple steps~~.~~, as illustrated in the flowchart (Fig. 1). First~~,~~ (Sect. 2.2), the POMINO NO_2 VCD data over summer 2012–~~2016~~2015 are

averaged on a 0.05°×0.05° grid, using a special oversampling technique that preserves the finest spatial information possible. A Satellite Conversion Matrix (SCM), which will be applied to PHLET simulated NO_2 VCDs at the second step, is also calculated based on the OMI pixel parameters.

Second~~,~~ (Sect. 2.3), the PHLET model is constructed to simulate the local net source (i.e., emission – loss) and horizontal transport of NO_2 ~~VCD~~VCDs on the 0.05°×0.05° grid. ~~A Satellite Conversion Matrix (SCM) approach~~The SCM is ~~used for spatial conversion between the PHLET grid space and the~~ then applied to PHLET simulated VCDs to mimic how each satellite pixel ~~space.~~ averages the spatial distribution of NO_2, in order to ensure the spatial sampling consistency between PHLET and POMINO. This process is needed because satellite pixels represent the NO_2 spatial distribution at a coarser (than PHLET) resolution with irregular shapes of individual pixels.

Third~~,~~ (Sect. 2.4), the PHLET-A adjoint model is constructed to, together with PHLET~~, invert~~ and POMINO VCDs, derive the local net source ~~from satellite NO_2 VCD data.~~ at each 0.05°×0.05° grid cell. We construct a cost function to quantify the difference between the distribution of POMINO VCDs and that simulated by PHLET at the 0.05°×0.05° grid. The inversion process to derive the local net sources is equivalent to minimization of the cost function.

Finally~~,~~ (Sect. 2.5), the emission and lifetime of NO_x at each 0.05°×0.05° grid cell is derived from the ~~inverted~~ local net source term, by ~~assuming~~fitting a ~~fixed~~ formula ~~within the small study domain~~ for the nonlinear relationship between ~~lifetime and VCD. A~~lifetimes and VCDs. The formula is assumed to be fixed, i.e., the relationship is applicable to all grid cells within the small study domain.

Furthermore, a rigorous error analysis for the framework and models is ~~also~~ conducted~~, including using~~ (Sect. 2.6). This analysis is complemented by an OSSE-like test~~.~~ based on the GEOS-Chem simulated distribution of NO_2 VCDs (Sect. 5).

Our inversion method explicitly accounts for horizontal transport and the nonlinear relationship between ~~NO_x emissions,~~ lifetimes~~,~~ and NO_2 VCDs. With a few reasonable assumptions, the method is

computationally efficient, suitable for speedily conducting high-resolution emission ~~inversion~~estimates in multiple areas and across a long time period~~. In the case of YRD here, with~~ (2012-2015 in this study). Both PHLET and PHLET-A are numerically solved based on FEniCS, a popular open source solver (Farrell et al., 2012; Funke and Farrell, 2013; Alnaes et al., 2015). With one computational core (Intel® Xeon® Gold 6130 CPU @ 2.10GHz), ~~the inversion calculation~~derivation of NO_x emissions over the YRD here takes ~~about 36 hours~~less than one hour after necessary input data are prepared. Applying the framework to multiple areas would take a similar amount of time by using one computational core for each area.

2.2. Tropospheric NO_2 VCDs retrieved from OMI

~~OMI is a UV/VIS nadir solar backscatter spectrometer on board the Aura satellite. OMI provides daily global coverage. Each complete swath of OMI consists of 60 ground pixels, the sizes of which increase from 13 km × 24 km at nadir to about 40 km × 150 km at the swath edge in accordance to the view zenith angle (VZA) from 0° to 57° (de Graaf et al., 2016).~~

OMI is a UV/VIS nadir solar backscatter spectrometer on board the Aura satellite (Levelt et al., 2006). OMI provides daily global coverage. Each complete swath of OMI consists of 60 ground pixels, the sizes of which increase from 13 km × 24 km at nadir to about 40 km × 150 km at the swath edge in accordance to the view zenith angle (VZA) from 0° to 57° (de Graaf et al., 2016).

We use Level-2 tropospheric NO_2 VCD data from ~~the~~ POMINO (Peking University Ozone Monitoring Instrument NO_2 product) (Lin et al., 2014; Lin et al., ~~2015~~2015a). As described in detail in Lin et al. (2014; 2015), POMINO is an OMI-based regional NO_2 product that includes a number of important features. Briefly, POMINO adopts the tropospheric slant column density (SCD) data from DONIMO v2 and conducts an improved calculation of tropospheric air mass factors (AMFs) and VCDs (i.e., VCD = SCD / AMF) ~~(Boersma et al., 2011)~~(Boersma et al., 2011). Key features of the POMINO algorithm include explicit representation of aerosol scattering and absorption (by combining aerosol data from daily nested GEOS-Chem (at 0.3125° long. × 0.25° lat.) simulations and monthly MODIS/Aqua aerosol optical

depth (AOD) data), explicit representation of the angular dependence of surface reflection, high-resolution NO_2 profiles from GEOS-Chem (at 0.3125° long. × 0.25° lat.), consistent retrievals of clouds (a prerequisite for the NO_2 retrieval) and NO_2, and use of a parallelized, LIDORT-driven AMFv6 package. POMINO NO_2 VCDs are consistent with ground-based MAX-DOAS data (Liu et al., ~~2018b~~2019).

To better relate NO_x emissions to NO_2 VCDs at the 0.05°×0.05° resolution, we only employ the NO_2 data in summer (June, July, and August), in which season the ~~lifetime~~lifetimes of NO_2 ~~is~~are the shortest (a few hours). We combine data over 2012–~~2016~~2015 to increase the sample size. The change in NO_2 VCD from June to August is relatively small, reducing the effect of intra-seasonal variability when ~~inverting~~deriving NO_x emissions from summer mean NO_2 VCDs. We screen out the 30 outer pixels with VZA larger than 30° (cross-track width larger than 36 km) that greatly smear the spatial gradient of NO_2, pixels with cloud radiance fraction exceeding 50%, and pixels with AOD larger than 3 (i.e., when the aerosol data used in the NO_2 retrieval are unreliable~~). We also exclude data with raw anomaly problems (http://projects.knmi.nl/omi/research/product/rowanomaly-background.php).~~ and the NO_2 retrieval is subject to an excessive error) (Lin et al., 2014;Lin et al., 2015b;Liu et al., 2018a). We also exclude data with raw anomaly problems (http://projects.knmi.nl/omi/research/product/rowanomaly-background.php). After data screening, we obtain valid data from 22,007 pixels. We then convert the pixel-specific Level-2 data to the 0.05°×0.05° grid.

To convert from the satellite ~~pixel space~~pixels to the 0.05°×0.05° grid ~~space~~cells, we use an oversampling method that employ satellite data on multiple days to enhance the horizontal resolution~~(Zhang et al., 2014)~~ (Zhang et al., 2014). For each 0.05°×0.05° grid cell, we average all pixels covering the grid cell from all valid days, using area-based weighting. The oversampling approach takes advantage of the fact that the exact ~~footprint~~location of the OMI ~~instrument~~footprint slightly changes from one day to another, so does the exact location of the footprint of ~~a satellite~~an OMI pixel at a given VZA. Thus, sampling from multiple days increases the horizontal resolution of data. Our oversampling approach is different from ~~Fioletov et al., who~~previous studies, which filled a grid cell with data from pixels within a certain distance (e.g., 30

km~~), which implied a~~) and would result in spatial smoothing (Fioletov et al., 2011; Krotkov et al., 2016; Sun et al., 2018).

For the purpose of emission ~~inversion~~estimate, we assume that the error of VCD at a satellite pixel (σ_p) contains an absolute error of ~~0.5×10^{15}~~half of the mean VCD over the domain (i.e., 1.9×10^{-15} molecules cm^{-2}) and a relative error of 30% (Lin et al., 2010; Boersma et al., 2011;~~Lin et al., 2015;~~ Beirle et al., 2011; Lin et al., 2015a). We further add in quadrature an additional error (σ_g) when a satellite pixel is projected to the grid cells at a finer resolution; this error is important in the urban-rural fringe zone. For a given grid cell, σ_g is set to be ~~15~~50% of the standard deviation of VCDs at its eight surrounding ~~eight~~ grid cells. Sampling over multiple days reduces the random error by a factor of $s = \left(\sqrt{(1-c)/n + c}\right)$, where c represents the fraction of systematic error (assumed to be 50%) and n the number of days with valid data (Eskes et al., 2003; Miyazaki et al., 2012). Thus, the total error for the temporally averaged VCD at a given grid cell is $\sigma_s = \sqrt{(\sigma_p^2 + \sigma_g^2)} \cdot s$.

2.3. The PHLET model simulation

~~We construct the PHLET model on the $0.05° \times 0.05°$ grid to interpret the relationship between local net source (emissions - loss), horizontal transport, and VCD of NO_2 in a 2-D gridded space (Eq. (1)) in the sense of long-time average. PHLET simulates the horizontal transport of NO_x through a time averaged advection process and an "effective" diffusion process, which represents the residual from the temporally averaged advection. The model assumes a horizontally homogeneous vertical shape of NO_2 concentrations, and that NO_2 is concentrated near the surface (Beirle et al., 2011). The assumption is implicitly used in many previous studies for polluted areas (Liu et al., 2016;Beirle et al., 2011). The corresponding uncertainty in the modeled NO_2 VCDs is set as 15% (Lin et al., 2014;Boersma et al., 2011).~~

~~Although lightning emissions, biomass burning emissions, aircraft emissions, and the vertical transport can lead to NO_2 at higher altitudes over the YRD area, the amount of NO_2 aloft is much smaller than NO_2 near the ground due to large anthropogenic pollution emitted from the ground (Lin, 2012). We regard NO_2 aloft as the regional background, and do not include it in Eq. 1 – as such, PHLET accounts for anthropogenic and soil NO_x emitted from the surface but not other types of emission sources. [For NO_x near the ground in the YRD area, the contribution of lightning, biomass burning, and aircraft emissions is negligible compared to the major anthropogenic (energy, industry, transportation, residential) sources.] To ensure the consistency between PHLET and OMI NO_2 data, we assume the background value to be half of the minimum OMI NO_2 VCD among all grid cells (i.e. 0.54×10^{15} molecules cm^{-2}), and then subtract the background value from the gridded OMI data when comparing with PHLET simulations.~~ We construct the PHLET model on the 0.05°×0.05° grid to interpret the relationship between local net source (i.e., emission – loss), horizontal transport, and VCDs of NO_2 in a 2-D gridded space (Eq. 1) in the sense of long-time average. PHLET simulates the horizontal transport of NO_x through a time averaged advection process and an "effective" diffusion process, which represents the residual from the temporally averaged advection. The vertical distribution is simplified as in Sect. 2.3.2. The loss process of NO_x is represented based on the lifetime.

2.3.1 Governing equation of PHLET

PHLET is an equilibrium model for the local net source, VCDs and horizontal transport of NO_2 at each grid cell. ~~The corresponding uncertainty in the modeled NO_2 VCDs is set as 5%.~~

Equation ~~(~~1~~)~~ presents the governing equation in PHLET:

$$\frac{\partial C(x,y)}{\partial t} = r \cdot L(x,y) - \boldsymbol{V}(x,y) \cdot \nabla C(x,y) + \nabla \cdot (\mathbf{K}(x,y) \cdot \nabla C(x,y)) \cdot \left(\mathbf{K}(x,y) \cdot \nabla C(x,y)\right) = 0 \quad (1)$$

$C(x,y)$ represents the tropospheric NO_2 VCD (in molecules cm^{-2}) with due to sources over the regional background removed YRD. The value of $C(x,y)$ after the model reaches equilibrium ($\frac{\partial C(x,y)}{\partial t} = 0$ for every x and y) gives the distribution of NO_2 VCDs to at equilibrium ($\frac{\partial C(x,y)}{\partial t} = 0$ for every x and y). The discrete form of PHLET is set on the 0.05°×0.05° grid. The simulated VCDs will be compared applied with the SCM and compared to the gridded, OMI data (after the contribution of horizontally homogeneous regional background value excluded is subtracted from the OMI data. As such, we, see Sect. 2.3.2).

We assume a steady state of NO_2 in the PHLET model, and PHLET, although NO_2 observed by the satellite instrument may be in a transient state. We assign an uncertainty error of 15% to simulated $C(x,y)$ to account for the possibility that NO_2 may not be fully in steady state. possible range of NO_2 variability at the overpass time of the instrument. Also, combining data from multiple years to derive an averaged NO_2 distribution for simulation (rather than conducting the simulations for individual years and months) leads to an additional uncertainty, which is set to be 10%. % based on a comparison between the emissions estimated from multiple years together (here) and the average of emissions estimated from individual years (in a sensitivity test).

$L(x,y)$ represents the local net source term (in molecules cm^{-2} s^{-1}, equivalent to 2.63×10^{-12} kg km^{-2} h^{-1}) combining), which combines the effects of ground emissions (anthropogenic + soil + biomass burning; see discussion in Sect. 2.3.2), deposition, and chemistry of NO_x. At equilibrium, the domain average of modeled $L(x,y)$ reaches zero, become there are no horizontal fluxes into or out of the domain boundaries. $L(x,y)$ can be separated into an emission term, and a loss term:

$$L(x,y) = E(x,y) - \frac{C(x,y)}{r \cdot \tau(x,y)} \quad (2)$$

where $E(x,y)$ denotes the gridded ~~r~~ emissions of NO_x, and $\tau(x,y)$ the lifetimes associated with deposition and chemical loss. r represents the ratio of NO_2 over NO_x concentration. The daytime NO_x chemical system reaches equilibrium rapidly and r varies little (Beirle et al., 2011; Valin et al., 2013). We set r to be 0.76 with an uncertainty of 10% (Seinfeld et al., 2006; Beirle et al., 2011).

$\boldsymbol{V}(x,y) \cdot \nabla C(x,y)$ represents the time averaged advection term. ~~We set r to be 0.76 with an uncertainty of 10% (Seinfeld et al., 2006;Beirle et al., 2011).~~ $\boldsymbol{V}(x,y)$ denotes the mean wind vector (in m s^{-1}) averaged over summer 2012–2015. The wind data are taken from the European Centre for Medium-range Weather Forecasts (ECMWF) ERA5 dataset (see details in Sect. 2.3.3).

~~$L(x,y)$ can be separated into an emission term and a loss term:~~

~~$$L(x,y) = E(x,y) - \frac{C(x,y)}{r \cdot \tau(x,y)} \quad (2)$$~~

~~where $E(x,y)$ denotes the gridded emission of NO_x, and $\tau(x,y)$ the lifetime of NO_2 associated with deposition and chemical loss.~~

~~$\boldsymbol{V}(x,y) \cdot \nabla C(x,y)$ represents the time averaged advection term.~~ ~~$\boldsymbol{V}(x,y)$ denotes the mean wind vector (in m s^{-1}) averaged over summer 2012 – 2016. To solve the advection process, we follow the Walcek scheme (Walcek, 2000); the SHASTA scheme (Schere, 1983) leads to similar results.~~

$\nabla \cdot (\mathbf{K}(x,y) \cdot \nabla C(x,y))$ represents the diffusion term, where $\mathbf{K}(x,y)$ denotes the "effective" diffusion coefficient tensor (in m^2 s^{-1}). The diffusion term accounts for transport by the residual winds deviating from the temporally averaged wind vector $\boldsymbol{V}(x,y)$. Appendix A shows how to determine the diffusion coefficient ~~and solve the diffusion process.~~tensor.

2.3.2 ~~*The discrete form*~~*Vertical shape and regional background* of NO_2

PHLET assumes a horizontally homogeneous vertical shape of NO_2 concentrations, and that NO_2 is concentrated near the surface (Beirle et al., 2011). The assumption is implicitly used in many previous studies for polluted areas (Beirle et al., 2011; Liu et al., 2016; Liu et al., 2017). The corresponding uncertainty in the modeled NO_2 VCDs is set as 15% (Boersma et al., 2011; Lin et al., 2014).

Lightning emissions, biomass burning emissions, aircraft emissions, transport from neighboring regions, and convection can lead to NO_2 at higher altitudes over the YRD area. However, the amount of NO_2 aloft is much smaller than near-ground NO_2 due to large ground sources (Lin, 2012). Thus, we regard NO_2 aloft as the regional background, and do not include it in Eq. 1. Also, for near-ground NO_2 over the YRD area, the contribution of downward vertical transport is negligible compared to the contribution of ground sources. Aircraft emissions contribute little to the total ground source, because 78% of aircraft emissions occur at the high altitudes (9–12 km) (Ma and Xiuji, 2000). Therefore, PHLET only accounts for near-ground NO_2 from ground soil, biomass burning and anthropogenic sources (energy, industry, transportation, and residential).

To ensure the consistency between PHLET and OMI NO_2 data, we assume the background value to be half of the minimum OMI NO_2 VCD among all grid cells (i.e., 0.54×10^{15} molecules cm^{-2}), and then subtract the background value from the gridded OMI data when comparing with PHLET simulations. The corresponding uncertainty in the modeled NO_2 VCDs is set as 5%.

2.3.3 ~~*on the 0.05° × 0.05° grid.*~~ *Initial conditions, lateral boundary conditions, and wind data input*

To run PHLET, the NO_2 VCDs at the domain edges, as the lateral boundary conditions (LBCs), are set as the corresponding OMI NO_2 VCDs. For initial conditions, the VCD and the local net source at each grid cell inside the domain boundaries ~~is~~are set ~~to be~~as zero~~, and the local net source term is assigned to be a low value (0.02 kg km^{-2} h^{-1}, or 7.60×10^{9} molecules cm^{-2} s^{-1})~~.. The horizontal ~~distribution~~distributions of modeled NO_2 VCDs and local net sources at equilibrium ~~does~~do not depend on the initial conditions~~.

~~At equilibrium, the domain average of modeled $L(x,y)$ reaches zero, become there are no horizontal fluxes into or out of the domain boundaries~~.

For horizontal transport, we use 3-hourly wind fields from the ~~European Centre for Medium-range Weather Forecasts (~~ECMWF~~)~~ ERA5 dataset (https://confluence.ecmwf.int//display/CKB/ERA5+data+documentation; last access: 2018/7/2). The resolution of raw ERA5 data is 0.28125° on the reduced Gaussian grid, which is regridded to ~~0.05° × 0.05°~~0.05°×0.05° by using the online program offered by ECMWF (see Fig. ~~A1~~A). We adopt the mean wind field of the lowest 14 vertical levels (out of 157 levels in total); these 14 levels represent the altitudes from surface to about 500 m ~~(Hersbach and Dee, 2016;Beirle et al., 2011).~~(Beirle et al., 2011;Hersbach and Dee, 2016). Over the study period, the prevailing wind is northwesterly, and the wind speed is small over land (Fig. ~~A1~~A). For both zonal and meridional wind speeds, the uncertainty in the average wind speed is set to be 10%, which is similar to the temporal standard deviation of the wind speed~~.~~ and may partly account for the fact that lower-resolution wind data are used. We assess the model errors introduced by the uncertainties in the wind field and effective diffusion coefficients by Monte Carlo simulations~~; the~~ in which the wind speeds are changed according to their uncertainties. The resulting relative uncertainty in the modeled NO_2 VCDs is about ~~5~~20%.

2.3.4 Application of SCM

Re-mapping of PHLET simulated NO_2 VCDs in accordance to satellite pixels is important. Given the size of OMI pixels, the OMI NO_2 data smooth to some extent the actual horizontal distribution of NO_2. To ensure consistent spatial sampling between PHLET and OMI data, for each day we project the PHLET modelled NO_2 VCD data (in the original ~~0.05° × 0.05°~~0.05°×0.05° grid ~~space~~) to the satellite ~~pixel space~~pixels to mimic how OMI "sees" the ground, remove the pixels with invalid OMI data, and then project the model data back to the ~~0.05° × 0.05°~~0.05°×0.05° grid. The last two procedures are the same as done for OMI data. The whole process of grid conversion is done through the SCM approach

(Appendix B). Although PHLET simulates summer average NO_2 VCDs (rather than daily values), we repeat the grid conversion process for as many days as there are valid OMI data.

2.3.5 Summary of model errors

The model error σ_m is set to be the sum in quadrature of errors contributed by the abovementioned steady state assumption (15%), the time averaging over multiple years and months (10%), the assumption of horizontally constant vertical shape of NO_2 (15%), the NO_2/NO_x ratio (10%), the treatment of background NO_2 concentration (5%), and the error in the wind data and the calculation of effective diffusion coefficients (~~5~~20%).

2.4. PHLET-A: The adjoint model of PHLET

We construct the PHLET-A adjoint model to obtain an optimized horizontal distribution of the local net source term (L in Eq. ~~(~~1~~))~~) under the given OMI NO_2 VCDs, wind field, and other parameters. PHLET-A accounts for the complex nonlinear effects of 2-dimensional transport and loss processes. ~~We define a scalar cost function (Eq. (3)) to quantify the difference between OMI NO_2 VCDs and PHLET simulated NO_2 VCDs.~~

We first define a scalar cost function (Eq. 3) to quantify the difference between OMI NO_2 VCDs and PHLET simulated (and SCM applied) NO_2 VCDs.

$$J = (\boldsymbol{C^{OMI}} - \boldsymbol{C^{PHLET}})^T \mathbf{S_o^{-1}} (\boldsymbol{C^{OMI}} - \boldsymbol{C^{PHLET}}) \quad (3)$$

Because PHLET does not require a priori knowledge about the local net source, the cost function does not include the a priori term either. The vector $\boldsymbol{C}$ denotes gridded NO_2 VCDs. $\mathbf{S_o}$ denotes the observational error covariance matrix consisting of a satellite data error covariance matrix ($\mathbf{S_s}$) and a PHLET model error covariance matrix ($\mathbf{S_m}$): ~~, as derived in Appendix C.~~

~~Applying Lagrange identity and integrating by parts, we~~$\mathbf{S_o} = \mathbf{S_s} + \mathbf{S_m}$ (4)

For simplicity and following previous studies (Keiya and Itsushi, 2006; Cao et al., 2018), both $\mathbf{S_s}$ and $\mathbf{S_m}$ are assumed to be diagonal, with the diagonal elements set to be σ_f^2 and σ_m^2, respectively. Grid cells nearby may share the same pixels, although the area-based weights would be different. This means that nearby grid cells may not be fully independent, leading to a weakness of the diagonal assumption here. The associated uncertainty is partly accounted for by an error term based on the variability of NO_2 VCDs (i.e., 50% of the standard deviation across the surrounding grid cells; see Sect. 2.2).

We then derive PHLET-A and its initial and lateral boundary conditions by applying Lagrange identity and integrating by parts (Marchuk, 1994; Sandu et al., 2005; Martien et al., 2006; Hakami et al., 2007):

$$\frac{\partial \lambda(x,y)}{\partial t} + \nabla(\boldsymbol{V}(x,y)\cdot\lambda(x,y)) + \nabla\cdot(\mathbf{K}(x,y)\cdot\nabla\lambda(x,y)) = 0 \quad (45)$$

$$\lambda(x,y)|_{t=T} = \frac{\delta J}{\delta C(x,y)}|_{t=T} \quad (56)$$

$$\lambda(x,y)|_{boundary} = 0 \quad (67)$$

As shown in Eq. ~~Here, T stands for the time when the domain-wide NO_2 VCDs come to equilibrium, i.e., the start time of the adjoint simulation. By discrete adjoint sensitivity analysis, the gradient of cost function to emission is obtained:~~

~~$\frac{\delta J}{\delta L_{i,j}}$~~5, PHLET-A represents the sensitivity of cost function (J) to local net source ($\boldsymbol{L}$) where λ stand for the adjoint variable (Marchuk, 1994; Sandu et al., 2005). T stands for the time when the domain-wide NO_2 VCDs come to equilibrium, i.e., the start time of the adjoint simulation. By discrete adjoint sensitivity analysis, the gradient of J to $\boldsymbol{L}$ is obtained:

$$\frac{\delta J}{\delta L_{i,j}} = r\cdot\Delta x\cdot\Delta y\cdot\Delta t\cdot\sum_k \lambda_{i,j,k} \quad (78)$$

where the indices i, j, and k denote zonal, meridional, and time, respectively. The gradient is then used in an iterative optimization algorithm (Appendix C(shown by the blue arrows in Fig. 1) to minimize the cost function J, i.e., to minimize the weighted difference between model simulated and OMI NO_2. The iteration stops when J is reduced from an initial value of 7937 to a stabilized value below 390 (Fig. C1).

The numerical solution to obtain an optimized $\boldsymbol{L}$ that minimizes J is as follows. Given a starting point of $\boldsymbol{L}$, we derive a search direction by the Broyden-Fletcher-Goldfarb-Shanno (BFGS) method (Li and Fukushima, 2001; Bousserez et al., 2015). Then, by practicing backtracking line search based on the Armijo–Goldstein condition (Armijo, 1966), we obtain a revised $\boldsymbol{L}$ for the next iteration. The numerical calculation is done through FEniCS. It takes 50 iterations of PHLET and PHLET-A runs before the convergence is reached, according to the rate of reduction in J. The value of J is reduced from an initial value of 6585.2 to a stabilized value of 73.6 (Fig. 2).

The uncertainty of the optimized $\boldsymbol{L}$ is given by the Hessian of the cost function, which is approximated by the BFGS method (Brasseur and Jacob, 2017):

$$\boldsymbol{S} = 2 \cdot (\nabla^2_{\boldsymbol{L}} \mathrm{J})^{-1} \quad (9)$$

2.5. Deriving emission and loss from the local net source term

The optimized local net source term combines the contributions of emission (anthropogenic + soil) and loss (chemical loss + deposition). We further separate emission from loss by assuming a fixed formula within our small study domain for the nonlinear relationship between lifetimelifetimes and VCDVCDs of NO_2.

In the summertime daytime, the dominant sink of NO_x is reactions with the radicals to produce nitric acid and organic nitrogen species. The NO_x chemistry quickly reaches a steady state under high solar radiation and air temperature in the early afternoon (Murphy et al., 2006; Valin et al., 2013) when OMI passes over the YRD. The chemical lifetime of NO_x depends on the concentrations of NO_x and non-methane volatile organic compounds (NMVOC), radiation, temperature, and other factors. Within our small study domain,

we assume the net effect of all factors except NO_x concentrations to be spatially homogeneous. As such, the chemical lifetime of NO_x at steady state is a sole function of NO_x concentration (and thus NO_2 VCD, given the constant NO_2/NO_x ratio). Appendix ~~D~~C shows in detail how to deduce the chemical lifetime of NO_x from NO_2 VCD, to account for the effect of dry deposition, to separate emission and lifetime from the local net source term, and to quantify the errors involved ~~using Monte Carlo simulations~~.

2.6. Uncertainty estimate for ~~inverted~~top-down emissions

For a particular grid cell, ~~our inverted~~the derived emission is affected by the error involved in the ~~inversion~~estimate of L (embedded in satellite data and model simulations) and the error in the separation of emission and lifetime from L. The satellite data error σ_s is analyzed in Sect. 2.2. The model ~~induced~~related error σ_m is analyzed in Sect. 2.3. The error of L, σ_L, is connected with σ_s and σ_m through the adjoint simulation ~~(Sect. 2.4),~~ and is given by Hessian of the cost function J (~~Appendix C~~Sect. 2.4).

The error involved in the separation of emission and lifetime, σ_f , is contributed by the assumption on the NO_2/NO_x ratio ~~r~~r (Sect. 2.3.1), the simplified treatment of deposition and chemical processes of NO_x (Appendix ~~D~~C), and the assumed relationship between ~~lifetime~~lifetimes and ~~VCD~~VCDs (Appendix ~~D~~C). σ_f is estimated by ~~500 times of~~ data fitting of L ~~at individual grid cells~~with different fitting parameters (Appendix ~~D~~C).

Thus, the error in ~~inverted~~ emission, σ_e, is equal to the sum in quadrature of σ_L and σ_f, i.e., $\sigma_e = \sqrt{{\sigma_L}^2 + {\sigma_f}^2}$. The error in the ~~inverted~~ lifetime is derived from the errors in ~~a similar way~~NO_x loss (estimated in Appendix C) and NO_2 VCDs, according to the common manner of error synthesis.

~~Appendix E further presents an OSSE-like test to estimate the reliability of our emission inversion method, by examining to what extent the method can invert the emissions used in a nested GEOS-Chem simulation (0.3125° long. × 0.25° lat.) for summer 2014. Overall, the inverted emission data capture the mean value and spatial variability of the GEOS-Chem emissions, with a linear regression slope of 0.98, a~~

~~correlation of 0.93, and a mean bias of 0.25 kg km^{-2} h^{-1} (16%). This test suggests the high reliability of our inversion method.~~

3. High-resolution spatial distributions of NO_2 VCDs, local net sources, and lifetimes over the YRD

Figure ~~1a~~3a shows the number of days with valid OMI data in summer 2012–~~2016~~2015 over the YRD area on the 0.05°×0.05° grid. The number of days varies from about ~~14~~12 to ~~113 (56~~101 (48 on average). There is a "band" pattern in the spatial distribution, due to the difference in the number of satellite orbits covering each grid cell (not shown). This band pattern is not obvious in the distribution of OMI NO_2 VCDs (Fig. ~~1b~~3b), suggesting that the temporally averaged VCD values are less sensitive to the number of days (~~14~~12 or more) used for temporal averaging. There are fewer valid data in severely polluted locations. The effect of sampling size on the uncertainty in OMI NO_2 is accounted for in our study (Sect. 2.2).

Figure ~~1b~~3b shows the gridded horizontal distribution of OMI NO_2 VCDs. The background value (0.54×10^{15} molecules cm^{-2}) has not been removed. NO_2 VCDs are high over the major urban centers along the Yangtze River and the coastal line, especially Shanghai, Nanjing (Capital of Jiangsu Province), Hangzhou (Capital of Zhejiang Province), and the Ningbo-Zhoushan area (with intensive maritime shipping activities). The maximum VCD value exceeds ~~14 × 10^{15}~~ 16×10^{15} molecules cm^{-2} in north Shanghai. NO_2 VCDs are larger than ~~1 × 10^{15}~~1×10^{15} molecules cm^{-2} at all grid cells, reflecting the influence of local anthropogenic sources and/or pollution transported from nearby cities ~~(Cui et al., 2016).~~ ~~NO_2 VCDs are lower than 3 × 10^{15}~~(Cui et al., 2016). NO_2 VCDs are lower than 5×10^{15} molecules cm^{-2} along the boundaries of our study domain.

Across the grid cells, the absolute errors in OMI NO_2 VCDs are about ~~0.58–3.4 × 10^{15}~~1.6–4.9×10^{15} molecules cm^{-2} (Fig. ~~2a~~4a), and the relative errors are about ~~24%–54~~30%–157% (Fig. ~~2b~~4b). In general, the grid cells with larger NO_2 VCDs have larger absolute errors but smaller relative errors. Over the

eastern sea and the southwestern corner of the domain, NO_2 VCDs are relatively small (Fig. ~~1b~~3b), thus their absolute errors are small (Fig. ~~2a~~4a), but their relative errors are very large (Fig. ~~2b).~~ 4b).

Figure ~~1c~~4c shows the spatial distribution of the ~~inverted~~ local net source L (emission – loss). A positive (negative) value of L indicates that the emission is larger (smaller) than the loss. The values of L are the greatest (~~8.9~~11.7 kg km^{-2} h^{-1}) over the major urban areas with high NO_2 VCDs, and are low ~~(< 3.2~~(< -1.0 kg km^{-2} h^{-1}) in many areas with low NO_2 loadings. ~~However, the~~The values of L are the lowest ((~~-7.~~6.9) ~~(~~-2~~) (-3.2~~.0) kg km^{-2} h^{-1}) at places in the urban-rural fringe zones with NO_2 hotspots nearby; this feature reflects that NO_2 is transported from the urban centers and destroyed in the fringe zones. The absolute errors of L vary from 0.6 to 4.5 kg km^{-2} h^{-1}. The spatial correlation between the absolute errors of L (Fig. ~~2c) are highly consistent with~~4c) and those of the NO_2 ~~VCD~~VCDs (Fig. ~~2a), with a spatial correlation of 0.95.~~4a) is about 0.5. The absolute errors of L are notable in the urban-rural fringe zones where L is small but NO_2 VCD is high, because the deviation of L at these areas is very sensitive to errors in the assumed transport and loss process.

Figure ~~1d~~3d shows the ~~inverted lifetime~~derived lifetimes of NO_2 on the 0.05°×0.05° grid. The ~~lifetime ranges~~lifetimes range from ~~1.4~~0.6 to 3.~~6~~3 h across the study domain~~.~~, with an average of 2.0 h. The ~~lifetime is below 1.5~~lifetimes are about 0.6 h at grid cells with NO_2 VCDs of about ~~2 × 10^{15}~~ 1.6×10^{15} molecules cm^{-2}, increasing to ~~2.2~~0.8 h at grid cells with the lowest VCDs ~~(< 2 × 10^{15}~~ (around 1.0×10^{15} molecules cm^{-2}), and exceeding 3 h at many polluted grid cells, i.e., the urban centers. The ~~mean lifetime over the study domain~~nonlinear dependence of lifetimes on VCDs is ~~about 2.0 h.~~ expected from our inversion method (Appendix ~~D~~C). Appendix C further shows the chemical ~~lifetime~~lifetimes to be ~~1.7~~ 0.6~~.6~~ ~~–~~ 3.8 h and the deposition ~~lifetime~~lifetimes to be constantly at ~~7.8~~30.4 h across all grid cells. ~~The nonlinear dependence of lifetime on VCD is expected from our inversion method (Appendix D). The~~

Figure 4d shows that the absolute ~~uncertainty~~uncertainties in the ~~inverted lifetime is~~lifetimes are greater than 1.0 h at the NO_2 hotspot locations, between 0.~~75~~6 and 1.0 h over the eastern sea and the southwest of the study domain, and about 0.~~7~~4 h at many other locations ~~(Fig. 2d).~~. The lifetimes at high-NO_2

locations (up to 3.3 h) are consistent with previous studies, e.g., one single value of 4.7±1.4 h for Shanghai in summer 2005–2013 by (Liu et al., 2016). The short lifetimes at low-NO_2 locations over the eastern sea may be underestimated, due to the assumption that non-NO_2 factors (especially NMVOC) are spatially homogeneous within the study domain (Appendix C). In particular, the concentrations of NMVOC over the eastern sea may be overestimated by this assumption, based on the OMI formaldehyde data (De Smedt et al., 2015).

4. High-resolution spatial distribution of NO_x emissions over the YRD

4.1. Spatial distribution of ~~inverted~~ emissions

Figure ~~1e~~5a shows the ~~inverted~~derived horizontal distribution of summer 2012~~–2016~~2015 average NO_x emissions on the 0.05°×0.05° grid. The ~~inverted~~ emissions include the contributions of ground anthropogenic (energy, industry, transportation, and residential), soil and biomass-burning sources. As discussed in Sect. 4.3, soil emissions contribute little (0.~~9~~5%) to the total ~~emission~~emissions over the study domain~~.~~, and biomass burning contributes about 5.1%.

Figure ~~1e~~5a shows that NO_x emissions vary from 0 to ~~12.0~~15.3 kg km^{-2} h^{-1} across the grid cells. The highest emission value occurs in north Shanghai, close to Wusongkou where Shanghai Port is located, which has become the largest container terminal ~~all over~~in the world in 2010 ~~(Fu et al., 2012).~~(Fu et al., 2012). High emission values also occur at places along the Yangtze River and the coastal line. Along the Yangtze River, the highest emission value occurs in Nanjing City. Along the coastal line, there is an emission hotspot in the Ningbo-Zhoushan area. The general spatial distribution of ~~inverted~~ NO_x emissions is consistent with that of OMI NO_2 VCDs (correlation = 0.~~82~~69), reflecting the short ~~lifetime~~lifetimes of NO_x and thus a modest effect of horizontal transport. Nonetheless, emissions are much more concentrated at a few sparse locations than NO_2 VCDs are, and many locations near the emission hotspots have very low emissions but relatively large NO_2 VCDs, suggesting that the effect of horizontal transport cannot be ignored at such a high resolution.

Figure ~~2e~~5b shows the absolute ~~uncertainties~~errors of NO_x emissions at individual grid cells. The emission ~~uncertainty varies~~errors vary from 0.~~1~~7 to ~~1.~~4.5 kg km^{-2} h^{-1} across all grid cells. The largest uncertainty occurs in north Shanghai, corresponding to the highest VCD (Fig. ~~1b~~3b) and emission (Fig. ~~1e~~5a) values. The spatial pattern of absolute emission ~~uncertainties~~errors (Fig. ~~2e~~5b) is closer to the pattern of NO_2 VCDs (Fig. ~~1b~~3b, correlation = 0.~~91~~51) than to the pattern of emissions (Fig. ~~1e~~5a, correlation = 0.~~75). The emission uncertainties~~33). There are ~~spatially~~ more ~~homogeneous~~hotspots in the distribution of emission errors than in the distributions of VCDs and emissions~~ are~~, because the emission ~~uncertainties~~errors can be high at locations with low VCDs and emissions. The spatial pattern of emission ~~uncertainties~~errors is consistent with that of *L* ~~uncertainties~~errors (Fig. ~~2c~~4c, correlation = ~~0.85).~~1.0), indicating that the errors in deriving emissions from the local net sources are rather homogenous. Figure 5c further shows that the relative errors of emissions are high (> 100%) over low-emission locations but much lower over emission hotspots.

The scatter plot in Fig. ~~2f shows the emission uncertainty as a function of emission at each grid cell. Although the emission uncertainty tends to be higher when the inverted emission value increases,~~5d shows the relationship between absolute emission errors and emissions at individual grid cells. The relationship is highly nonlinear, and there is large data spread~~. The data spread reaches its maximum value when emissions are the lowest, declines~~ where the emissions are low. The data spread tends to be smaller when emissions exceed 5 kg km^{-2} h^{-1}. The emission errors tend to decrease as emissions increase until about 5 kg km^{-2} h^{-1}, after which the emission errors tend to increase with the increasing emissions~~, and is relatively small when emissions exceed 3 kg km^{-2} h^{-1}. The~~ . The data points in Fig. ~~2f~~5d are ~~further~~ colored to indicate the different ranges of VCDs~~ at individual grid cells. It is clear that the~~ , and they show that grid cells with ~~low emissions but high emission uncertainties have large~~ higher NO_2 VCDs~~. These grid cells are located in the urban-rural fringe zones with significant NO_2 pollution transported from nearby urban centers~~ have larger emission errors and smaller data spread.

4.2. ~~Comparing~~Comparison between our ~~inverted~~top-down emissions ~~with nighttime light, population density,~~ and ~~road network~~spatial proxies

This section compares our ~~inverted~~ NO_x emission dataset (Fig. 6b) with several spatial proxies widely used in bottom-up inventories, including nighttime light brightness (~~0.5′ × 0.5′,~~ Fig. ~~3a~~6c), population density (Fig. 6d), road network (Fig. 6e), ship route density (~~0.1° × 0.1°, Fig. 3b), and road network (Fig. 3c~~Fig. 6f), power plant locations (Fig. 6g), and a satellite photo from Google Earth that indicates the extent of land use (Fig. 6i). These proxies broadly represent the intensity of human activities and are highly related to NO_x emissions ~~(Geng et al., 2017)~~(Geng et al., 2017).

Figure ~~3a~~6c shows the spatial distribution of nighttime light brightness in 2012. The data are taken from Version 4 DMSP-OLS Nighttime Lights Time Series at a horizontal resolution of 0.5'×0.5' (https://www.ngdc.noaa.gov/eog/dmsp/downloadV4composites.html; last access: 2018/08/19). The brightness is represented digitally from 0 to 63 bits. The nighttime light reflects the intensity of household activity, commercial activity, and resource consumption (Elvidge et al., 2013). When regridded to ~~0.05° × 0.05°~~0.05°×0.05°, the spatial correlation between nighttime light brightness and NO_x emissions is about 0.~~70, i.e., the nighttime light brightness can explain 49% of the spatial variability in NO_x emissions in the YRD area.~~ 61 over land.

Figure ~~3b~~6d shows the population density data, which are taken from the Gridded Population of the World v4 (GPWv4) at a horizontal resolution of 0.1°×0.1° (http://sedac.ciesin.columbia.edu/data/collection/gpw-v4/sets/browse; last access: 2018/08/19) ~~(Center for International Earth Science Information Network - CIESIN - Columbia University, 2016).~~(Center for International Earth Science Information Network - CIESIN - Columbia University, 2016). This dataset provides population density data for every five years (2000, 2005, 2010, 2015, etc.). Data in 2012, 2013 and 2014 are estimated by fitting a natural spline to the 2000, 2005, 2010, and 2015 values. ~~Data in 2016 are estimated by fitting a natural spline to the 2005, 2010, 2015, and 2020 values.~~ The population density varies greatly from the urban centers to the countryside. In north Shanghai, the population density exceeds ~~5 × 10³~~3.5×10^3 km^{-2}. The NO_x emission hotspots match the population hotspots, and the lowest-emission

locations have little population. When regridded to ~~0.05° × 0.05°~~0.05°×0.05°, the spatial correlation between population densities and NO_x emissions is 0.~~52~~50 over land.

Figure ~~3c~~6e shows~~ our NO_x emissions overlaid with~~ the OpenStreetMap road network data (http://download.geofabrik.de; last access: 2018/6/27). The network includes both highways and local roads. In the southern areas (between 29°N and 31°N), the spatial distribution of NO_x emissions largely coincides with the road network. The spatial coincidence is less obvious in the north because of the influence of non-mobile sources. NO_x emissions are notable along the three major national highways connecting Jinhua City (one of the largest hubs of light industry products in China), Hangzhou City, and Ningbo City. NO_x emissions are also identifiable along the national highway from Hangzhou City to Huangshan City. Pairs of NO_x emissions and traffic hubs are located to the west of the Taihu Lake and in the urban centers. These results suggest the capability of our~~ inverted~~ emission dataset in capturing the contribution of traffic sources.

~~4.3. Comparing our inverted emission dataset to the MEIC inventory~~

~~This section compares our inverted emission data to the widely used MEIC anthropogenic bottom-up inventory over summer 2012–2016 (www.meicmodel.org; last access: 2018/7/2). The MEIC data are available at the 0.25° × 0.25° resolution. Because our emission data include the slight contribution of soil sources, we use the nested GEOS-Chem to calculate soil emissions (Fig. 3d), and then subtract these soil emissions from our data. Figure 3ows the resulting "anthropogenic" portion of our inverted emissions. Summed over the study domain, the soil sources contribute 0.9% of our inverted emissions.~~

~~Figures 3e and 3f show that compared to MEIC,~~Figure 6f shows the mean density of marine shipping routes over the eastern sea in 2016 (www.marinetraffic.com; last access: 2019/6/27). Over the northern parts of the eastern sea, the route density map shows certain north-south and northwest-southeast lines. High route densities are also evident close to the ports. These features are consistent with the distributions of NO_2 VCDs (Fig. 6a) and NO_x emissions (Fig. 6b, same as Fig. 5a).

The filled circles in Fig. 6g show the locations of coal-fired power plants in 2016 from Carbon Brief (www.carbonbrief.org; last access: 2019/6/27). The radius of a circle denotes the power generation capacity. Figure 6h further shows the GPED v1.0 bottom-up NO_x emissions for power plants on a 0.1°×0.1° grid in 2016. Coal-fired power plants in the YRD are normally near the urban centers, traffic lines or other sources. Our top-down NO_x emission map shows large emission values near the power plants (Fig. 6b), although it cannot isolate the sole contribution of power plants. At the GPED power plant locations, the correlation between our and GPED emissions reaches 0.26, due to the influence by non-power plant sources; note that the correlation between GPED emissions and POMINO NO_2 VCDs are only about 0.21.

Figure 6i shows a satellite photo taken in 2018 from Google Earth (earth.google.com; last access: 2019/7/4). The grey areas in the photo represent developed lands and the dark green areas indicate un-developed places. The majority of lands over the YRD have been developed. Although the lands over the southwest are less influenced by humans than the areas like Shanghai are, many places of the southwest have been developed as cities, towns and roads. This explains the spotted emission sources (Fig. 6b) retrieved from the satellite NO_2 VCDs.

4.3. Comparison between our emission dataset and other inventories

This section compares our emission data to several inventories for the region, including the MEIC bottom-up anthropogenic inventory in summer 2012–2015 (www.meicmodel.org; last access: 2018/7/2) (Liu et al., 2015;Zheng et al., 2014), the MarcoPolo (bottom-up + top-down hybrid) anthropogenic inventory in summer 2014 (www.marcopolo-panda.eu/products/toolbox/emission-data/; last access: 2019/5/4) (Hooyberghs et al., 2016;Timmermans et al., 2016), and the DECSO v5.1qa top-down emissions in summer 2012–2015 (www.globemission.eu/region_asia/datapage.php; last access: 2018/11/14) (Mijling et al., 2013;Ding et al., 2017b). MEIC and DESCO emission data are available at the 0.25°×0.25° resolution, and MarcoPolo are at 0.01°×0.01°. When compared with our emissions, these emission data are regridded to 0.05°×0.05°.

Our emission data and the DECSO inventory are top-down estimates and include the contributions of soil and biomass-burning sources. Thus, we estimate soil and biomass burning emissions from independent sources, and then subtract these emissions from our and DECSO emission datasets. Soil emissions are calculated by the nested GEOS-Chem (Fig. 7c), with the uncertainties assumed to be within 50% (J. Yienger and Ii Levy, 1995;Wang et al., 1998). Biomass burning emissions (Fig. 7b) are taken from the Global Fire Emissions Database (GFED4; www.globalfiredata.org/data.html; last access: 2019/7/10) (Giglio et al., 2013), with the uncertainties estimated to be within 10% over the YRD (Giglio et al., 2009;Giglio et al., 2013). Summed over the study domain, the soil sources contribute about 0.5% of our emissions while biomass burning contribute about 5.1%. Figure 7a shows the resulting "anthropogenic" portion of our emissions.

Compared with MEIC (Fig. 7d) and DECSO (Fig. 7e), our high-resolution anthropogenic emission dataset (Fig. 7a) provides much more detailed spatial information. Our dataset identifies the emission hotspots and their contrast with nearby low-emission areas (e.g., in the urban-rural fringe zones) better than MEIC ~~does~~and DECSO do. The contribution of mobile sources along the road network is clearer in our dataset. Our emission data contain sources over the nearby sea (i.e., from shipping), along the coastal line, and in the southwest of the domain, which are not included in MEIC. ~~In Hangzhou City~~Compared with DECSO, our dataset suggests ~~the highest~~higher emissions ~~to be to~~on the ~~south~~northern parts of ~~Qiantang River (marked~~the sea, which may be due to our underestimate of NO_x lifetimes (Sect. 3) and/or errors in ~~purple line in Fig. 1b), whereas~~ the ~~MEIC inventory suggests north. The total emission in MEIC is smaller than ours by 28.3% over the entire study domain and by 10.4% over land~~DECSO estimate.

~~Figure 4 compares emissions in several cities between our and MEIC inventory. A total of 14 cities within the domain are selected, and for each city the NO_x emissions are summed over the grid cells within the municipal administrative boundaries. The MEIC inventory is re-gridded to 0.05° × 0.05° for this purpose. Among the cities, emission values differ from -51.4% to +61.3% between the two datasets. In Shanghai, Suzhou and Wuxi, our dataset is lower than MEIC by 27.1%, 43.7%, and 51.4%, respectively. MEIC uses the industrial GDP as a spatial proxy to attribute provincial-level industrial emissions to individual~~

~~counties and grid cells (Geng et al., 2017). This may overestimate the emissions in Suzhou and Wuxi, since much of the industrial GDP in the two cities is contributed by high-tech industries with low emissions.~~

~~Figure 4 also shows that in Zhoushan, Huai'an and Yancheng, our dataset is higher than MEIC by 61.3%, 55.5%, and 55.1%, respectively. Zhoushan (around 30°N, 122°E) has many isles and marine ports, as identifiable on the nighttime light map (Fig. 3a). The marine ports in the Ningbo-Zhoushan area contribute about 10% of the total shipping emissions in China (Endresen et al., 2003;Fu et al., 2017). Our dataset accounts for emissions from marine shipping and ports, whereas MEIC does not.~~

~~Section 4.2 shows~~MarcoPolo emissions (regridded to 0.05°×0.05°, Fig. 7f) show more detailed spatial information than our emission dataset (Fig. 7a) does. This is because our top-down estimate is limited by the intrinsic resolution of NO_2 VCDs, i.e., our oversampling approach does not fully compensate for the large sizes of OMI pixels. Therefore, the large spatial gradient of NO_x emissions is smoothed to some extent in our dataset. On the other hand, the domain that MarcoPolo covers (118.135°E, 29.635°N – 122.125°E, 32.625°N) is much smaller than ours, and emissions of 9 cities (including Zhou Shan, Ningbo, Nantong, Hangzhou, Huai'an, Yancheng, Yangzhou, Taizhou, Shaoxing) and marine shipping emissions are not included in MarcoPolo.

At 0.05°×0.05°, the spatial ~~correlation at the 0.05° × 0.05° resolution~~correlations between our ~~inverted~~ NO_x emissions and ~~the~~spatial proxies ~~to be~~are 0.~~70~~61 for nighttime light brightness and 0.~~52~~50 for population density~~.~~ (Sect. 4.2). These values can be compared to the respective results for MarcoPolo on the 0.05°×0.05° grid (0.35 and 0.55, respectively). When regridded to ~~0.25° × 0.25°, the correlation becomes higher:~~ 0.25°×0.~~79~~25°, the correlations between our emissions and these spatial proxies become higher: 0.70 for nighttime light brightness and 0.~~63~~69 for population density. ~~As~~The weaker correlation at a higher resolution reflects that as the spatial resolution gets finer, the chance that NO_x emissions are collocated with population or nighttime light becomes smaller ~~(Zheng et al., 2017)~~(Zheng et al., 2017), because of the influences of NO_x-emitting factories, power plants, and mobile sources. By comparison,

the ~~correlation~~correlations between ~~the~~ MEIC ~~inventory~~ and these proxies on the ~~0.25° × 0.25°~~0.25°×0.25° grid ~~is~~are 0.~~83~~80 for nighttime light and 0.~~71~~81 for population density~~, higher than~~. The respective correlation values for DECSO are 0.66 and 0.46. The lower correlation values for our ~~emission dataset. This difference is in part because our dataset~~ dataset and DESCO than for MEIC partly reflect that top-down emissions better ~~accounts~~account for the influences of land ~~mobile and offshore shipping sources~~transportation, which are spatially not tied closely to nighttime light and population at this resolution.

Figure 8 compares city-level emissions between our and other inventories. A total of 18 cities within the domain are selected, and for each city the NO_x emissions are summed over the grid cells within the municipal administrative boundaries. All inventories are gridded at 0.05°×0.05° for this purpose. The MarcoPolo inventory does not include emissions for several cities, thus the respective color bars are missing from Fig. 8. Among the cities, emission values differ from -5.8% to +67.5% between our emissions and the mean values of all four inventories (ours, DECSO, MEIC and MarcoPolo (if available)). For most cities, our emissions are consistent with at least one of the other three inventories, often the DESCO top-down inventory, after accounting for errors in our emission estimate. In Yancheng, Huai'an and Ningbo, our emission values are higher than the averages of ours, DECSO and MEIC by 67.5%, 57.5% and 34.6%, respectively. Ningbo (around 29.8°N, 121.5°E) is a coastal city with many isles and marine ports, as identifiable on the nighttime light map (Fig. 6c). The marine ports in the Ningbo-Zhoushan area contribute about 10% of the total shipping emissions in China (Endresen et al., 2003;Fu et al., 2017). Our dataset and DECSO account for emissions from marine shipping and ports, whereas MEIC does not.

5. OSSE-like test of our top-down emission derivation method by using GEOS-Chem simulated NO_2 data

This section further presents an OSSE-like test to estimate the reliability of our emission derivation method, by examining to what extent the method can re-produce the emissions used in a nested GEOS-Chem simulation. Specifically, we use the nested GEOS-Chem v9-02 (Yan et al., 2016;Liu et al.,

2018b;Ni et al., 2018) to simulate the NO_2 VCDs in the early afternoon (around the overpass time of OMI) in summer 2014 on the 0.3125° longitude ×0.25° latitude grid. The simulated NO_2 data are shown in Fig. 9a and the emission inputs are shown in Fig. 9b. Next, we convert the GEOS-Chem NO_2 VCDs into the 0.05°×0.05° grid, and parameterize PHLET with the wind field adopted by GEOS-Chem, following the procedures in Sect. 2.3. Then we use PHLET, PHLET-A, and the lifetime-emission separation method to estimate the NO_x emissions. Finally, we compare the derived emissions (re-mapped to the 0.3125°×0.25° grid) to those used in GEOS-Chem.

Figure 9c and 9d shows the horizontal distributions of our "anthropogenic" emissions and emission errors, respectively. The contribution of soil and biomass burning emissions (as simulated by GEOS-Chem) are subtracted from the dataset. Figure 9e shows the differences between the derived anthropogenic emissions and those used in GEOS-Chem. The emission difference at each grid cell varies from −3.0 to 5. 4 kg km^{-2} h^{-1}, which is attributed to the limitation of our inversion method. The domain average difference is 0.28 kg km^{-2} h^{-1}, or 18% of GEOS-Chem emissions. The scatter plot in Fig. 9f suggests excellent consistency between the derived and the GEOS-Chem emissions, with a linear regression slope of 1.06 and correlation of 0.94. The emission differences for most grid cells are within the uncertainties of the derived emissions (shaded area).

~~5.~~6. Concluding remarks

This study presents a satellite-based ~~NO_x emission inversion~~top-down method ~~for~~to estimating NO_x emissions over urban and surrounding areas at ~~very~~a high horizontal resolution. As a demonstration, the method is applied to the YRD area at the ~~0.05° × 0.05°~~0.05°×0.05° resolution in summer 2012–~~2016~~2015, based on the POMINO NO_2 product. We construct a simplified, computationally efficient 2-D lifetime-emission-transport model (PHLET) and its adjoint model (PHLET-A) to, together with other procedures, facilitate the emission ~~inversion~~estimate. The reliability of our inversion method is supported by 1) a rigorous step-by-step derivation of models, assumptions, and parameters used, 2) a comprehensive uncertainty analysis, and 3) an OSSE-like test with GEOS-Chem simulated NO_2 data. Our ~~inverted~~

emission dataset in the YRD area on the ~~0.05° × 0.05°~~ 0.05°×0.05° grid shows fine-scale spatial information that is tied to nighttime light, population density, road network, ~~and~~ maritime shipping, and land use indicated from a Google Earth photo. Our dataset reveals many fine-scale spatial characteristics not well represented or not included in ~~the widely used MEIC inventory.~~ lower-resolution inventories such as MEIC and DECSO. Although this study derives the averaged emissions over summer 2012–2015, calculations of emissions at higher temporal resolutions (e.g., every 2 years) is possible to better capture the interannual variability and trends.

Our ~~emission~~ inversion method is useful for understanding how human activities have altered the atmospheric environment at fine resolutions. Many crucial human activities, such as urbanization, are conducted at very fine spatial scales. How the resulting emissions affect air quality, public health, and geo-health are still poorly understood due to lack of high-resolution emission data. This problem is particularly severe in the developing countries, because of their rapid paces of urbanization and great inadequacies in emission-related information such as economic statistics and emission factors. This poses a grand challenge for emission control and environmental management. Thus, our inversion method and resulting emission data offer useful independent high-resolution information to monitor the fine-scale emission sources, to improve the bottom-up inventory, to model the urban pollution chemistry and the effect of urbanization, and to conduct spatially targeted emission control.

Our inversion method also has a few shortcomings. The derived emissions do not separate the individual contributions of anthropogenic sectors (i.e., power plants, industry, transportation, and residential). The spatial resolution of the estimated emissions is limited by that of satellite VCD data, although a special oversampling technique has been used to help achieve the highest spatial resolution possible for emissions. The PHLET model is assumed to be 2-dimensional by simplifying the vertical distribution of NO_2 and not accounting for the spatial variability in the vertical shape, similar to previous studies. The adjoint model assumes the observational error covariance matrix to be diagonal, without fully considering the effect of correlations between individual grid cells. Also, we assume a spatially uniform relationship

between NO_2 VCDs and NO_2 lifetimes, which may lead to an underestimate in the lifetimes at low-NO_2 locations over the eastern sea.

Our emission inversion method and models have a few important features enabling their global applications. PHLET and PHLET-A are written in the Python language, which can be readily used with low financial costs. The PHLET model offers computationally efficient simulations of the NO_x chemistry, deposition, and transport. At a low computational cost, our inversion method is able to account for the nonlinear relationship between NO_x concentration, chemical loss, deposition, and transport. With the advent of TROPOMI and other satellite sensors with unprecedented spatial resolutions, our inversion approach can be applied to these measurements for continuous inference of emissions at finer and finer resolutions. ~~As a final point, PHLET and PHLET-A are written in the Python language, which can be readily used with low financial costs.~~

Data availability

Observational data are obtained from individual sources (see links in the text and acknowledgments). Model results are available upon request. Model codes are available on a collaborative basis.

Author contributions

JL conceived the research. HK, RZ and JL designed the research. HK and RZ performed the data processing, model development, and simulations. ML, HW, LC, RN, JW and ~~JW~~YY contributed to data processing, model simulations, and data analyses. QZ provided MEIC data. HK and JL analyzed the results and wrote the paper with input from all authors.

Competing interests

The authors declare that they have no conflict of interest.

Acknowledgements

This research is supported by the National Natural Science Foundation of China (41775115) and the 973 program (2014CB441303).

Appendix A. Solving the diffusion process

The diffusion term can be simplified as follows:

$$\nabla \cdot \left(\mathbf{K}(x,y) \cdot \nabla C(x,y)\right) = \frac{\partial}{\partial x}\left(K_x \cdot \frac{\partial C}{\partial x}\right) + \frac{\partial}{\partial y}\left(K_y \cdot \frac{\partial C}{\partial y}\right) \quad \text{(A1)}$$

K_x and K_y are the diffusion coefficients in the zonal and meridional directions, respectively. ~~Given these coefficients, we solve the equation with the algorithm described in (Brasseur and Jacob, 2017).~~

We derive the diffusion coefficients based on a random walk assumption ~~(Schirmacher, 2015)~~(Schirmacher, 2015):

$$K_{x\ or\ y} = \frac{1}{2}\overline{V_{x\ or\ y}'}^2\ t_0, \quad \text{(A4)}$$

$\overline{V_{x\ or\ y}'}$ is the deviation of wind speed in the zonal or meridional direction. t_0 is 3 hours, the sampling interval of ERA5 wind data. Figure ~~A1~~A shows the time averaged wind vector and the distribution of K_x and K_y. The relative uncertainty in wind speed is assumed to be 10%, close to the temporal standard deviation of wind speed. The uncertainties of K_x and K_y are set to be 20%, about twice of the relative uncertainty in wind speed. The calculated K_x ranges from 30397 m^2s^{-2} over land to 203783 m^2s^{-2} over sea. The K_y ranges from 25811 m^2s^{-2} over land to 297053 m^2s^{-2} over sea. These diffusion coefficients tend to be slightly underestimated, because the variabilities of wind speed at higher frequencies (than 3-hourly) are not accounted for. This means that PHLET may underestimate the horizontal transport slightly.

Appendix B. Satellite Conversion Matrix to account for the smoothing effect of satellite pixels

The SCM is essentially a tool to preform quick conversion between grids, regular or not. In the YRD area, there are $100 \times 100 = 10000$ grid cells on the ~~0.05° × 0.05°~~0.05°×0.05° grid. We use the SCM (**A** matrix: [10000, 10000]) to convert from its original grid (***X*** vector: [10000, 1]) to the final grid (***Y*** vector: [10000, 1]), i.e., $\boldsymbol{Y} = \mathbf{A}\boldsymbol{X}$. The 10000 elements in one specific row of **A** represent the weights of the 10000 elements of ***X*** to an element in ***Y***. Apparently, **A** is a sparse matrix. The following description shows how **A** is constructed.

First, the VCDs specific to satellite pixels are reconstructed from the model grid cells. Each model grid cell (MGC) is divided into $10 \times 10 = 100$ finer grid cells (FGCs), each having the same area. Suppose the number of MGCs fully or partially covered by a given pixel p is N_c, and the number of FGCs in a given MGC i covered by p is g_i^p, then the total number of FGCs covered by p is:

$$G^p = \sum_{i=1}^{N_c} g_i^p \tag{B1}$$

Thus, the average VCD for the pixel p can be reconstructed as follows:

$$VCD^p = \sum_{i=1}^{N_c} \frac{g_i^p}{G^p} \cdot VCD_i \tag{B2}$$

Equation (B2) essentially means how a satellite pixel smooths the VCD. The blue portion of Fig. ~~B1~~B denotes the projection from MGC i to pixel p.

The next step represents how the oversampling approach is applied to satellite-smoothed VCD data. Suppose the number of satellite pixels fully or partially covering ~~a~~an MGC j is Np, then the total number of FGCs being part of the intersection of the Np pixels and MGC j is:

$$G_j = \sum_{p=1}^{N_p} g_j^p \tag{B3}$$

Finally, the average VCD for the MGC j converted from the Np pixels is:

$$\mathrm{VCD'_j} = \sum_{p=1}^{N_p} \frac{g_j^p}{G_j} \cdot \mathrm{VCD^p} \quad \text{(B4)}$$

The pink portion of Fig. ~~B1~~B denotes the projection from pixel p to MGC j. Thus, the element of SCM converting from MGC i to MGC j can be derived as follows:

$$A_{j,i} = \sum_{p=1}^{N_p} \frac{g_j^p}{G_j} \cdot \frac{g_i^p}{G^p} \quad \text{(B5)}$$

Appendix C. ~~Solving the observation error covariance matrix and the adjoint model~~

~~The observation error covariance matrix ($\mathbf{S_o}$) consists of a satellite data error covariance matrix ($\mathbf{S_s}$) and a PHLET model error covariance matrix ($\mathbf{S_m}$):~~

~~$$\mathbf{S_o} = \mathbf{S_s} + \mathbf{S_m} \quad \text{(C1)}$$~~

~~Both $\mathbf{S_s}$ and $\mathbf{S_m}$ are assumed to be diagonal, with the diagonal elements set to be σ_s^2 and σ_m^2, respectively.~~

~~As shown in Eq. (7), PHLET-A represents the sensitivity of cost function (J) to local net source ($\boldsymbol{L}$) (Marchuk, 1994;Sandu et al., 2005). Given a starting point of $\boldsymbol{L}$, we can derive a search direction by the Cautious Broyden-Fletcher-Goldfarb-Shanno (CBFGS) method (Li and Fukushima, 2001;Bousserez et al., 2015). Then, by practicing backtracking line search based on the Armijo–Goldstein condition (Armijo, 1966), we can evaluate an optimized $\boldsymbol{L}$. The uncertainty of $\boldsymbol{L}$ is given by the Hessian of the cost function, which is approximated by the CBFGS method (Brasseur and Jacob, 2017):~~

~~$$\boldsymbol{S} = 2 \cdot (\nabla_{\boldsymbol{L}}^2 J)^{-1} \quad \text{(C2)}$$~~

~~Appendix D.~~ Deriving NO_2 lifetime from VCD

We assume a steady state of radicals (HO_x), where the production rate of HO_x is equal to the loss rate through three types of termination reactions: between the hydroxyl radical (OH) and NO_2, between NO

and peroxyl radicals to form organic nitrates, and between peroxyl radicals (Murphy et al., 2006;Valin et al., 2011):

$$P(HO_x) = k_1 C_{OH} C_{NO_2} + \alpha k_{2eff} \frac{k_1 C_{NMVOC} C_{OH}}{k_{2eff} C_{NO}} C_{NO} + 6 k_{3eff} \left(\frac{k_1 C_{NMVOC} C_{OH}}{k_{2eff} C_{NO}}\right)^2 \quad (\text{~~D1~~C1})$$

Here $P(HO_x)$ is the production rate, and the right-~~-~~hand side of Eq. (~~D1~~C1) is the loss rate. C_{NO_2} and C_{OH} denote the concentrations of NO_2 and OH, respectively. Since the conversion between the peroxyl radicals (HO_2 + RO_2) and OH is in steady state, the term $\frac{k_1 C_{NMVOC} C_{OH}}{k_{2eff} C_{NO}}$ expresses the "effective" total concentration of peroxyl radicals in terms of the concentrations of NMVOC, OH and NO. Assuming $P(HO_x)$, C_{NMVOC} and all reaction constants to be constant ~~(Valin et al., 2011)~~(Valin et al., 2011), and given that $C_{NO} = C_{NO_2} \cdot \frac{1-r}{r}$, Eq. (~~D1~~C1) can be simplified as Eq. (~~D2~~C2):

$$a C_{OH} C_{NO_2} + b C_{OH} + c \left(\frac{C_{OH}}{C_{NO_2}}\right)^2 = 1 \quad (\text{~~D2~~C2})$$

Here a, b, c are the coefficients. Because the chemical ~~lifetime~~lifetimes of NO_2 is determined by C_{OH} ($\tau_c = \frac{1}{k_1 C_{OH}}$) , we can deduce the relationship between C_{NO_2} and τ_c:

$$\frac{a'}{\tau_c} + \frac{b'}{\tau_c \cdot C_{NO_2}} + c' \left(\frac{1}{\tau_c \cdot C_{NO_2}}\right)^2 = -1 \quad (\text{~~D3~~C3})$$

NO_2 is lost primarily through reaction with OH and secondarily through dry deposit ($\frac{C_{NO_2}}{\tau_d}$), thus its lifetime (τ) is also determined by these two loss processes. Therefore,

$$\tau_c = \frac{1}{\frac{1}{\tau} - \frac{1}{\tau_d}} \quad (\text{~~D4~~C4})$$

In the areas of low emissions, the emission term can be neglected in Eq. 2, thus the local net source $L = -\frac{C_{NO_2}}{r \cdot \tau}$. Therefore Eq. ~~D3~~C3 becomes Eq. ~~D5~~C5, which connects L and C_{NO_2}.

$$a' \frac{r(L+kC_{NO_2})}{C_{NO_2}} + b' \frac{r(L+kC_{NO_2})}{C_{NO_2}^2} + c' \left(\frac{r(L+kC_{NO_2})}{C_{NO_2}^3}\right)^2 = 1 \quad (\text{~~D5~~C5})$$

where $k = \frac{1}{\tau_d}$. We determine the coefficients a', b', c', and k in Eq. ~~D5~~C5 by conducing nonlinear fitting of OMI NO_2 VCD data and L values in the low emission areas (see below). This procedure establishes the nonlinear relationship between τ and VCD, which is then applied to the entire study domain.

The low-emission areas have small values of VCD and large negative values of L. Figure ~~D1a~~C shows a scatter plot for the ~~inverted~~derived local net source L and VCD at each individual grid cell of the study domain. The data scatter reflects the combined effect of emission, loss, and horizontal transport. We then fit the quantiles of L where the VCD is relatively low ($< 5 \times 10^{15}$ molecules cm^{-2}~~) into Eq. 6 through a nonlinear quantile fitter based on Tensor flow.~~, shown as blue points in Fig. C) into Eq. C5 through a nonlinear quantile fitter based on Tensorflow(Abadi et al., 2016). Using the quantile fitting also means that the low-emission grid cells do not need to be explicitly identified prior to the fitting. The quantile fitting gives L as a function of VCD (when emissions are neglected), through which the relationship between ~~lifetime~~lifetimes and ~~VCD~~VCDs is derived. We conduct the fitting by ~~500~~50 times, each by linearly changing the assumed percentile threshold of L from 0.~~01~~1% to ~~10~~5%, to determine the fitted median value (red line in Fig. ~~D1a~~C) and uncertainty (gray shaded areas, 95% CI). The uncertainty is caused by the assumption on the NO_2/NO_x ratio r, the simplification of the relationship between ~~lifetime~~lifetimes and ~~VCD~~VCDs, and possible misjudgment of low-emission areas.

The orange line in Fig. ~~D1b~~C presents the relationship between NO_2 ~~VCD~~VCDs and chemical ~~lifetime~~lifetimes (τ_c) derived based on the mean value of the fitting. The value of τ_c varies from ~~1.7 to~~ 0.6~~.6~~ ~~to~~ 3.8 h with an average of 1.2~~.8~~ h. The ~~lifetime declines~~lifetimes decline rapidly with increasing ~~VCD~~VCDs from 0 to 2×10^{15} molecules cm^{-2}, and then grows gradually with increasing ~~VCD~~VCDs. This result is consistent with Valin et al. (2011). By comparison, the value of τ_d is ~~7.8~~30.4 h and is spatially homogeneous under the assumption here. The total lifetime (τ) varies from ~~1.4~~0.6 to 3.~~6~~3 h (Fig. ~~D1b~~C, blue line) across the study domain.

Appendix E. Testing our emission inversion method using GEOS-Chem simulated NO_2 data

We apply our emission inversion method to the NO_2 VCD data simulated by the nested GEOS-Chem CTM. Specifically, we use GEOS-Chem v9-02 (Liu et al., 2018a;Ni et al., 2018;Yan et al., 2016) to simulate the NO_2 VCDs in the early afternoon (around the overpass time of OMI) in summer 2014 on the $0.3125° \times 0.25°$ grid. The simulated NO_2 data are shown in Fig. E1a. Next, we convert the GEOS-Chem NO_2 VCDs into the $0.05° \times 0.05°$ grid, and parameterize PHLET with the wind field adopted by GEOS-Chem, following the procedures in Sect. 2.3. Then we use PHLET, PHLET-A, and the lifetime-emission separation method to estimate the NO_x emissions. Finally, we compare the inverted emissions (re-mapped to the $0.25° \times 0.3125°$ grid) to those used in GEOS-Chem.

Figure E1c and E1d shows the horizontal distributions of our inverted "anthropogenic" emissions and emission uncertainties, respectively. The contribution of soil emissions (as simulated by GEOS-Chem) is subtracted from the inverted dataset. Figure E1e shows the differences between the inverted anthropogenic emissions and the GEOS-Chem anthropogenic emissions. The emission difference at each grid cell varies from −4.5 to 5.8 kg km^{-2} h^{-1}, which is attributed to the limitation of our inversion method. The domain average difference is 0.25 kg km^{-2} h^{-1}, or 16% (with respect to GEOS-Chem emission value). The scatter plot in Fig. E1f suggests excellent consistency between the inverted and the GEOS-Chem emissions, with a linear regression slope of 0.98 and correlation of 0.93. The inverted emissions tend to be overestimated in the low-emission areas, but the differences are within the uncertainties of the inverted emissions (shaded area).

References

NBSC (National Bureau of Statistics of China) STATISTICAL COMMUNIQUÉ OF THE PEOPLE'S REPUBLIC OF CHINA ON THE 2017 NATIONAL ECONOMIC AND SOCIAL DEVELOPMENT,

NBSC (National Bureau of Statistics of China) STATISTICAL COMMUNIQUÉ OF THE PEOPLE'S REPUBLIC OF CHINA ON THE 2013 NATIONAL ECONOMIC AND SOCIAL DEVELOPMENT,

NBSC (National Bureau of Statistics of China) STATISTICAL COMMUNIQUÉ OF THE PEOPLE'S REPUBLIC OF CHINA ON THE 2009 NATIONAL ECONOMIC AND SOCIAL DEVELOPMENT,

NBSC (National Bureau of Statistics of China) China Statistical Yearbook 2007 2008 2009 2010 2011 2012 2013 2014 2015 2016 2017,

~~Armijo~~Abadi, M., Agarwal, A., Barham, P., Brevdo, E., Chen, Z., Citro, C., Corrado, G. s., Davis, A., Dean, J., Devin, M., Ghemawat, S., Goodfellow, I., Harp, A., Irving, G., Isard, M., Jia, Y., Jozefowicz, R., Kaiser, L~~. J. P.~~., Kudlur, M., and Zheng, X.: TensorFlow: Large-Scale Machine Learning on Heterogeneous Distributed Systems, 2016.

Alnaes, M. S., Blechta, J~~. o. M.: .~~, Hake, J., Johansson, A., Kehlet, B., Logg, A., Richardson, C., Ring, J., Rognes, M. E., and Wells, G. N.: The FEniCS Project Version 1.5, Archive of Numerical Software, 3, 9-23, 2015.

Armijo, L.: Minimization of functions having Lipschitz continuous first partial derivatives~~. Pac. J. Math.~~, Pacific Journal of Mathematics, 16, 1-3, 10.2140/pjm.1966.16.1, 1966.

Barnes, I., and Rudziński, K. J.: Disposal of Dangerous Chemicals in Urban Areas and Mega Cities, Springer Netherlands, 2013.

Beirle, S., Boersma, K. F., Platt, U., Lawrence, M. G., and Wagner, T.: Megacity Emissions and Lifetimes of Nitrogen Oxides Probed from Space, Science, 333, 1737-1739, ~~doi:~~10.1126/science.1207824, 2011.

Beirle, S., Sihler, H., and Wagner, T.: Mapping NO_x Sources on High Spatial Resolution by Combined Measurements from OMI and GOME-2 Narrow Swath Mode, ~~Atmos, 2015,~~ATMOS 2015, Proceedings of the Conference held 8-12 June, Crete, 2015,

Boersma, K., Vinken, G., and Tournadre, J.: Ships going slow in reducing their NO_x emissions: Changes in 2005-2012 ship exhaust inferred from satellite measurements over Europe, ~~2015.~~Environmental Research Letters, 10, 10.1088/1748-9326/10/7/074007, 2015.

Boersma, K. F., Eskes, H. J., Dirksen, R. J., and R., J. v. d. A~~. J. A. M. T.~~: An improved tropospheric NO_2 column retrieval algorithm for the Ozone Monitoring Instrument, Atmospheric Measurement Techniques 4, 2329-2388, 2011.

Bousserez, N., Henze, D. K., Perkins, A., Bowman, K. W., Lee, M., Liu, J., Deng, F., and Jones, D. B. A.: Improved analysis-error covariance matrix for high-dimensional variational inversions: application to source estimation using a 3D atmospheric transport model, Quarterly Journal of the Royal Meteorological Society, 141, 1906-1921, ~~doi:~~10.1002/qj.2495, 2015.

Brasseur, G. P., and Jacob, D. J.: Modeling of atmospheric chemistry, 2017.

Cao, H., Fu, T.-M., Zhang, L., Henze, D. K., Miller, C. C., Lerot, C., Abad, G. G., De Smedt, I., Zhang, Q., van Roozendael, M., Hendrick, F., Chance, K., Li, J., Zheng, J., and Zhao, Y.: Adjoint inversion of Chinese non-methane volatile organic compound emissions using space-based observations of formaldehyde and glyoxal, Atmospheric Chemistry and Physics, 18, 15017-15046, 10.5194/acp-18-15017-2018, 2018.

Cui, Y~~. Z.~~, Lin, J~~. T.~~, Song, C., Liu, M~~. Y.~~, Yan, Y~~. Y.~~, Xu, Y., and Huang, B~~. J. A. C., and Physics:.~~: Rapid growth in nitrogen dioxide pollution over Western China, 2005~~–~~2013, ~~15, 34913-34948,~~ Atmospheric Chemistry and Physics, 16, 6207-6221, 10.5194/acp-16-6207-2016, 2016.

de Graaf, M., Sihler, H., Tilstra, L. G., and Stammes, P.: How big is an OMI pixel?~~, Atmos. Meas. Tech.,~~, Atmospheric Measurement Techniques, 9, 3607-3618, ~~doi:~~10.5194/amt-9-3607-2016, 2016.

De Smedt, I., Stavrakou, T., Hendrick, F., Danckaert, T., Vlemmix, T., Pinardi, G., Theys, N., Lerot, C., Gielen, C., Vigouroux, C., Hermans, C., Fayt, C., Veefkind, P., Müller, J. F., and Van Roozendael, M.: Diurnal, seasonal and long-term variations of global formaldehyde columns inferred from combined OMI and GOME-2 observations, Atmospheric Chemistry and Physics, 15, 12519-12545, 10.5194/acp-15-12519-2015, 2015.

Ding, J., Johannes, V. D. A., Ronald, Mijling, B., and Felicitas Levelt, P~~. J. A. M. T.~~: Space-based NO_x emission estimates over remote regions improved in DECSO, ~~10, 1-21~~Atmospheric Measurement Techniques, 10, 925-938, 10.5194/amt-10-925-2017, 2017a.

Ding, J., Miyazaki, K., ~~Johannes, V. D. A., Ronald,~~van der A, R. J., Mijling, B., Kurokawa, J.-i., Cho, S~~. Y., Janssensmaenhout~~., Janssens-Maenhout, G., Zhang, Q., Liu, F., ~~Felicitas~~and Levelt, P. ~~J. A. C., and Physics:~~F.: Intercomparison of NO_x emission inventories over East Asia, ~~17, 1-35~~Atmospheric Chemistry and Physics, 17, 10125-10141, 10.5194/acp-17-10125-2017, 2017b.

Elvidge, C., Hsu, F. C., Baugh, K. E., and Ghosh, T.: National Trends in Satellite Observed Lighting: 1992-2012, in: lobal Urban Monitoring and Assessment Through Earth Observation (In Press), CRC Press, 2013.

Endresen, Ø., Sørgård, E., Sundet, J. K., Dalsøren, S. B., Isaksen, I. S. A., Berglen, T. F., and Gravir, G~~. J. J. o. G. R. A.~~.: Emission from international sea transportation and environmental impact, Journal of Geophysical Research, 108, -, 10.1029/2002jd002898, 2003.

Eskes, H. J., Velthoven, P. F. J. V., Valks, P. J. M., and Kelder, H. M.: Assimilation of GOME total-ozone satellite observations in a three-dimensional tracer-transport model, Quarterly Journal of the Royal Meteorological Society, 129, 1663-1681, ~~doi:~~10.1256/qj.02.14, 2003.

Farrell, P. E., Ham, D. A., Funke, S. F., and Rognes, M. E.: Automated derivation of the adjoint of high-level transient finite element programs, Computer Science, 35, 10.1137/120873558, 2012.

Fioletov, V. E., McLinden, C. A., Krotkov, N., Moran, M. D., and Yang, K.: Estimation of SO_2 emissions using OMI retrievals, Geophysical Research Letters, 38, n/a-n/a, ~~doi:~~10.1029/2011gl049402, 2011.

Fu, M., Liu, H., Jin, X., and He, K.: National- to port-level inventories of shipping emissions in China, Environmental Research Letters, 12, ~~doi:~~10.1088/1748-9326/aa897a, 2017.

Fu, Q., Shen, Y., and Zhang, J.: On the ship pollutant emission inventory in Shanghai port, J. Saf. Environ., 12, 57–64, 2012.

Funke, S. W., and Farrell, P. E.: A framework for automated PDE-constrained optimisation, Computer Science, 2013.

Geng, G., Zhang, Q., Martin, R. V., Lin, J., Huo, H., Zheng, B., Wang, S., and He, K.: Impact of spatial proxies on the representation of bottom-up emission inventories: A satellite-based analysis, Atmospheric Chemistry and Physics, 17, 4131-4145, ~~doi:~~10.5194/acp-17-4131-2017, 2017.

Giglio, L., Randerson, J. T., van der Werf, G. R., Kasibhatla, P. S., Collatz, G. J., Morton, D. C., and DeFries, R. S.: Assessing variability and long-term trends in burned area by merging multiple satellite fire products, Biogeosciences Discussions, 6, 11577-11622, 10.5194/bgd-6-11577-2009, 2009.

Giglio, L., T. Randerson, J., and R. van der Werf, G.: Analysis of daily, monthly, and annual burned area using the Fourth-Generation Global Fire Emissions Database (GFED4), Journal of Geophysical Research: Biogeosciences, 118(1), 10.1002/jgrg.20042, 2013.

Granier, C., Darras, S., Gon, H. D. v. d., Doubalova, J., Elguindi, N., Galle, B., Gauss, M., Guevara, M., Jalkanen, J.-P., Kuenen, J., Liousse, C., Quack, B., Simpson, D., and Sindelarova, K.: The Copernicus Atmosphere Monitoring Service global and regional emissions (April 2019 version), Copernicus Atmosphere Monitoring Service (CAMS) report, doi:10.24380/d0bn-kx16, 2019.

Gu, D., Wang, Y., Smeltzer, C., and Boersma, K. F.: Anthropogenic emissions of NO_x over China: Reconciling the difference of inverse modeling results using GOME-2 and OMI measurements, Journal of Geophysical Research: Atmospheres, 119, 7732-7740, ~~doi:~~10.1002/2014jd021644, 2014.

Gu, D., Wang, Y., Yin, R., Zhang, Y., and Smeltzer, C.: Inverse modelling of NO_x emissions over eastern China: uncertainties due to chemical non-linearity, Atmospheric Measurement Techniques, 9, 5193-5201, 10.5194/amt-9-5193-2016, 2016.

Hakami, A., Henze, D. K., Seinfeld, J. H., Singh, K., Sandu, A., Kim, S., Byun, D., and Li, Q.: The Adjoint of CMAQ, Environ. Sci. Technol, 41, 7807-7817, 2007.

Hersbach, H., and Dee, D.: ERA5 reanalysis is in production, ECMWF Newsletter No. 147, 7, 2016.

~~Huang, M., Bowman, K. W., Carmichael, G. R., Chai, T., Pierce, R. B., Worden, J. R., Luo, M., Pollack, I. B., Ryerson, T. B., and Nowak, J. B. J. J. o. G. R.: Changes in Nitrogen Oxides Emissions in California during 2005-2010 Indicated from Top-down and Bottom-up Emission Estimates, 119, 12,928-912,952, 2014.~~

Hooyberghs, H., Veldeman, N., and Maiheu, B.: MarcoPolo Emission Inventory for EastChina: Basic Description, 2016.

J. Yienger, J., and Ii Levy, H.: Empirical model of global soil-biogenic NO_x emissions, 11447-11464 pp., 1995.

Janssens-Maenhout, G., Crippa, M., Guizzardi, D., Dentener, F., Muntean, M., Pouliot, G., Keating, T., Zhang, Q., Kurokawa, J., and Wankmüller, R.: HTAP_v2.2: a mosaic of regional and global emission gridmaps for 2008 and 2010 to study hemispheric transport of air pollution, Atmospheric Chemistry ~~&~~and Physics, 15, 12867-12909, 2015.

Keiya, Y., and Itsushi, U.: Adjoint inverse modeling of CO emissions over Eastern Asia using four-dimensional variational data assimilation, Atmospheric Environment, 40, 6836-6845, 2006.

Krotkov, N. A., McLinden, C. A., Li, C., Lamsal, L. N., Celarier, E. A., Marchenko, S. V., Swartz, W. H., Bucsela, E. J., Joiner, J., Duncan, B. N., Boersma, K. F., Veefkind, J. P., Levelt, P. F., Fioletov, V. E., Dickerson, R. R., He, H., Lu, Z., and Streets, D. G.: Aura OMI observations of regional SO_2 and NO_2 pollution changes from 2005 to 2015, Atmospheric Chemistry and Physics, 16, 4605-4629, ~~doi:~~10.5194/acp-16-4605-2016, 2016.

Lamsal, L. N., Martin, R. V., Padmanabhan, A., van Donkelaar, A., Zhang, Q., Sioris, C. E., Chance, K., Kurosu, T. P., and Newchurch, M. J.: Application of satellite observations for timely updates to global anthropogenic ~~NO(x)~~NO_x emission inventories, Geophysical Research Letters, 38, L05810, ~~doi:~~10.1029/2010gl046476, 2011.

Levelt, P. F., van den Oord, G. H. J., Dobber, M. R., Malkki, A., Huib, V., Johan de, V., Stammes, P., Lundell, J. O. V., and Saari, H.: The ozone monitoring instrument, IEEE Transactions on Geoscience and Remote Sensing, 44, 1093-1101, 10.1109/tgrs.2006.872333, 2006.

Li, D.-H., and Fukushima, M.: A modified BFGS method and its global convergence in nonconvex minimization, Journal of Computational and Applied Mathematics, 129, 15-35, 2001.

Lin, J.-T., Liu, M.-Y., Xin, J. Y., Boersma, K. F., Spurr, R., Martin, R., and Zhang, Q.: Influence of aerosols and surface reflectance on satellite NO_2 retrieval: seasonal and spatial characteristics and implications for NO_x emission constraints, Atmospheric Chemistry and Physics, 15, 11217-11241, ~~doi:~~10.5194/acp-15-11217-2015, ~~2015~~2015a.

Lin, J., Tong, D., Davis, S., Ni, R., Tan, X., Pan, D., Zhao, H., Lu, Z., Streets, D., Feng, T., Zhang, Q., Yan, Y., Hu, Y., Li, J., Liu, Z., Jiang, X., Geng, G., He, K., Huang, Y., and Guan, D.: Global climate forcing of aerosols embodied in international trade, Nature Geoscience, 9, 790-794, ~~doi:~~10.1038/ngeo2798, 2016.

Lin, J. T., McElroy, M. B., and Boersma, K. F.: Constraint of anthropogenic NO_x emissions in China from different sectors: a new methodology using multiple satellite retrievals, Atmos. Chem. Phys., 10, 63-78, ~~doi:~~10.5194/acp-10-63-2010, 2010.

Lin, J. T.: Satellite constraint for emissions of nitrogen oxides from anthropogenic, lightning and soil sources over East China on a high-resolution grid, ~~Atmos. Chem. Phys.,~~Atmospheric Chemistry and Physics, 12, 2881-2898, ~~doi:~~10.5194/acp-12-2881-2012, 2012.

~~Lin, J. T., Liu, Z., Zhang, Q., Liu, H., Mao, J., and Zhuang, G.: Modeling uncertainties for tropospheric nitrogen dioxide columns affecting satellite-based inverse modeling of nitrogen oxides emissions, Atmos. Chem. Phys., 12, 12255-12275, doi:10.5194/acp-12-12255-2012, 2012.~~

Lin, J. T., Martin, R. V., Boersma, K. F., Sneep, M., Stammes, P., Spurr, R., Wang, P., Van Roozendael, M. V., Clémer, K., and Irie, H. J. A. C., and Physics, 3:.: Retrieving tropospheric nitrogen dioxide from the Ozone Monitoring Instrument: Effects of aerosols, surface reflectance anisotropy, and vertical profile of nitrogen dioxide, Atmospheric Chemistry and Physics, 14, 1441-1461, 10.5194/acp-14-1441-2014, 2014.

Lin, J. T., Liu, M. Y., Xin, J. Y., Boersma, K. F., Spurr, R., Martin, R., and Zhang, Q.: Influence of aerosols and surface reflectance on satellite NO_2 retrieval: seasonal and spatial characteristics and implications for NO_x emission constraints, Atmospheric Chemistry and Physics, 15, 11217-11241, 10.5194/acp-15-11217-2015, 2015b.

Liu, F., Zhang, Q., Tong, D., Zheng, B., Li, M., Huo, H., and He, K. B.: High-resolution inventory of technologies, activities, and emissions of coal-fired power plants in China from 1990 to 2010, Atmospheric Chemistry and Physics, 15, 13299-13317, 10.5194/acp-15-13299-2015, 2015.

Liu, F., Beirle, S., Zhang, Q., Dörner, S., He, K., and Wagner, T.: NO_x lifetimes and emissions of cities and power plants in polluted background estimated by satellite observations, Atmospheric Chemistry and Physics, 16, 5283-5298, doi:10.5194/acp-16-5283-2016, 2016.

Liu, F., Beirle, S., Zhang, Q., van der, A. R., Zheng, B., Tong, D., and He, K.: NO_x emission trends over Chinese cities estimated from OMI observations during 2005 to 2015, Atmospheric Chemistry and Physics, 17, 9261-9275, 10.5194/acp-17-9261-2017, 2017.

Liu, M.-Y., Lin, J.-T., Boersma, K. F., Pinardi, G., Wang, Y., Chimot, J., Wagner, T., Xie, P., Eskes, H., Van Roozendael, M., Hendrick, F., Wang, P., and Yan, Y.-Y.: Improved aerosol correction for OMI tropospheric NO_2 retrieval over East Asia: constraint from CALIOP aerosol vertical profile, Atmospheric Measurement Techniques Discussions, 10.5194/amt-2018-34, 2018a.

Liu, M.-Y., Lin, J.-T., Wang, Y.-C., Sun, Y., Zheng, B., Shao, J., Chen, L.-L., Zheng, Y., Chen, J., Fu, T. M., Yan, Y.-Y., Zhang, Q., and Wu, Z.: Spatiotemporal variability of NO_2 and PM2.5 over Eastern China: observational and model analyses with a novel statistical method, Atmospheric Chemistry and Physics, 18, 12933-12952, doi:10.5194/acp-18-12933-2018, 2018a2018b.

Liu, M., Lin, J., Boersma, K. F., Pinardi, G., Wang, Y., Chimot, J., Wagner, T., Xie, P., Eskes, H., Van Roozendael, M., Hendrick, F., Wang, P., andWang, T., Yan, Y., Chen, L., and Ni, R.: Improved aerosol correction for OMI tropospheric NO₂NO_2 retrieval

over East Asia: constraint from CALIOP aerosol vertical profile, Atmospheric Measurement Techniques Discussions, 12, 1-48, doi:21, 10.5194/amt-2018-34, 2018b12-1-2019, 2019.

Ma, J., and Xiuji, Z.: Development of a three-dimensional inventory of aircraft NO_x emissions over China, Atmospheric Environment, 34, 389-396, 2000.

Maiheu, B., and Veldeman, N.: NO_x Emission Downscaling for South Africa, 2013.

Marchuk, G. L.: Adjoint Equations and Analysis of Complex Systems, Russian Academy of Sciences, Moscow, Russia, 475 pp., 1994.

Martien, P. T., Harley, R. A., and Cacuci, D. G.: Adjoint Sensitivity Analysis for a Three-Dimensional Photochemical Model: Implementation and Method Comparison, Environ. Sci. Technol, 40, 2663-2670, 2006.

Martin, R. V., Jacob, D. J., Chance, K., Kurosu, T. P., Palmer, P. I., and Evans, M. J.: Global inventory of nitrogen oxide emissions constrained by space-based observations of NO_2 columns, Journal of Geophysical Research: Atmospheres, 108, 4537, doi:10.1029/2003JD003453, 2003.

Mijling, B., and R., J. v. d. A. J. J. o. G. R. A.: Using daily satellite observations to estimate emissions of short-lived air pollutants on a mesoscopic scale, J Journal of Geophysical Research Atmospheres, 117, -, 2012.

Mijling, B., van der A, R. J., and Zhang, Q.: Regional nitrogen oxides emission trends in East Asia observed from space, Atmospheric Chemistry and Physics, 13, 12003-12012, 10.5194/acp-13-12003-2013, 2013.

Miyazaki, K., Eskes, H. J., and Sudo, K.: Global NO_x emission estimates derived from an assimilation of OMI tropospheric NO_2 columns, Atmospheric Chemistry and Physics, 12, 2263-2288, doi:10.5194/acp-12-2263-2012, 2012.

Miyazaki, K., Eskes, H., Sudo, K., Boersma, K. F., Bowman, K., and Kanaya, Y.: Decadal changes in global surface NO_x emissions from multi-constituent satellite data assimilation, Atmospheric Chemistry and Physics Discussions, 1-48, doi:10.5194/acp-2016-529, 2016.

Murphy, J. G., Day, D. A., Cleary, P. A., Wooldridge, P. J., Millet, D. B., Goldstein, A. H., and Cohen, R. C.: The weekend effect within and downwind of Sacramento: Part 2. Observational evidence for chemical and dynamical contributions, Atmospheric Chemistry and Physics Discussions, 6, 11971-12019, doi:10.5194/acpd-6-11971-2006, 2006.

Ni, R.-J., Lin, J.-T., Yan, Y.-Y., and Lin, W.: Foreign and domestic contributions to springtime ozone over China, Atmospheric Chemistry and Physics, 18, 11447-11469, doi:10.5194/acp-18-11447-2018, 2018.

Qu, Z., Henze, D. K., Capps, S. L., Wang, Y., Xu, X., Wang, J., and Keller, M. J. J. o. G. R. A.: Monthly top-down NOx emissions for China (2005–2012): A hybrid inversion method and trend analysis, 122, 2017.

Sandu, A., Daescu, D. N., Carmichael, G. R., and Chai, T.: Adjoint sensitivity analysis of regional air quality models, Journal of Computational Physics, 204, 222-252, doi:10.1016/j.jcp.2004.10.011, 2005.

Schere, K. L. J. A. E.: An evaluation of several numerical advection schemes, 17, 1897-1907, 1983.

Schirmacher, W.: Theory of Liquids and Other Disordered Media, Springer International Publishing, 2015.

Seinfeld, J. H., Pandis, S. N. J. A. C., and Physics: From air pollution to climate change, 429-443, 2006.

Stavrakou, T., Muller, J. F., Boersma, K. F., De Smedt, I., and van der A, R. J.: Assessing the distribution and growth rates of NO_x emission sources by inverting a 10-year record of NO_2 satellite columns, Geophysical Research Letters, 35, L10801, doi:10.1029/2008gl033521, 2008.

Stavrakou, T., Müller, J. F., Boersma, K. F., van der A, R. J., Kurokawa, J., Ohara, T., and Zhang, Q.: Key chemical NO_x sink uncertainties and how they influence top-down emissions of nitrogen oxides, Atmos. Chem. Phys., 13, 9057-9082, doi:10.5194/acp-13-9057-2013, 2013.

Sun, K., Zhu, L., Cady-Pereira, K., Chan Miller, C., Chance, K., Clarisse, L., Coheur, P.-F., Gonzalez Abad, G., Huang, G., Liu, X., Van Damme, M., Yang, K., and Zondlo, M.: A physics-based approach to oversample multi-satellite,

multi-species observations to a common grid, Atmospheric Measurement Techniques Discussions, 1-30, doi:10.5194/amt-2018-253, 2018.

Tang, W., Cohan, D. S., Lamsal, L. N., Xiao, X., and Zhou, W.: Inverse modeling of Texas NO_x; emissions using space-based and ground-based NO_2 observations, Atmospheric Chemistry and Physics, 13, 11005-11018, 10.5194/acp-13-11005-2013, 2013.

Timmermans, R., Kranenburg, R., and Hooyberghs, H.: MarcoPolo project, Deliverable 4.3, 2016.

Valin, L. C., Russell, A. R., Hudman, R. C., and Cohen, R. C.: Effects of model resolution on the interpretation of satellite NO_2 observations, Atmospheric Chemistry and Physics, 11, 11647-11655, doi:10.5194/acp-11-11647-2011, 2011.

Valin, L. C., Russell, A. R., and Cohen, R. C.: Variations of OH radical in an urban plume inferred from NO_2 column measurements, Geophysical Research Letters, 40, 1856-1860, doi:10.1002/grl.50267, 2013.

~~Walcek, C. J.: Minor flux adjustment near mixing ratio extremes for simplified yet highly accurate monotonic calculation of tracer advection, Journal of Geophysical Research: Atmospheres, 105, 9335-9348, doi:10.1029/1999jd901142, 2000.~~

Wang, Y., Jacob, D. J., and Logan, J. A.: Global simulation of tropospheric O_3-NO_x-hydrocarbon chemistry: 1. Model formulation, 103, 10713-10725, 10.1029/98jd00158, 1998.

Yan, Y.-Y., Lin, J.-T., Chen, J., and Hu, L.: Improved simulation of tropospheric ozone by a global-multi-regional two-way coupling model system, Atmospheric Chemistry and Physics, 16, 2381-2400, ~~doi:~~10.5194/acp-16-2381-2016, 2016.

Zhang, R., Lin, J., and Zhang, Q.: Satellite-based evaluation of nitrogen oxides emission inventory for Beijing at a high resolution, Bachelor, Peking University, unpublished, 19 pp., 2014.

Zhao, Y., Nielsen, C. P., Lei, Y., McElroy, M. B., and Hao, J.: Quantifying the uncertainties of a bottom-up emission inventory of anthropogenic atmospheric pollutants in China, Atmospheric Chemistry and Physics, 11, 2295-2308, ~~doi:~~10.5194/acp-11-2295-2011, 2011.

Zhao, Y., Qiu, L. P., Xu, R. Y., Xie, F. J., Zhang, Q., Yu, Y. Y., Nielsen, C. P., Qin, H. X., Wang, H. K., Wu, X. C., Li, W. Q., and Zhang, J.: Advantages of a city-scale emission inventory for urban air quality research and policy: the case of Nanjing, a typical industrial city in the Yangtze River Delta, China, Atmospheric Chemistry and Physics, 15, 12623-12644, 10.5194/acp-15-12623-2015, 2015.

Zheng, B., Huo, H., Zhang, Q., Yao, Z. L., Wang, X. T., Yang, X. F., Liu, H., and He, K. B.: High-resolution mapping of vehicle emissions in China in 2008, Atmospheric Chemistry and Physics, 14, 9787-9805, 10.5194/acp-14-9787-2014, 2014.

Zheng, B., Zhang, Q., Tong, D., Chen, C., Hong, C., Li, M., Geng, G., Lei, Y., Huo, H., and He, K.: Resolution dependence of uncertainties in gridded emission inventories: a case study in Hebei, China, Atmospheric Chemistry and Physics, 17, 921-933, ~~doi:~~10.5194/acp-17-921-2017, 2017.

5

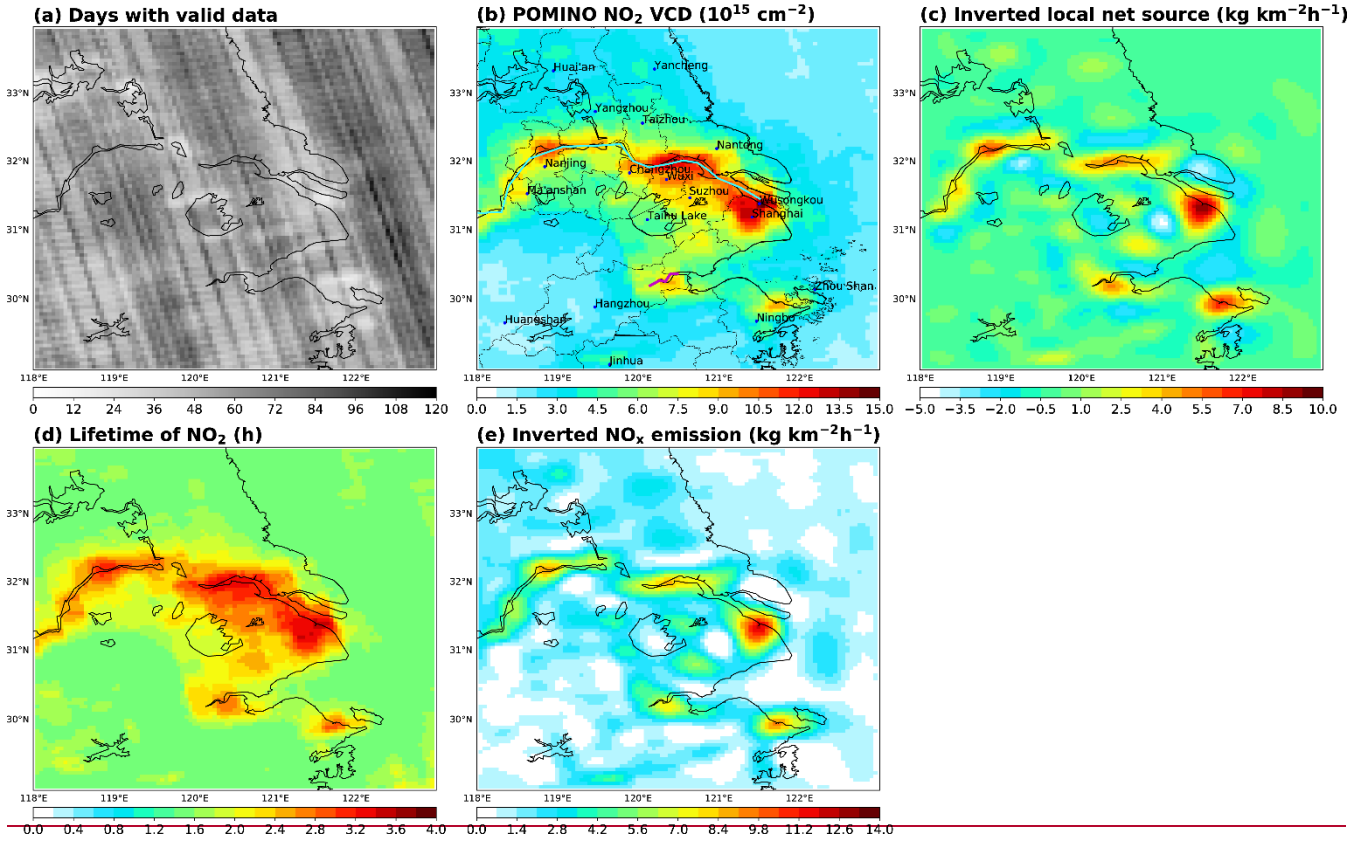
(a) Days with valid data
(b) POMINO NO2 VCD (10^15 cm^-2)
(c) Inverted local net source (kg km^-2h^-1)
(d) Lifetime of NO2 (h)
(e) Inverted NOx emission (kg km^-2h^-1)
Huai'an
Yancheng
Yangzhou
Taizhou
Nantong
Nanjing
Changzhou
Wuxi
Suzhou
Mt Tianshan
Taihu Lake
Wusongkou
Shanghai
Zhou Shan
Hangzhou
Huangshan
Ningbo
Jinhua
33°N
32°N
31°N
30°N
118°E
119°E
120°E
121°E
122°E
0 12 24 36 48 60 72 84 96 108 120
0.0 1.5 3.0 4.5 6.0 7.5 9.0 10.5 12.0 13.5 15.0
−5.0 −3.5 −2.0 −0.5 1.0 2.5 4.0 5.5 7.0 8.5 10.0
0.0 0.4 0.8 1.2 1.6 2.0 2.4 2.8 3.2 3.6 4.0
0.0 1.4 2.8 4.2 5.6 7.0 8.4 9.8 11.2 12.6 14.0

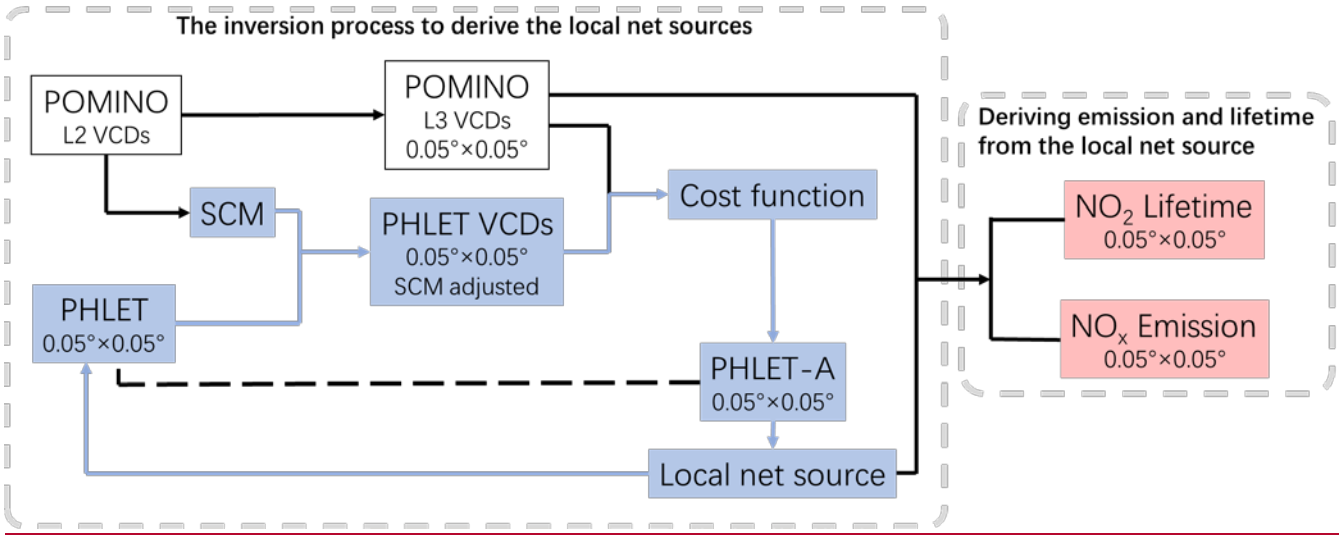
The inversion process to derive the local net sources
POMINO
L2 VCDs
POMINO
L3 VCDs
0.05°×0.05°
SCM
PHLET VCDs
0.05°×0.05°
SCM adjusted
Cost function
PHLET
0.05°×0.05°
PHLET-A
0.05°×0.05°
Local net source
Deriving emission and lifetime
from the local net source
NO2 Lifetime
0.05°×0.05°
NOx Emission
0.05°×0.05°

Figure ~~1.~~1. The flowchart of the framework of our methodology. The blue arrows show the iterative process.

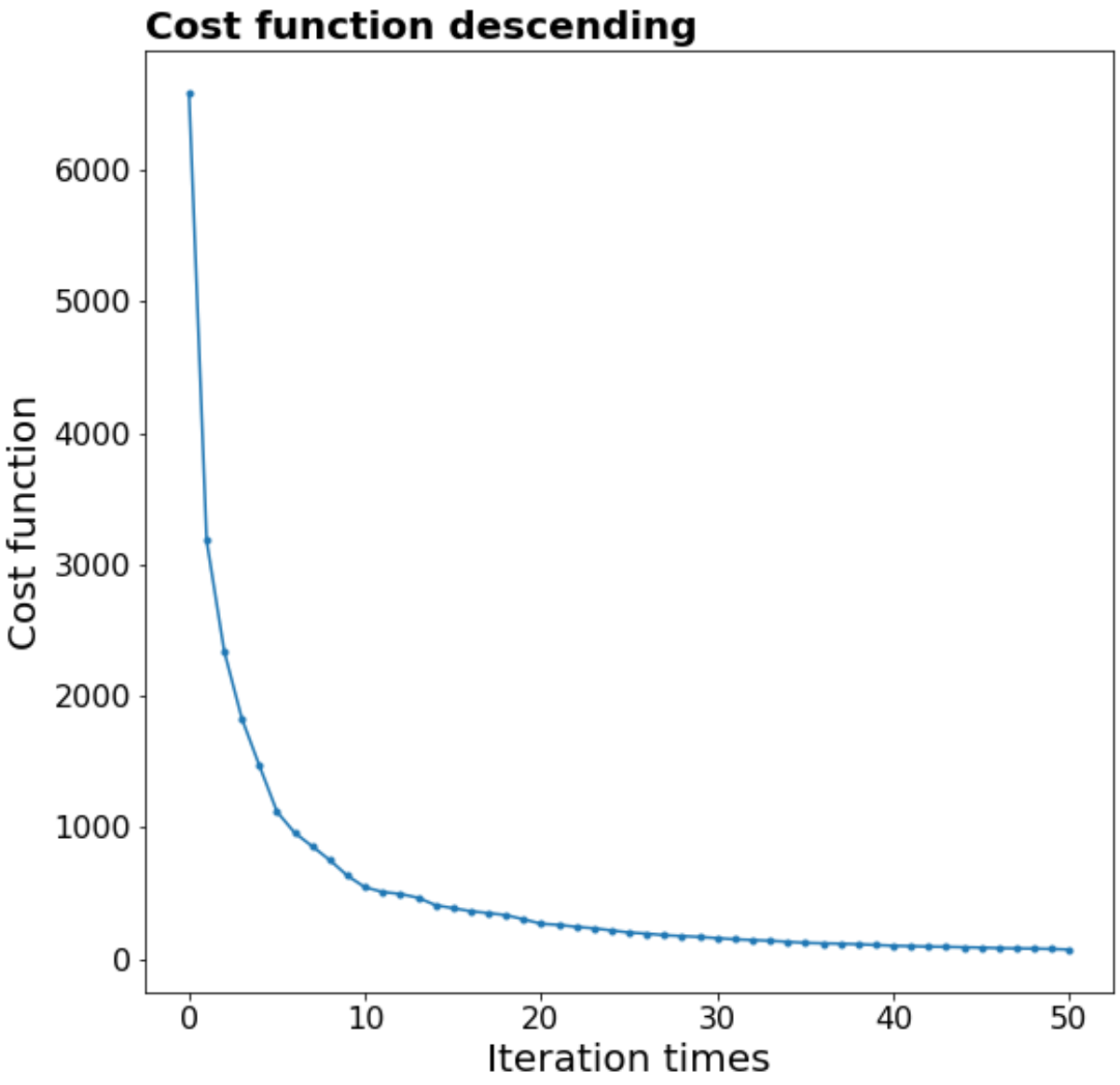

Figure 2. Cost function descending with iteration.

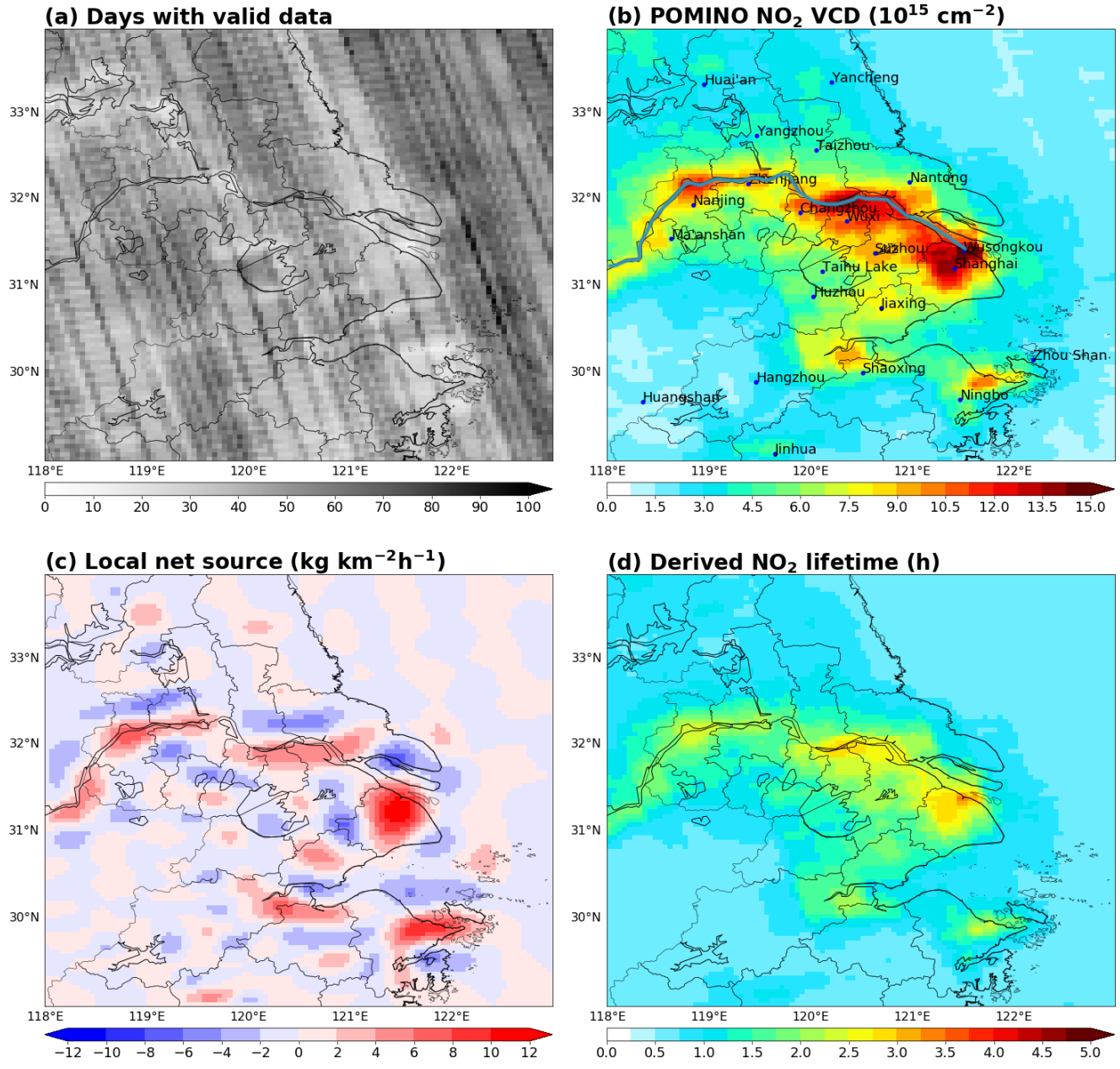

Figure 3. (a) Number of days with valid data in each grid cell over summer months of 2012–~~2016~~2015. (b) POMINO NO2 VCDs averaged over summer 2012–~~2016~~2015. Cities and locations mentioned in this paper are denoted. The Yangtze River is marked as a blue line~~, and the Qiantang River (passing Hangzhou) a purple line.~~. (c) ~~Inverted~~Derived local net source. (d) ~~Inverted~~Derived NO_x lifetime due to both chemical loss and deposition. ~~(e) Inverted NO_x emissions from anthropogenic and soil sources.~~

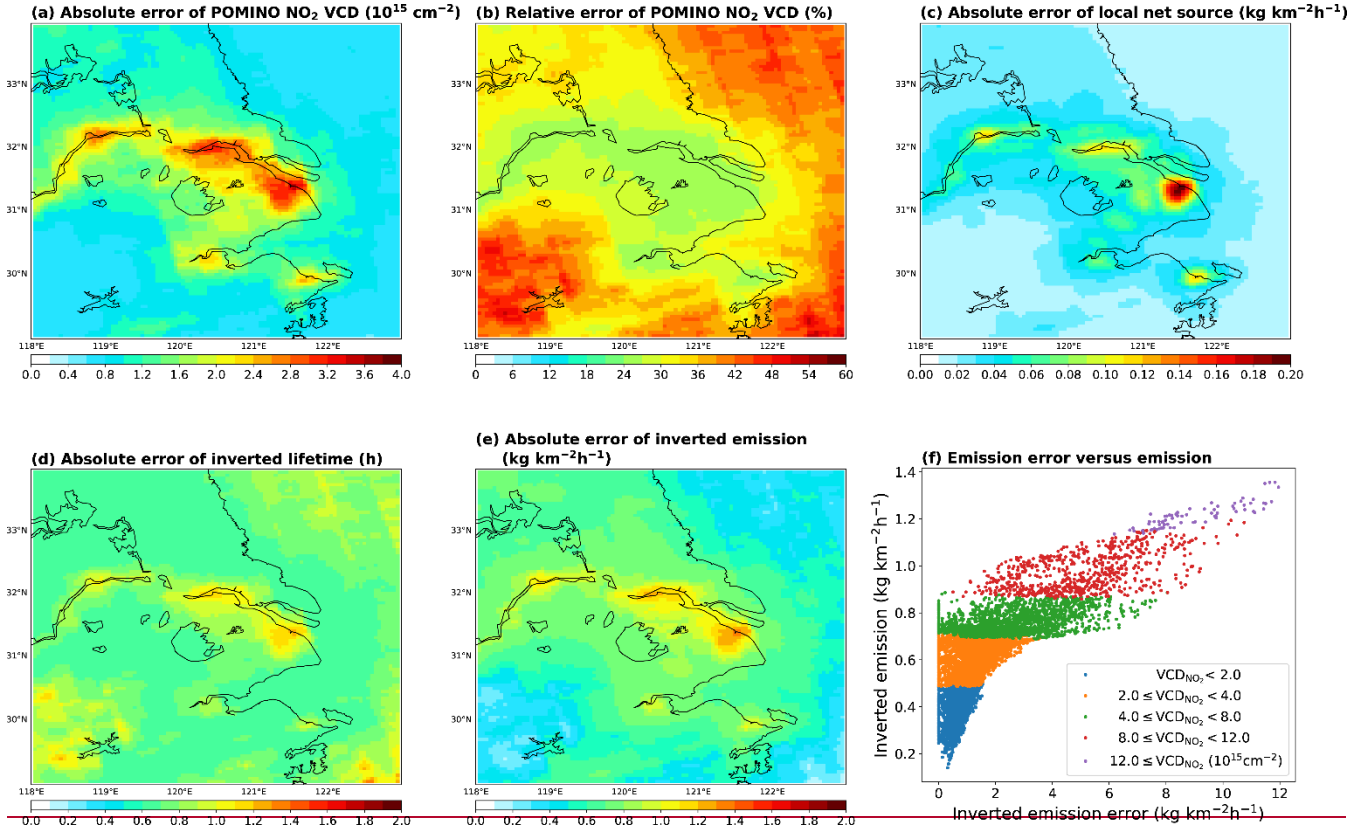
(a) Absolute error of POMINO NO2 VCD (10^15 cm^-2)
(b) Relative error of POMINO NO2 VCD (%)
(c) Absolute error of local net source (kg km^-2 h^-1)
(d) Absolute error of inverted lifetime (h)
(e) Absolute error of inverted emission (kg km^-2 h^-1)
(f) Emission error versus emission
Inverted emission (kg km^-2 h^-1)
Inverted emission error (kg km^-2 h^-1)
VCDNO2 < 2.0
2.0 ≤ VCDNO2 < 4.0
4.0 ≤ VCDNO2 < 8.0
8.0 ≤ VCDNO2 < 12.0
12.0 ≤ VCDNO2 (10^15 cm^-2)

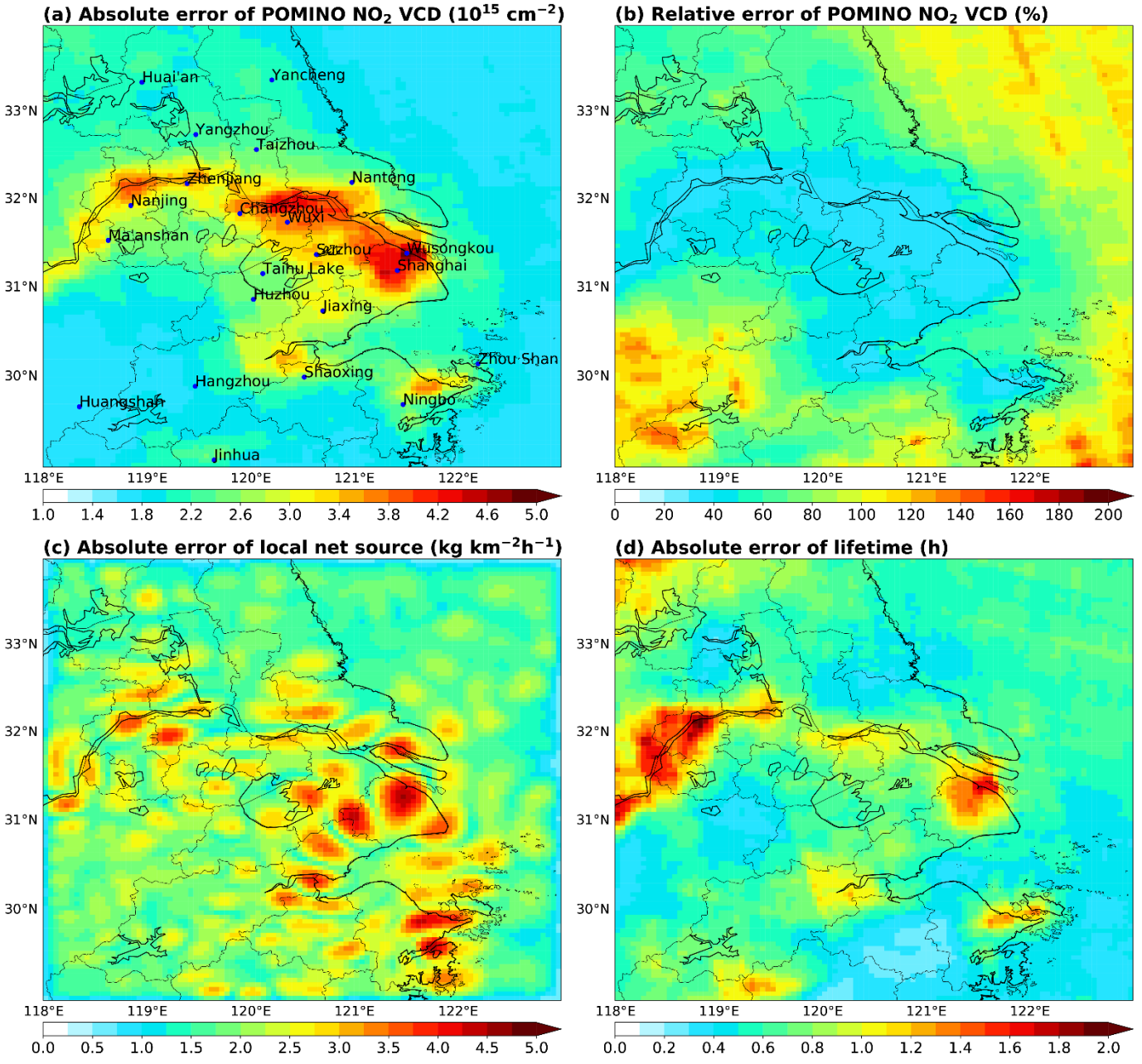

Figure ~~2~~4. (a) Absolute error (1_σ) of POMINO NO_2 VCD at each grid cell at ~~0.05°×0.05°~~ the 0.05°×0.05° resolution. (b) Relative error (1_σ) of POMINO NO_2 VCD. (c) Absolute error (1_σ) of the ~~inverted~~derived local net source. (d) Absolute error (1_σ) of the ~~inverted~~derived NO_x lifetime due to chemical loss and deposition. ~~(e)~~

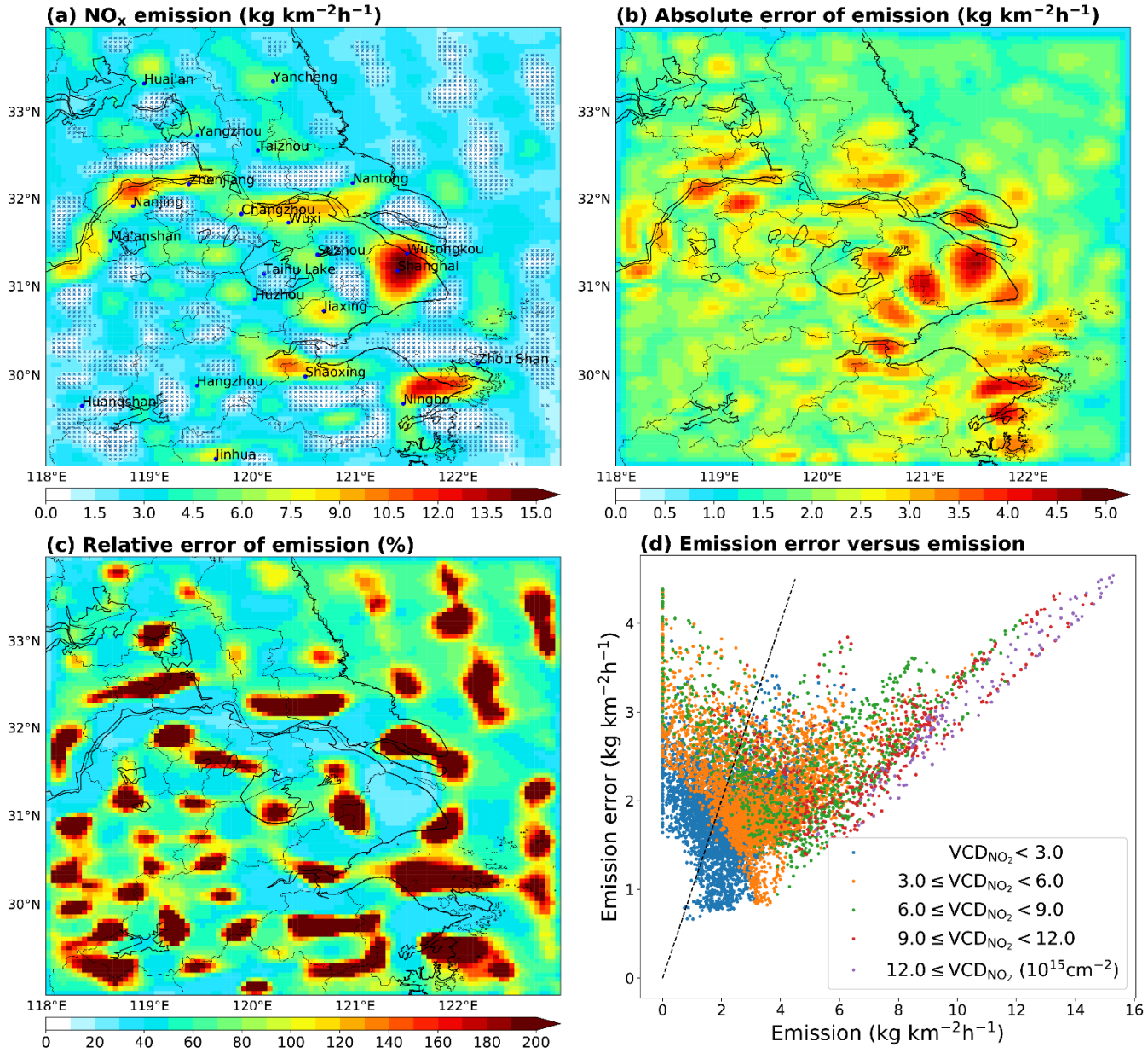

Figure 5. (a) Our NO_x emissions from anthropogenic, biomass burning and soil sources together. The blue corsses indicate where the relative errors exceed 100%. (b) Absolute ~~error~~errors (1 σ) of ~~inverted NO_x emission. (f)~~ our NO_x emissions. (c) Relative errors of our emissions. (d) Absolute ~~error~~errors (1 σ) of ~~inverted~~ NO_x ~~emission~~emissions as a function of ~~inverted~~ NO_x ~~emission~~emissions at ~~each~~individual grid

~~cell~~cells. Data points are coloured according to the magnitudes of POMINO NO_2 VCDs. The dashed line indicates an error of 100%.

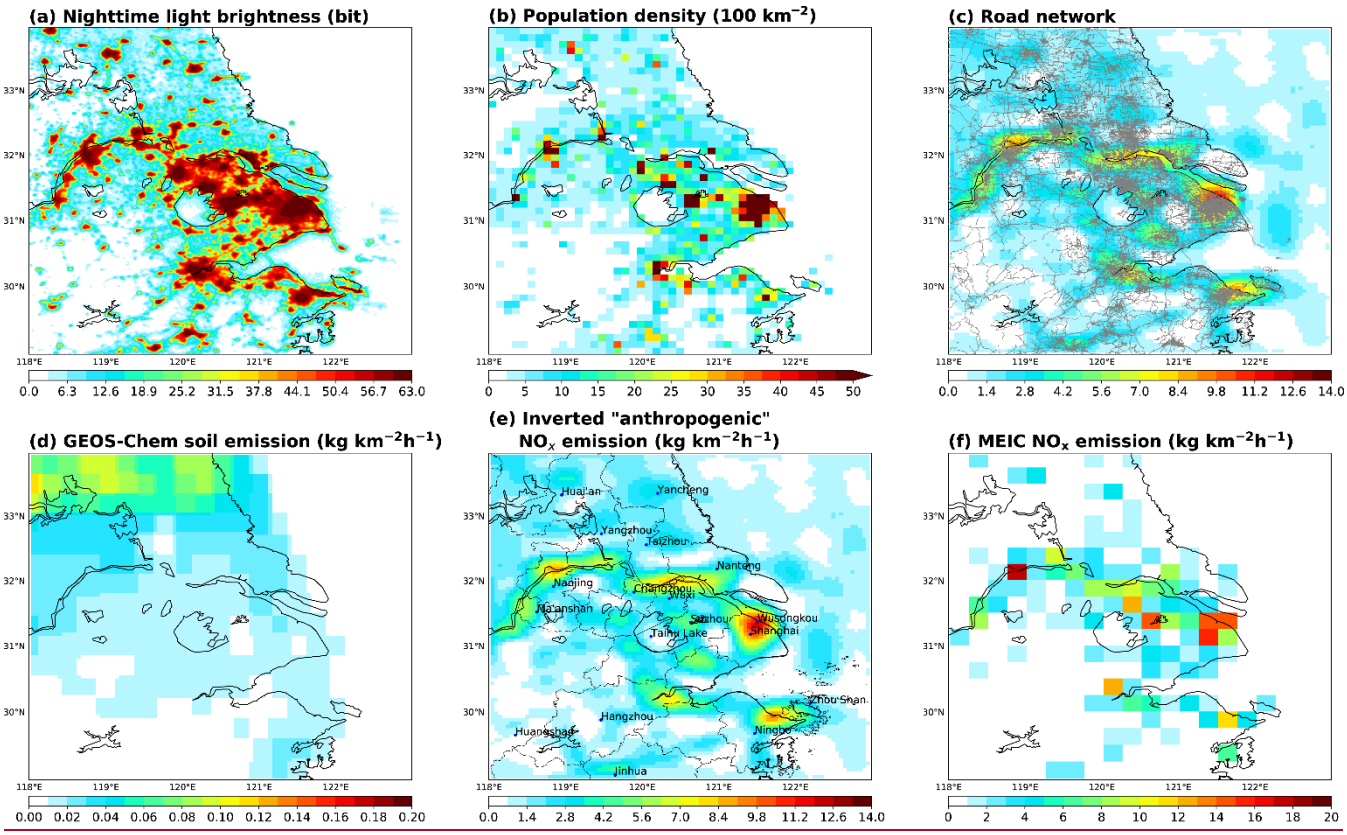

~~Figure 3. (a~~

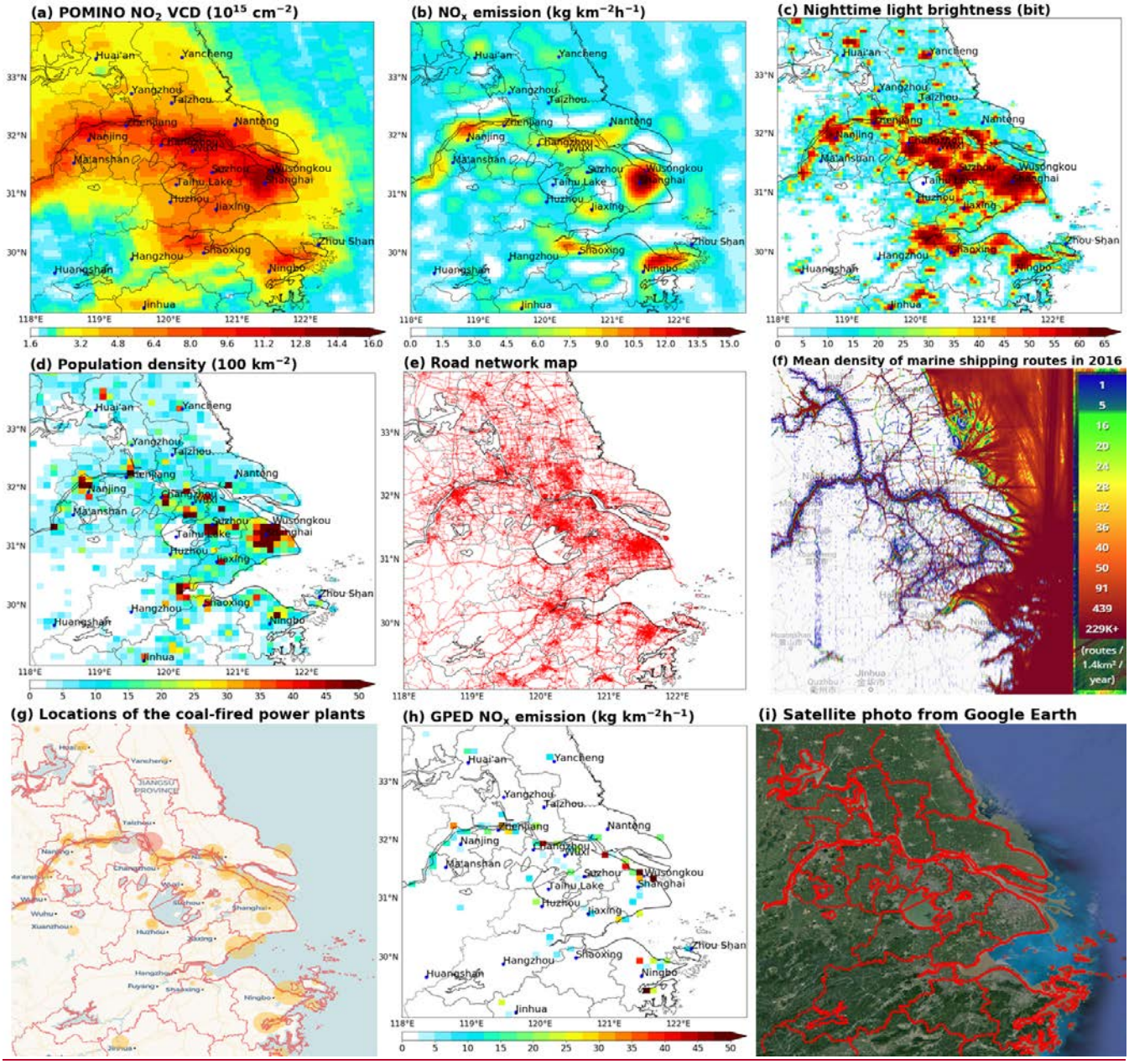

Figure 6. (a) POMINO NO_2 VCDs averaged over summer 2012–2015, which is same as Fig. 1a. but based on a different color scale. (b) Our NO_x emissions from anthropogenic, biomass-burning and soil sources together, same as Fig. 3a. (c) Nighttime light brightness ~~on a **0.5′ × 0.5′** grid~~ in 2012. (~~b~~d) Population density averaged over 2012~~–2016 on a **0.1° × 0.1°** grid.~~ (~~c~~) 2015. (e) Road network (~~grey lines) superimposed upon the inverted NO_x emissions. (~~dred lines). (f) Mean density of marine shipping routes

in 2016 (data source: www.marinetraffic.com). (g) Locations of coal-fired power plants in 2016 from Carbon Brief. (h) GPED v1.0 bottom-up NO_x emissions from coal-fired power plants. (i) A satellite photo from Google Earth taken in 2018.

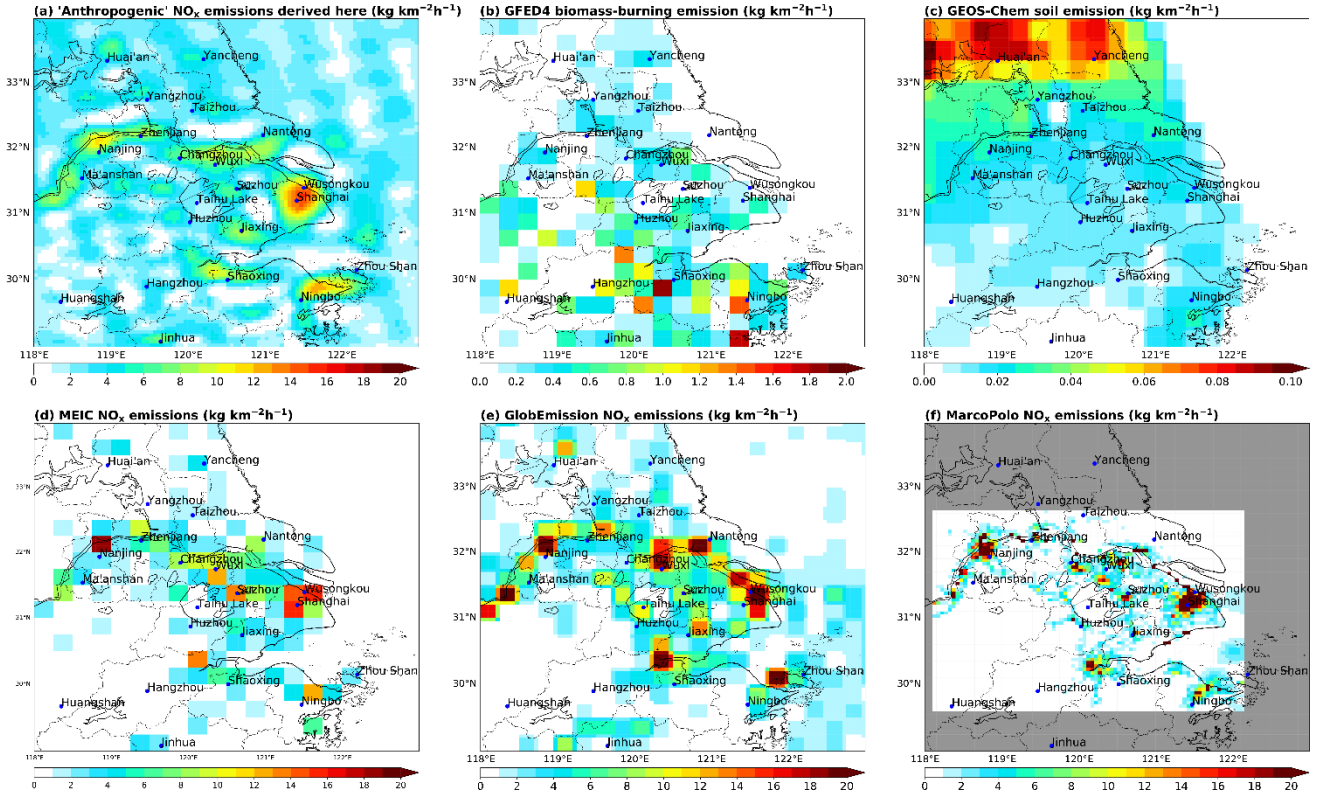

Figure 7. (a) Our "anthropogenic" NO_x emissions, by subtracting soil and biomass burning emissions from the derived emissions. (b) GFED4 biomass burning NO_x emissions. (c) Soil NO_x emissions calculated by a nested GEOS-Chem simulation ~~(0.25° × 0.3125°) and regraded~~. (d) MEIC NO_x emissions over summer 2012–2015. (e) DECSO v5.1qa top-down emissions in summer 2012–2015. (f) MarcoPolo bottom-up inventory in summer 2014; note that this inventory does not cover the grid cells shown in grey). All data are regridded to ~~the 0.05° × 0.05° grid. (e) Inverted "anthropogenic" NO_x emissions on a~~ 0.05° × 0.05° ~~grid. City names and boundaries are given. (f) MEIC NO_x emissions on a 0.25° × 0.25° grid~~.

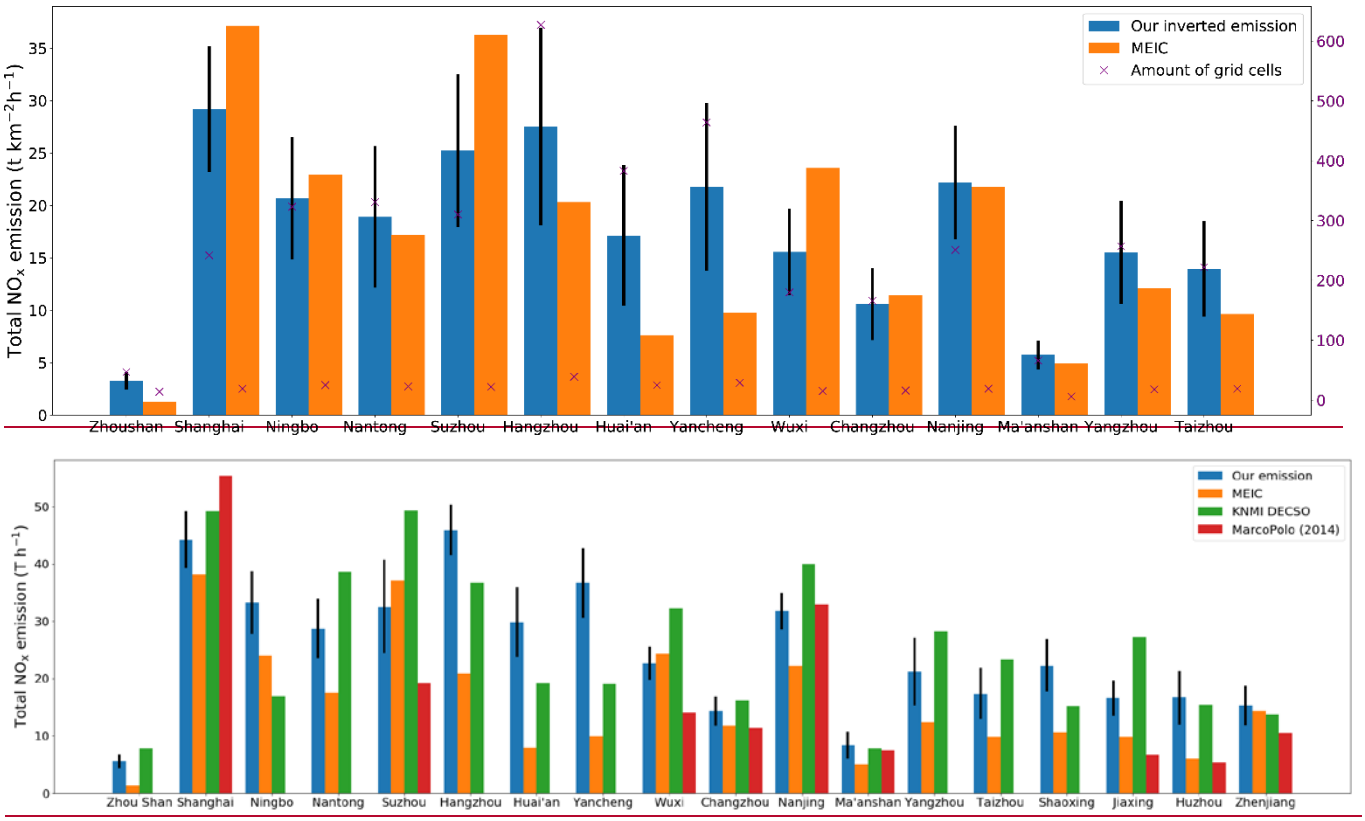

Figure ~~4~~8. Total anthropogenic NO_x emission in each city for summer 2012–~~2016 inverted here versus from the MEIC inventory.~~2015 derived here, in comparison with other emission datasets. Soil NO_x emissions calculated by the nested GEOS-Chem and biomass burning NO_x emissions from GFED4 have been subtracted from our ~~inverted~~ emission data and DECSO. Black vertical lines denote the uncertainty (1~~σ). Red points denote the numbers of grid cells covered by each city at different resolutions (0.05° × 0.05° in our inverted dataset and 0.25° × 0.25° in MEIC).~~ σ) of our emissions.

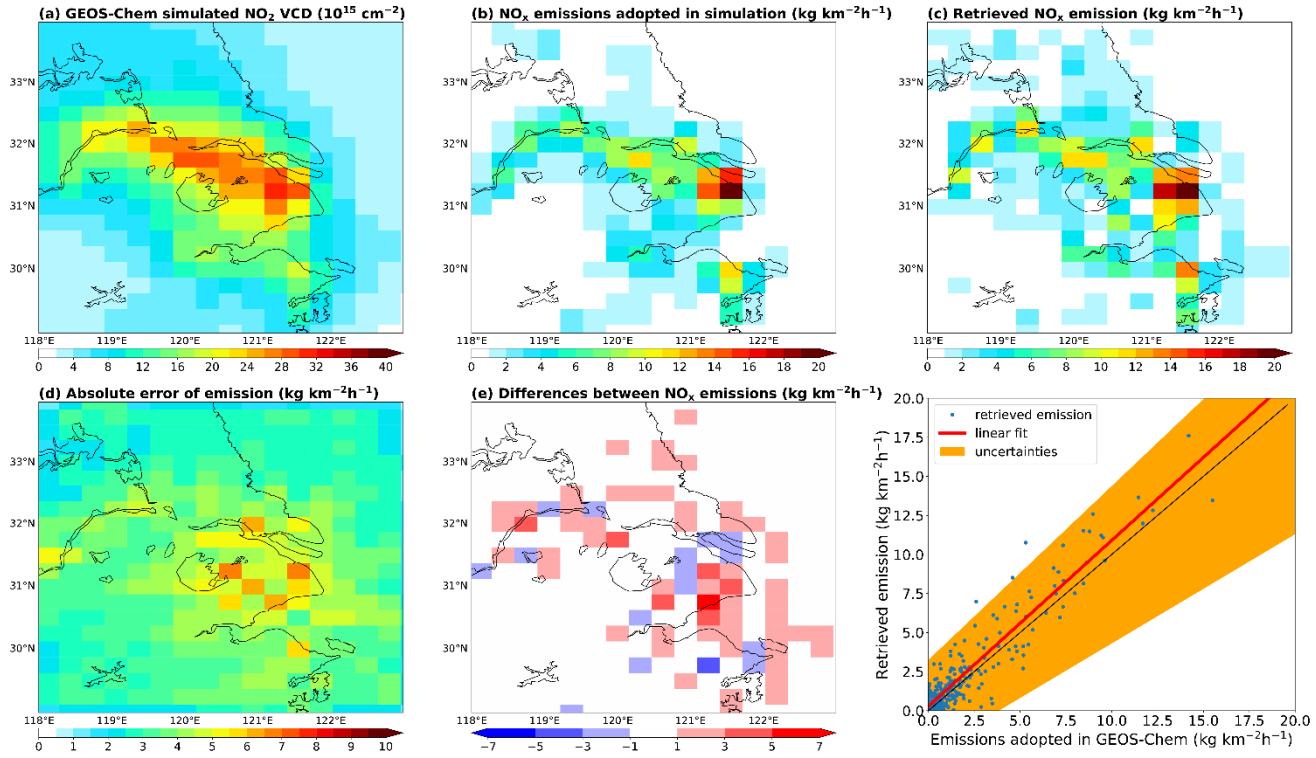

Figure 9. (a) GEOS-Chem simulated NO_2 VCDs at the 0.3125°×0.25° resolution for summer 2014. (b) Anthropogenic NO_x emissions used in GEOS-Chem. (c) Anthropogenic emissions derived based on GEOS-Chem simulated NO_2 VCDs and our inversion method. (d) Absolute errors (1 σ) of derived emission data. (e) Differences between the derived emissions and GEOS-Chem emissions (derived minus GEOS-Chem). (f) Scatter plot for the derived emissions (y-axis) and GEOS-Chem emissions (x-axis). The red line represents least square linear fitting. The shading represents the fitting by accounting for errors in the derived emission data, i.e., derived emissions + 1 σ for the upper bound, and derived emissions – 1 σ for the lower bound. The black dotted line denotes the 1:1 line.

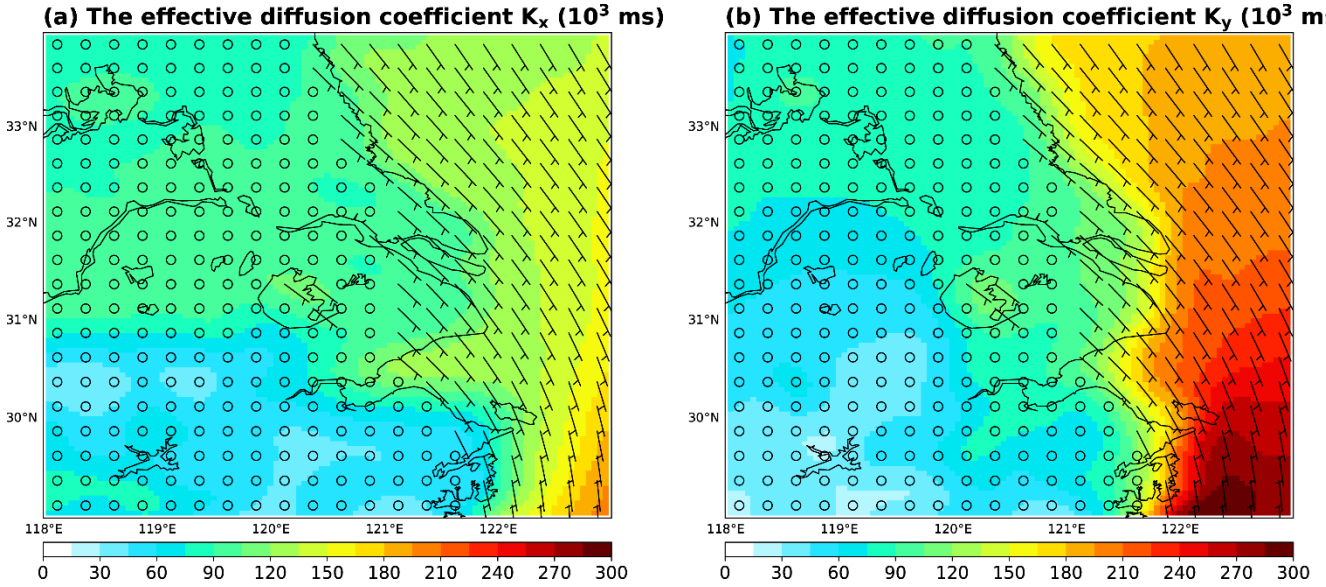

Figure ~~A1~~A. The effective diffusion coefficients for summer 2012–~~2016~~2015 on a 0.05° × 0.05° grid. Overlaid is the temporal mean wind vector, which is plotted for every 5 × 5 = 25 grid cells to enhance the readability.

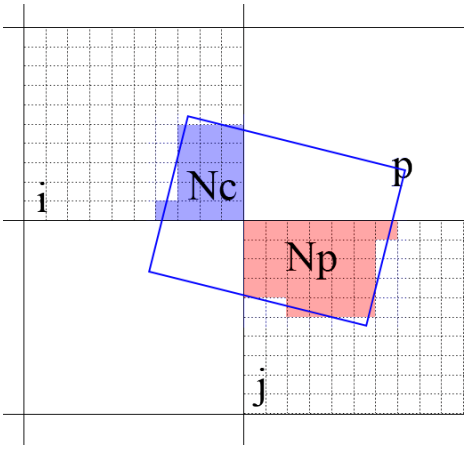

Figure ~~B1~~B. Illustration of how the original PHLET model grid cell i is projected to the satellite pixel p and then to the final grid cell j through the SCM approach. The size of the satellite pixel is scaled down to be comparable with the size of a model grid cell, for illustration ~~purpose~~purposes.

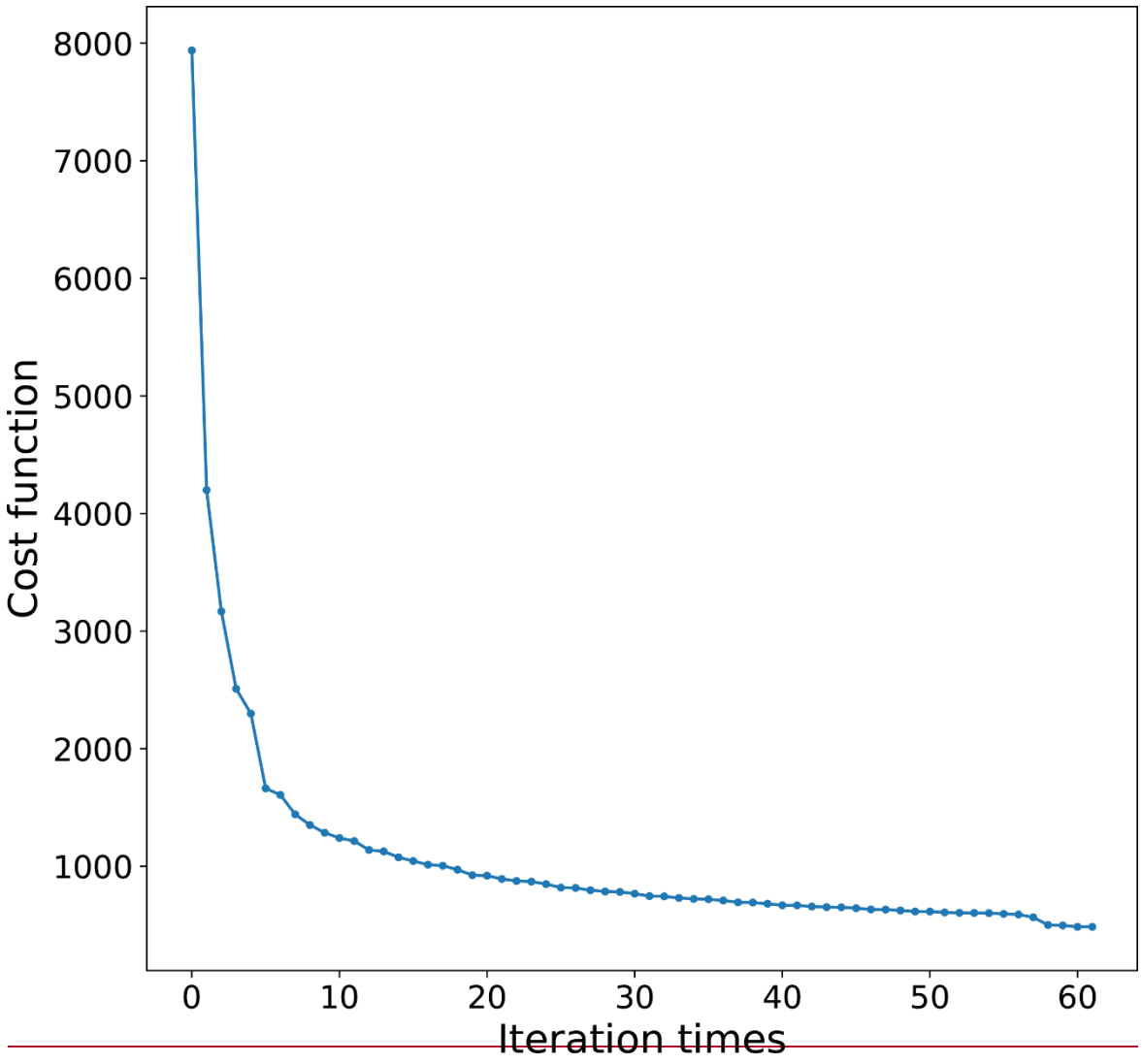
8000
7000
6000
5000
4000
3000
2000
1000
Cost function
0
10
20
30
40
50
60
Iteration times

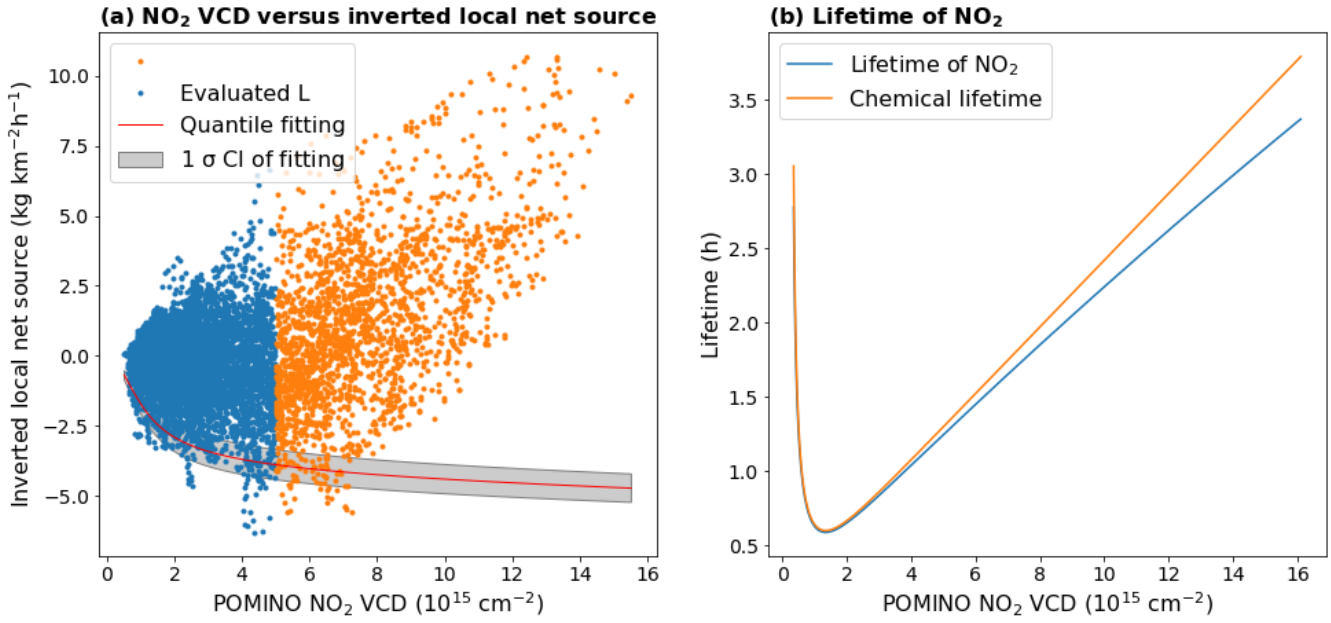

Figure ~~C1. Variation of the cost function *J* with iteration times.~~

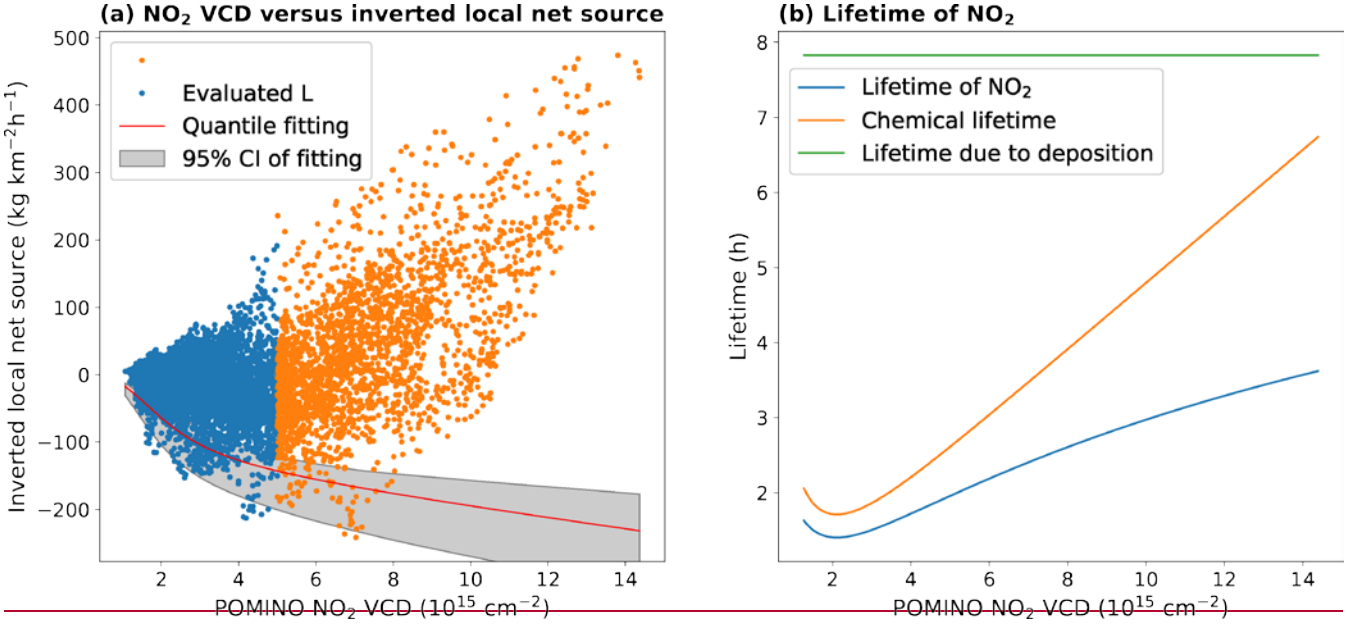

~~Figure D1~~C. (a) Scatter plot for POMINO NO_2 VCDs (x-axis) and ~~inverted~~derived local net sources (y-axis) across individual grid cells. Grid cells with NO_2 VCDs below (above) 5×10^{15} molecules cm^{-2} are coloured in blue (orange). The red line and shading denote the median and uncertainty (~~95%~~1 σ CI) of the quantile fitting, respectively, to estimate the nonlinear relationship between NO_2 VCD and lifetime,

based on data in the low-emission areas. (b) The derived relationship between NO_2 VCD and lifetime across the range of NO_2 VCDs in the YRD area.

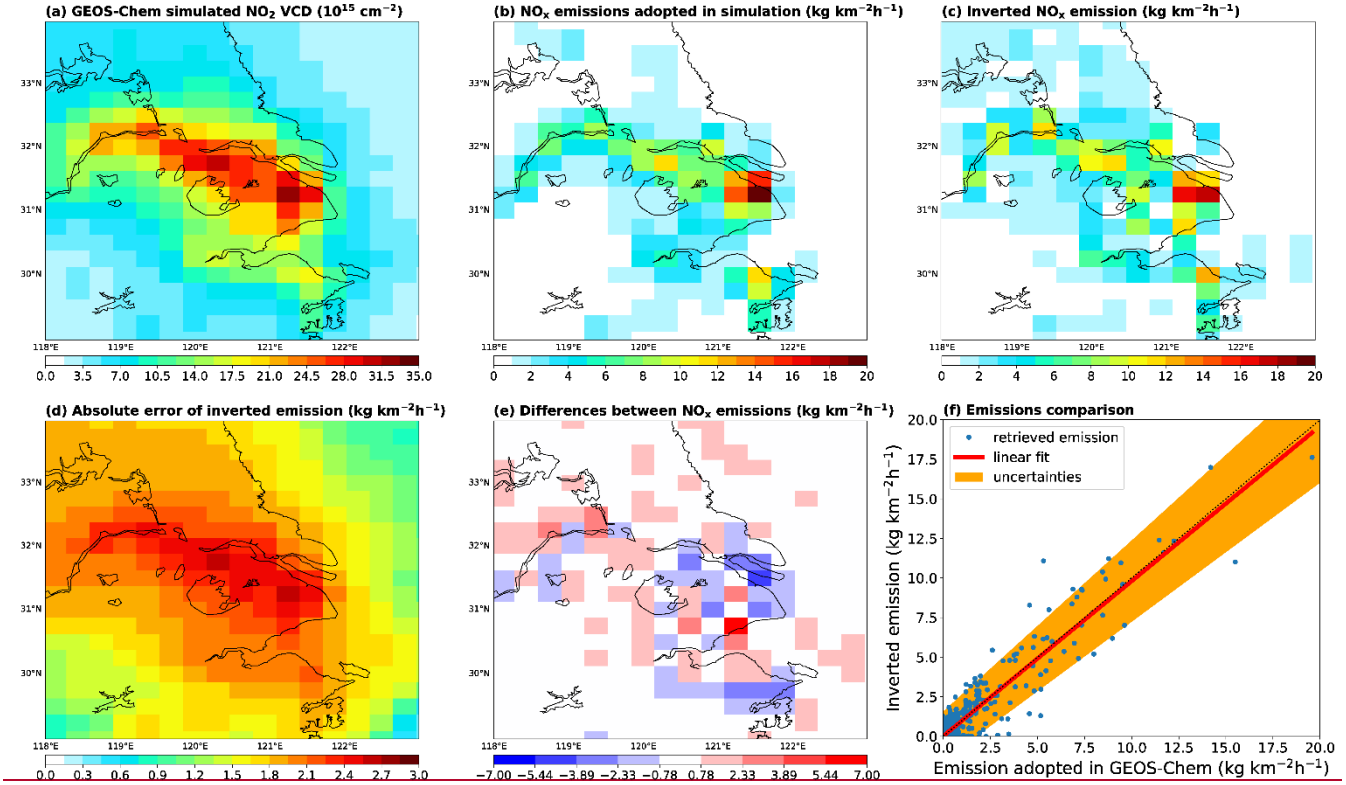

~~Figure E1. (a) GEOS-Chem simulated NO_2 VCDs at the **0.3125°** × **0.25°** resolution for summer 2014. (b) Anthropogenic NO_x emissions used in GEOS-Chem. (c) Inverted anthropogenic emissions based on GEOS-Chem simulated NO_2 VCDs. (d) Absolute errors (1σ) of inverted emission data. (e) Differences between the inverted emissions and GEOS-Chem emissions (inverted minus GEOS-Chem). (f) Scatter plot for the inverted emissions (y-axis) and GEOS-Chem emissions (x-axis). The red line represents least square linear fitting. The shading represents the fitting by accounting for errors in the inverted emission data, i.e., inverted emissions + 1σ for the upper bound, and inverted emissions – 1σ for the lower bound. The black dotted line denotes the 1:1 line.~~